



**BISTATIC 3D ELECTROMAGNETIC
SCATTERING FROM A RIGHT-ANGLE
DIHEDRAL AT ARBITRARY
ORIENTATION AND POSITION**

THESIS

Andreas Tempelis, Captain, USAF
AFIT/GE/ENG/11-39

**DEPARTMENT OF THE AIR FORCE
AIR UNIVERSITY**

AIR FORCE INSTITUTE OF TECHNOLOGY

Wright-Patterson Air Force Base, Ohio

APPROVED FOR PUBLIC RELEASE; DISTRIBUTION UNLIMITED.

The views expressed in this thesis are those of the author and do not reflect the official policy or position of the United States Air Force, Department of Defense, or the United States Government. This material is declared a work of the U.S. Government and is not subject to copyright protection in the United States.

AFIT/GE/ENG/11-39

BISTATIC 3D ELECTROMAGNETIC
SCATTERING FROM A RIGHT-ANGLE
DIHEDRAL AT ARBITRARY
ORIENTATION AND POSITION

THESIS

Presented to the Faculty
Department of Electrical and Computer Engineering
Graduate School of Engineering and Management
Air Force Institute of Technology
Air University
Air Education and Training Command
in Partial Fulfillment of the Requirements for the
Degree of Master of Science in Electrical Engineering

Andreas Tempelis, BSEE
Captain, USAF

March 2011

APPROVED FOR PUBLIC RELEASE; DISTRIBUTION UNLIMITED.

BISTATIC 3D ELECTROMAGNETIC
SCATTERING FROM A RIGHT-ANGLE
DIHEDRAL AT ARBITRARY
ORIENTATION AND POSITION

Andreas Tempelis, BSEE
Captain, USAF

Approved:

//signed//

10 March 2011

Dr. Julie A. Jackson (Chairman)

Date

//signed//

10 March 2011

Dr. Peter J. Collins (Member)

Date

//signed//

10 March 2011

Major Geoffrey A. Akers (Member)

Date

Abstract

A method is created to extend a bistatic 3D electromagnetic scattering solution for a dihedral at a given orientation and position to the case of arbitrary orientation and position. Results produced using this method are compared to shooting and bouncing rays (SBR) and method of moments (MoM) predictions, as well as measured data for applicable cases. The model in this thesis shows excellent agreement in magnitude and phase with SBR predictions. It also shows good agreement in magnitude with MoM predictions. Small phase differences between model and MoM data occur due to differences in the underlying scattering solution and the more exact MoM prediction. The model accurately predicts bistatic scattering from a dihedral at arbitrary orientation and position and is computationally more efficient than SBR and MoM methods.

Acknowledgements

I have many people to thank for helping me through my AFIT experience. First, I owe a big thank you to my fiancée. I couldn't have done this without her love and support. Getting to AFIT graduation will mean so much more knowing that we did it together. Also, I would like to thank my advisor, Dr. Julie Jackson. Her guidance, tough questions and high standards aided me immensely as I went through the thesis development process. Finally, I need to thank my fellow 11M LO's. You made the trials and tribulations of a graduate engineering education something close to enjoyable.

Andreas Tempelis

Table of Contents

	Page
Abstract	iv
Acknowledgements	v
List of Figures	viii
List of Tables	xii
I. Introduction	1
1.1 Problem Description	1
1.2 Research Goals and Methodology	2
1.3 Potential Applications	3
1.4 Organization of Thesis	4
II. Background	5
2.1 Chapter Overview	5
2.2 Previous Research	6
2.2.1 Dihedral Scattering	6
2.2.2 Previous 3D Models for Bistatic ATR	8
2.3 Important Concepts	11
2.3.1 Radar Cross Section	11
2.3.2 Scattering Regimes	13
2.3.3 Physical Optics	14
2.3.4 Other Methods	16
2.3.5 AFIT RCS Range	18
2.4 Chapter Summary	22
III. Scattering for Arbitrary Orientation and Position	23
3.1 Chapter Overview	23
3.2 Bistatic 3D PO Solution for Simple Plate	23
3.2.1 Plate Geometry	24
3.2.2 Plate Derivation	26
3.3 Bistatic 3D GO-PO Solution for Dihedral	30
3.3.1 Dihedral Geometry	30
3.3.2 Dihedral Derivation	31
3.4 Extension to Arbitrary Orientation and Position	35
3.4.1 Orientation	36
3.4.2 Position	40
3.4.3 Flow Chart	41
3.5 Chapter Summary	44

	Page
IV. Results	45
4.1 Chapter Overview	45
4.2 Data Presentation	46
4.3 Dihedral at Original Orientation and Position	47
4.4 Arbitrary Orientation and Position Model Validation	55
4.4.1 Dihedral with Roll, Pitch, Yaw Rotation and Translation from Origin	55
4.4.2 Comparison to Measured RCS Data	63
4.5 Additional Dihedral Validation	71
4.5.1 Dihedral Oriented for High Cross-Pol Intensity	73
4.5.2 Dihedral Oriented for Similar Co/Cross-Pol Intensity	80
4.6 Summary	86
V. Conclusion and Future Work	88
5.1 Conclusion	88
5.2 Future Work	88
A. Additional Data Comparisons	90
1.1 Simple Plate	90
1.1.1 Plate at Original Orientation and Position	90
1.1.2 Plate at Non-Original Orientation and Position	97
B. Co/Cross-pol Dihedral Scattering	103
2.1 Co/Cross-pol Equations	103
Bibliography	104
Vita	106

List of Figures

Figure		Page
1.1	Examples of dihedral targets at arbitrary orientation and position	2
2.1	Monostatic in-plane RCS pattern for dihedral	7
2.2	Geometry for 2D scattering center models and 3D dihedral parametric model	9
2.3	RCS scattering regions	14
2.4	Physical Optics approximation	15
2.5	Bistatic AFIT RCS range experiment setup	19
2.6	Dihedral targets for bistatic RCS measurements	20
2.7	Calibration error for bistatic RCS measurements	21
3.1	Simple plate geometry	25
3.2	Spherical coordinate geometry for bistatic radar configuration	27
3.3	Dihedral geometry	31
3.4	Global coordinate system to computation domain coordinate system	36
3.5	Roll, pitch, and yaw rotations	37
3.6	Electric field vector conversion	39
3.7	Flow chart for computing scattering for arbitrary orientation and position	43
4.1	Geometry and TX/RX angles for scene with dihedral at original orientation and position	48
4.2	Comparison of VV-pol scattering for the dihedral at original orientation and position	51
4.3	Comparison of HV-pol scattering for the dihedral at original orientation and position	52

Figure	Page
4.4	Comparison of VH-pol scattering for the dihedral at original orientation and position 53
4.5	Comparison of HH-pol scattering for the dihedral at original orientation and position 54
4.6	Geometry and TX/RX angles for scene with rotated and translated dihedral 56
4.7	Example coherent difference plots where incorrect phase correction is applied 57
4.8	Comparison of VV-pol scattering for the rotated and translated dihedral 59
4.9	Comparison of HV-pol scattering for the rotated and translated dihedral 60
4.10	Comparison of VH-pol scattering for the rotated and translated dihedral 61
4.11	Comparison of HH-pol scattering for the rotated and translated dihedral 62
4.12	Geometry and TX/RX angles for measurement scenario 1 64
4.13	Comparison of measured vs. predicted scattering for measurement scenario 1 66
4.14	Global range for Scenario 1 measured data 67
4.15	Geometry and TX/RX angles for measurement scenario 2 68
4.16	Comparison of measured vs. predicted scattering for measurement scenario 2 69
4.17	Global range for Scenario 2 measured data 70
4.18	Polarization effects for PEC plate and dihedral 71
4.19	Geometry and TX/RX angles for scene with dihedral oriented for high cross-pol scattering 74

Figure	Page
4.20	Comparison of VV-pol scattering for the dihedral oriented for high cross-pol RCS 76
4.21	Comparison of HV-pol scattering for the dihedral oriented for high cross-pol RCS 77
4.22	Comparison of VH-pol scattering for the dihedral oriented for high cross-pol RCS 78
4.23	Comparison of HH-pol scattering for the dihedral oriented for high cross-pol RCS 79
4.24	Geometry and TX/RX angles for scene with dihedral oriented for similar co/cross-pol scattering 80
4.25	Comparison of VV-pol scattering for the dihedral oriented for similar co/cross-pol RCS 82
4.26	Comparison of HV-pol scattering for the dihedral oriented for similar co/cross-pol RCS 83
4.27	Comparison of VH-pol scattering for the dihedral oriented for similar co/cross-pol RCS 84
4.28	Comparison of HH-pol scattering for the dihedral oriented for similar co/cross-pol RCS 85
A.1	Geometry and TX/RX angles for plate centered in XY plane 91
A.2	Comparison of VV-pol scattering for the plate centered in XY plane..... 93
A.3	Comparison of HV-pol scattering for the plate centered in XY plane..... 94
A.4	Comparison of VH-pol scattering for the plate centered in XY plane..... 95
A.5	Comparison of HH-pol scattering for the plate centered in XY plane..... 96
A.6	Geometry and TX/RX angles for rotated and translated plate 97

Figure	Page
A.7	Comparison of VV-pol scattering for the rotated and translated plate 99
A.8	Comparison of HV-pol scattering for the rotated and translated plate 100
A.9	Comparison of VH-pol scattering for the rotated and translated plate 101
A.10	Comparison of HH-pol scattering for the rotated and translated plate 102

List of Tables

Table		Page
4.1	Scattering summary for dihedral at original orientation and position	49
4.2	Scattering summary for dihedral with roll, pitch, yaw rotation and translation from origin	57
4.3	Measurement matrix for AFIT RCS range	63
4.4	Quantitative summary for measurement scenario 1	64
4.5	Quantitative summary for measurement scenario 2	67
4.6	Scattering summary for dihedral oriented for high cross-pol intensity	74
4.7	Scattering summary for dihedral oriented for similar co/cross-pol intensity	81
4.8	Computation time for cases examined	87
A.1	Scattering summary for plate at original orientation and position	91
A.2	Scattering summary for plate at non-original orientation and position	98

BISTATIC 3D ELECTROMAGNETIC
SCATTERING FROM A RIGHT-ANGLE
DIHEDRAL AT ARBITRARY
ORIENTATION AND POSITION

I. Introduction

1.1 Problem Description

Monostatic electromagnetic scattering from the basic dihedral shape has been comprehensively studied and is a well understood phenomenon. However, bistatic scattering has not been researched as extensively. Bistatic radar in general is again receiving interest in the radar and signal processing research community, due to its applicability to unmanned aerial vehicle (UAV) swarms and the inherent geometric information advantage over monostatic radar for Automatic Target Recognition (ATR) problems. The dihedral shape is commonly found in real world scenes of interest. Building-to-ground, car-to-ground, tree trunks-to-ground, etc. are examples of real-world dihedral features that, if correctly identified by long-range Synthetic Aperture Radar (SAR), would provide valuable information to the warfighter.

Electromagnetic scattering prediction codes based on Shooting and Bouncing Rays (SBR) or Method of Moments (MoM) can be used to obtain accurate bistatic scattering solutions for a right-angle dihedral placed at arbitrary position and orientation. However, these prediction codes are neither computationally efficient nor quickly modifiable to the parameters of the dihedral target. A parameterized, closed-form equation model based on high-frequency analysis techniques for a dihedral at arbitrary

orientation and position would greatly increase the computational efficiency (tenths of seconds versus hours) of finding the scene scattering behavior using a personal computer (PC). Further, the efficiency advantage is increased when considering time saved in modifying the surface mesh or facet information required for SBR or MoM predictions to account for arbitrary size, orientation, and position of the dihedral target.

1.2 Research Goals and Methodology

There are two main goals of this research effort. First, this research effort will create a method to extend the closed-form bistatic 3D dihedral scattering solution developed in [12] to account for arbitrary orientation and position. Second, it will validate the results produced by this method. An example of arbitrary dihedral orientations and positions as well as the orientation for the closed-form solution in [12] is shown in Figure 1.1. The result of successfully accomplishing these goals will be a validated, computationally efficient model to compute bistatic 3D scattering from a dihedral at arbitrary orientation and position.

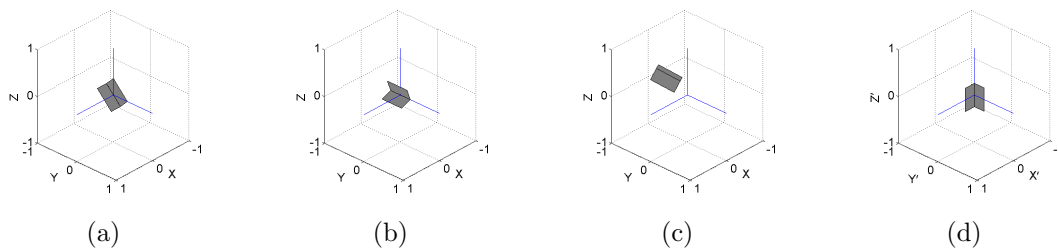


Figure 1.1. Examples of dihedral targets at arbitrary orientation and position. The model in this thesis is designed to calculate bistatic 3D scattering for a dihedral at arbitrary orientation and position (examples: a-c) by extending a closed-form bistatic 3D scattering solution for a dihedral orientated as shown in (d) developed in [12]. Prime notation in (d) indicates local target coordinates. Unprimed notation in (a)-(c) indicates global coordinates.

To this end, the bistatic 3D Physical Optics (PO) scattering solution is first found

for a simple plate. A plate is used because it is a subset shape comprising a dihedral and to simplify the scattering behavior for examining the effects of changes to orientation and position. A method is then developed to extend this solution to account for any combination of orientation, position and receive/transmit antenna aspect angles. This method is then applied to a Geometric Optics (GO) and PO hybrid closed-form scattering solution for a right-angle dihedral developed in [12]. Validation against SBR and MoM solutions is performed for both the simple plate and dihedral models. Further validation is accomplished by investigating model performance for dihedral orientations commonly used for calibration purposes as well as comparing to measured data. In this effort, orientation refers to the target's roll/pitch/yaw from a defined beginning orientation, while position refers to distance from the scene origin.

1.3 Potential Applications

The model developed in this thesis has two primary potential applications. First, it can be used in future bistatic ATR efforts where scattering waveform accuracy and timeliness is required. Because the model developed in this thesis produces waveforms which are a function of target size, orientation, and position (among other dependencies), there exists the potential to estimate these parameters in a real-world scene. The accurate scattering model developed in this thesis could be used to aide identification of a target dihedral's size, orientation, and position.

Second, the model developed in this thesis can potentially be used to provide timely calibration for airborne bistatic SAR systems. Dihedral calibration targets are commonly used for monostatic systems because of their high magnitude returns as well as polarization effects. Some current monostatic airborne SAR systems perform calibration based on the dihedral hip-pocket radar cross section (RCS) formula and scattering matrix [4]. The model developed in this thesis is more accurate in mag-

nitude and phase, is capable of accounting for any dihedral orientation and position, and is applicable to any bistatic transmitter/receiver (TX/RX) aspect angles within the interior corner of the dihedral.

1.4 Organization of Thesis

This thesis is organized into five chapters and two appendices. Chapter II provides theoretical background information related to the concepts investigated through this research effort as well as a review of similar efforts in the radar and signal processing communities. Chapter III describes the derivation of the PO solution for a simple plate with arbitrary orientation and position, and applies a similar approach to a dihedral target shape. Chapter IV includes results comparing data generated by the closed-form equations developed in this thesis to SBR and MoM based simulations as well as measured data. Chapter V contains the conclusion. Finally, data from the validation section not presented in Chapter IV is shown in Appendix A while additional dihedral scattering equations are provided in Appendix B.

II. Background

2.1 Chapter Overview

There are two purposes of this chapter. Current research into bistatic dihedral scattering is provided. Also, important concepts are explained which will aid the reader in understanding both the derivation and validation of the bistatic 3D dihedral scattering model for arbitrary orientation and position developed in this thesis.

The research section of this chapter will first summarize both monostatic and bistatic research efforts. It begins by explaining in-plane monostatic dihedral scattering and why dihedrals are useful calibration targets. It builds to summarizing development of a parametric bistatic 3D model for dihedral scattering based on 2D scattering center responses. This parametric bistatic 3D model is referred to as ‘parametric model’ throughout this thesis. The Geometric Optics-Physical Optics (GO-PO) based model in this thesis is shown in Chapter IV to be a more accurate descriptor of scattering for a dihedral at arbitrary orientation and position when compared to this parametric model.

In addition to research summaries, important concepts are provided to help the reader understand the derivation and validation in this thesis. First, basic RCS and scattering regime information is provided. The PO approximation is also explained. Third, scattering prediction methods based on SBR and MoM are summarized. Finally, experimental setup and calibration information for measurements taken in the AFIT RCS range are provided.

This chapter is organized into two sections. Section 2.2 contains information on previous research into electromagnetic scattering for a dihedral. Section 2.3 provides information on electromagnetic scattering concepts, prediction methods, and RCS measurement information.

2.2 Previous Research

This section summarizes previous research into dihedral scattering behavior and 3D scattering models.

2.2.1 Dihedral Scattering.

This section will describe previous monostatic and bistatic dihedral scattering research efforts. Monostatic scattering from a dihedral is a well-researched target class due to its usefulness as an RCS calibration object. There are many papers which consider monostatic, in-plane dihedral scattering. In [18], Michaeli uses Physical Theory of Diffraction (PTD) for analysis. In [8, 9], Griesser and Balanis use two methods, PO combined with PTD and PO combined with Uniform Theory of Diffraction (UTD) [8, 9] to analyze monostatic, in-plane dihedral scattering. These models are accurate but are not extended to out-of-plane RX/TX angles, where RX refers to the receiver and TX refers to the transmitter.

The in-plane monostatic RCS pattern of a right-angle dihedral corner reflector for aspect angle shown in Figure 2.1a is given in Figure 2.1b. Figure 2.1b shows the characteristic broad center pattern which is dominated by the double-bounce mechanism shown in Figure 2.1a. The two peaks at $\pm 45^\circ$ are the peak specular returns from the single bounce off the two simple plates. The slight sinusoidal behavior in the central part of the pattern (-30° to 30°) is produced by the sidelobes of this single bounce return. The width and intensity of the RCS pattern is one of the main reasons why dihedrals are well suited as calibration devices [20, 7].

In [16], Knott gives the hip-pocket RCS formula for a dihedral as $\sigma = \frac{8\pi(ab)^2}{\lambda^2}$ where a and b are the length and width of one of the two plates of the dihedral. This formula requires equally sized plates which compose the dihedral. In [4], Blejer calibrates an airborne monostatic SAR system by comparing measured peak response

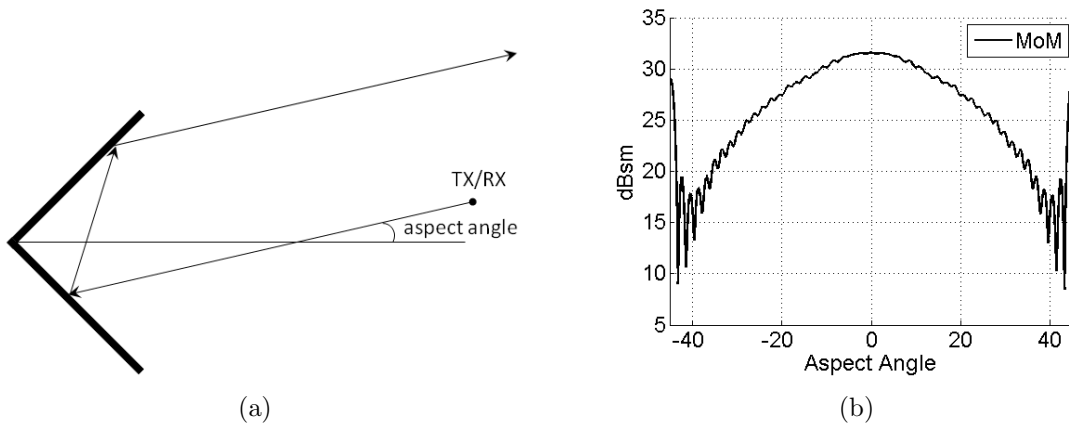


Figure 2.1. Monostatic in-plane RCS pattern for dihedral. (a) For monostatic in-plane scattering, rays entering a right-angle dihedral are reflected back in the direction from which they came. (b) Monostatic RCS pattern of a right-angle dihedral with square faces 0.5m along a side measured at 10 GHz.

from a dihedral to this hip-pocket RCS formula.

In [8], Griesser and Balanis investigate monostatic dihedral returns for various corner angles using both the GO-PO technique developed by Knott [14] and a more rigorous solution using numerical integration to find the PO near-field integral for the interior reflection. They find that the GO-PO technique compares well with experimental measurements for right angle (90°) and wider ($> 90^\circ$) dihedral corner reflectors but offers the least accuracy for acute (77°) dihedral corner reflectors. The PO near-field integral technique increases accuracy for acute dihedrals but offers little accuracy increase for right angle and obtuse dihedrals at the cost of significant computational complexity. Their findings provide motivation to use the GO-PO technique to study the right-angle dihedral in this thesis.

In [24], Wang and Jeng apply arbitrary orientation to a PO dihedral RCS solution, but their solution is only for the monostatic case and does not give the complex scattering solution needed for SAR.

In [13], Jackson predicts bistatic 3D scattering response using 2D scattering cen-

ter models extended to 3D. These models are examined in the next section. In [12], Jackson derives a more accurate model for bistatic dihedral scattering for fixed position and orientation using a hybrid GO-PO approach. This approach is extended in Section 3.3 to account for arbitrary orientation and position of the dihedral.

2.2.2 Previous 3D Models for Bistatic ATR.

This section will summarize the relevant parts of [13], which develops bistatic 3D parametric models based on 2D scattering center responses. These 3D parametric models are intended to model the dominant forward scatter while remaining less computationally complex than exact scattering solutions. In Chapter IV, data created using these models is referred to as ‘PM’ and is used as an additional comparison waveform when examining measured dihedral scattering data collected in the AFIT RCS range.

The three-dimensional shape responses in [13] are developed as products of the two-dimensional response. For example, when considering a three-dimensional right-angle dihedral with its seam aligned with the y-axis, one notices it is a combination of a two-dimensional right-angle in elevation and a flat plate scatterer in azimuth. Using Geometric Theory of Diffraction (GTD) to model the far-field, the high-frequency bistatic shape response of the 2D right angle of sufficient size ($H \gg \lambda$) is given as [13]:

$$M_{\text{right}}(k, \psi_t, \psi_r; H, \tilde{\psi}) = \left(\frac{jk}{\sqrt{\pi}} \right)^{1/2} 2H \text{sinc}[kH(\cos(\psi_t - \tilde{\psi}) - \cos(\psi_r - \tilde{\psi}))] \\ \times \begin{cases} \sin \frac{\psi_t + \psi_r - 2\tilde{\psi}}{2}, & \psi_t, \psi_r \in [\tilde{\psi}, \tilde{\psi} + \frac{\pi}{4}] \\ \cos \frac{\psi_t + \psi_r - 2\tilde{\psi}}{2}, & \psi_t, \psi_r \in [\tilde{\psi} + \frac{\pi}{4}, \tilde{\psi} + \frac{\pi}{2}] \end{cases} \quad (2.1)$$

where $k = 2\pi f/c$ is the wavenumber, H is the length of the sides, $\tilde{\psi}$ is the orientation

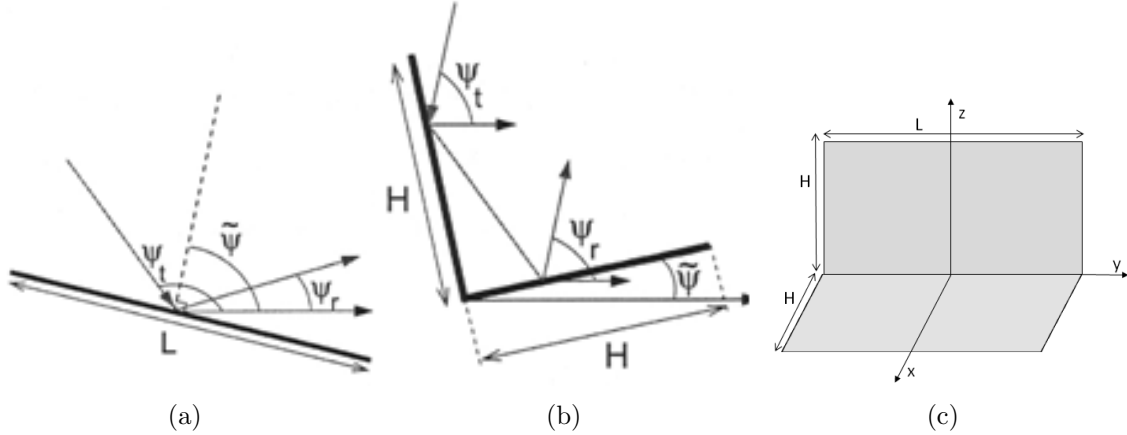


Figure 2.2. Geometry for 2D scattering center models and 3D dihedral parametric model, (a) 2D flat plate, (b) 2D right-angle, (c) 3D dihedral. The 2D scattering center response for flat plate (a) and right-angle (b) targets serve as the basis for the 3D dihedral model developed in [13]. Source for (a),(b) is [11].

angle of the 2D dihedral measured counterclockwise from the positive horizontal axis, and ψ_t and ψ_r are the transmit and receive angles respectively. See Figure 2.2b.

Similarly, the two-dimensional flat plate has bistatic scattering response given by

$$M_{\text{flat}}(k, \psi_t, \psi_r; L, \tilde{\psi}) = \left(\frac{jk}{\sqrt{\pi}} \right)^{1/2} L \operatorname{sinc} \left[k \frac{L}{2} (\sin(\psi_t - \tilde{\psi}) + \sin(\psi_r - \tilde{\psi})) \right],$$

$$\psi_t, \psi_r \in \left[\tilde{\psi} - \frac{\pi}{2}, \tilde{\psi} + \frac{\pi}{2} \right] \quad (2.2)$$

where L is length and $\tilde{\psi}$ is orientation angle.

Next, the three-dimensional dihedral response can be formed by multiplying the two-dimensional right angle and flat plate responses. This is because the three-dimensional dihedral functions as a right angle in elevation and a flat scatterer in

azimuth.

$$\begin{aligned}
M_{\text{dih}} &= M_{\text{flat}}(k, \phi_t, \phi_r; L, \tilde{\phi} = 0) M_{\text{right}}(k, \vartheta_t, \vartheta_r; H, \tilde{\psi} = 0) \\
&= \frac{jk}{\sqrt{\pi}} 2LH \operatorname{sinc}\left[k \frac{L}{2} (\sin \phi_t \cos \vartheta_t + \sin \phi_r \cos \vartheta_r)\right] \operatorname{sinc}[kH(\cos \vartheta_t - \cos \vartheta_r)] \\
&\quad \times \begin{cases} \sin \frac{\vartheta_t + \vartheta_r}{2}, & \vartheta_t, \vartheta_r \in [0, \frac{\pi}{4}] \\ \cos \frac{\vartheta_t + \vartheta_r}{2}, & \vartheta_t, \vartheta_r \in [\frac{\pi}{4}, \frac{\pi}{2}] \end{cases}, \phi_t, \phi_r \in \left[-\frac{\pi}{2}, \frac{\pi}{2}\right] \quad (2.3)
\end{aligned}$$

where L is the length of the three-dimensional dihedral, H is equal to the width of each of the plates which make up the dihedral, and ϑ is the elevation angle of the transmitter or receiver. Note that this thesis uses θ to indicate the traditional spherical angle from the z -axis down to the vector while ϑ is used here to indicate elevation angle from the xy -plane up to the vector ($\vartheta = \pi/2 - \theta$).

Finally, the shape response M_{dih} is multiplied with the polarization response and an exponential propagation factor to represent the complete returned signal S . This returned signal is dependent only on wave number k , transmitter and receiver angles, and the location, orientation, and size of the target.

It follows that other three-dimensional shapes can be modeled by the same method using different combinations of flat, right-angle, and circular planar responses. In [13], the author defines the three-dimensional response for rectangular plate, dihedral, square trihedral, cylinder, top-hat, and sphere shapes. Because these models are based on the geometric shape of the target, the model parameters are related to the geometry of the target, providing a basis for the feature estimation problem central to ATR.

The term feature estimation encompasses accurate identification of the feature type (e.g. dihedral vs. sphere) as well as accurate estimation of the true feature size, orientation, and position [13]. An accurate polarimetric scattering model for

canonical shapes such as the dihedral is central to correctly estimating the physical parameters in a scene. In [13], the parametric models described in this section are compared to SBR scattering predictions and are deemed an acceptable descriptor of the bistatic forward scattering from an object. However, these parametric models are not electromagnetically exact, show differences when compared to SBR predictions, and do not closely match MoM predictions. It will be shown in Chapter IV that the model developed in this thesis produces nearly identical magnitude and phase information when compared to SBR predictions, is very similar to MoM predictions, and is more accurate than the parametric model described in this section for a dihedral at arbitrary orientation and position.

2.3 Important Concepts

The information in this section will help the reader understand the tools and techniques used to derive the model central to this thesis as well as understand the various prediction methods used to validate it. First, basic RCS and scattering regime information is given. This is followed by an explanation of the theory behind the PO approximation. Third, scattering prediction methods based on SBR and MoM are summarized. Finally, experimental setup and calibration information for measurements taken in the AFIT RCS range are provided.

2.3.1 Radar Cross Section.

Radar cross section (RCS) is a measure of power scattered in a given direction when a target is illuminated by an incident electromagnetic wave [16]. The formal definition of RCS is the power density scattered in the direction of the receiver divided by the power per unit area (power density) incident at the target [17]. In terms of

the incident and scattered electric field intensities, the RCS is defined as [16]

$$\sigma \triangleq \lim_{R \rightarrow \infty} 4\pi R^2 \frac{|\vec{E}_s|^2}{|\vec{E}_i|^2} \quad (2.4)$$

where R is range to the target, and \vec{E}_s and \vec{E}_i are the scattered and incident electric fields respectively. Because the wave's power per unit area at the receiving antenna decreases as $1/(4\pi R^2)$ with distance, the factor $4\pi R^2$ in Equation (2.4) ensures the RCS is a function of aspect angles but not distance [19]. The limit is used in Equation (2.4) to ensure that the receiver is in the far field, i.e. that the received wave is planar.

Because the RCS is a real number formed by squaring the amplitude of a complex number representing the scattered electric field, all phase information is lost. It is useful, especially for ATR and SAR applications, to keep the phase information. Therefore, the root of σ is implicitly used when dealing with complex scattering values, using the equation [16]:

$$\sqrt{\sigma} \triangleq \lim_{R \rightarrow \infty} 2\sqrt{\pi} R \frac{\vec{E}_s}{\vec{E}_i}. \quad (2.5)$$

When providing RCS magnitude, units are most commonly given in decibels relative to area (dBsm):

$$\sigma[\text{dBsm}] = 10 \log \sigma = 20 \log |\sqrt{\sigma}| \quad (2.6)$$

The scattered electric field, and therefore RCS, is a function of many factors; target size, orientation, shape and material, radar frequency, and transmit and receive aspect angles and polarization. In general, bistatic RCS for a target is given as $\sigma_{\text{pol}_t, \text{pol}_r}(\theta_t, \phi_t, \theta_r, \phi_r)$ where pol_t and pol_r indicate the transmit and receive polarizations respectively and θ, ϕ are the spherical angles representing the transmit

(subscript t) and receive (subscript r) locations in the far field.

2.3.2 Scattering Regimes.

There are three regimes which characterize scattering behavior. They are dependent on the ratio between wavelength, λ and target length, L . The impacts of different scattering behavior in each region are important to consider when creating an RCS test plan and analyzing the results. The regimes shown in Figure 2.3 are the Rayleigh region, the Resonant region, and the Optics region, which correspond roughly to $L \ll \lambda$, $\lambda \leq L \leq 10\lambda$, and $L \gg \lambda$, respectively.

In the Rayleigh region, there is little phase variation of the incident wave over the surface of the scattering body and only the target size is important, not its individual features. In the Resonant region, there is significant phase variation over the length of the scattering body and surface and creeping waves significantly influence the scattered field. In this region, exact solutions of Maxwell's equations are required. Finally, in the Optical region, wavelength is much smaller than scattering body size, and the scattering response from a target can be considered as the summation of the returns from independent scattering centers. In this region, detailed geometry becomes important in the scattering process, and high-frequency techniques such as the PO approximation and Geometric Theory of Diffraction are accurate [16, 3, 20]. For this reason, the size of targets used for validation in Chapter IV have minimum dimensions of 0.25 meters for X-band ($\lambda \approx 0.03$ meters). Further, the Geometric Optics (GO) - PO hybrid method to predict dihedral scattering derived in [12] and used in this thesis is not validated below the Optical region.

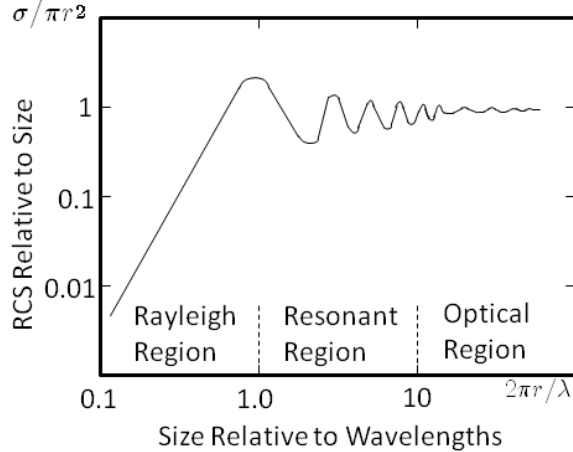


Figure 2.3. RCS scattering regions. The three regions are typically shown with respect to the RCS of a sphere, where r is the radius. In the Rayleigh region, RCS increases with frequency to the fourth power and specific target characteristics other than total area are trivial. In the Resonant region, second order effects such as travelling and creeping waves are the dominant scattering mechanism. In the Optical region, specular scattering is the dominant mechanism.

2.3.3 Physical Optics.

The PO approximation is a high frequency electromagnetics technique in which GO fields are utilized to compute currents for the radiation integrals that are encountered in scattering applications [6]. It is an approximate, not electromagnetically exact solution involving two assumptions to obtain the surface current [3]. First, the radii of curvature of the surface is large compared to wavelength (i.e. the surface is locally planar). Second, currents exist only in the area that is directly illuminated by the incident wave and currents on the illuminated surface have the same characteristics as of those on an infinite plane tangent to the surface at the point of incidence (i.e. 2nd order effects such as traveling and creeping waves are not accounted for).

For a perfect electrical conductor (PEC) target, the surface current is $\vec{J}_s = \hat{n} \times \vec{H}$ where $H = \vec{H}_s + \vec{H}_i$ and \hat{n} is the surface normal, \times indicates the cross-product operator, \vec{H} is the total magnetic field, \vec{H}_s is the scattered magnetic field, and \vec{H}_i is the incident magnetic field. Therefore, in an equivalent problem without the target,

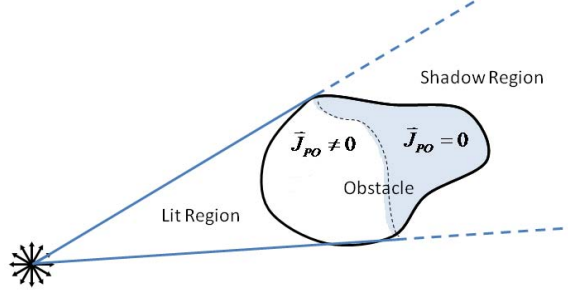


Figure 2.4. Physical Optics approximation. The PO approximation will exhibit non-physical behavior in the shadow region.

the scattered field will be maintained by the approximate equivalent electric surface current density:

$$\vec{J}_s^{\text{eq}} \approx \vec{J}_{\text{PO}} = \begin{cases} 2\hat{n} \times \vec{H}^i & \text{lit region} \\ 0 & \text{shadow region.} \end{cases} \quad (2.7)$$

Once the PO surface current density is found, one may use far-zone radiation integrals to compute the scattered field to find the RCS.

Although the PO approximation models well the currents on the illuminated portion of the target, there is a sudden jump between nonzero and zero current at the shadow boundary, see Figure 2.4. This non-physical behavior indicates that the PO approximation produces inaccurate scattering behavior near and within the shadow region. However, it is highly accurate near the mainlobe response [1, 16, 3, 6]. For this reason, the PO-based model central to this thesis shows promise for bistatic ATR and airborne SAR calibration, which both emphasize forward scatter mainlobe accuracy over sidelobe accuracy.

Furthermore, the closed-form GO-PO solution developed in this thesis is many orders of magnitude less computationally intensive than other prediction methods based on Shooting and Bouncing Ray (SBR) methods or Method of Moments (MoM) solutions. This advantage is increased for larger target size relative to wavelength. Additionally, a closed form solution does not require a surface mesh or other type of

geometry file to be created prior to simulation. These points will be expanded upon in the next section.

2.3.4 Other Methods.

This section will present information on other electromagnetic scattering prediction tools which are used in this thesis effort to create simulated reference data. The SBR and MoM electromagnetic scattering methods are presented followed by a discussion of geometry meshes.

2.3.4.1 Shooting and Bouncing Rays.

The SBR technique combines GO and PO theory to numerically predict the scattered EM field. A collection of parallel rays in the transmit direction are traced as they reflect off the target. The field for each ray is computed using GO, and PO is used to find the induced surface current and field contribution from the last reflection point on the target [2]. The field contributions from each ray are summed in the far-field to find the total scattered field. SBR is more computationally efficient than MoM and other electromagnetic analysis techniques based on solutions to the differential or integral forms of Maxwell's equations; the main computational burden of SBR lies in the ray tracing. The SBR technique is used in this thesis as a first-order accuracy benchmark for comparison which does not account for traveling wave or other second order effects. The closed-form GO-PO model used in this thesis is very similar to the SBR method in that both techniques are PO based and use GO to calculate the incident propagation vector for the double bounce scattering between the two dihedral plates.

2.3.4.2 Method of Moments.

The MoM is a numerical technique to solve for target surface current \vec{J}_s and the associated scattered (reradiated) fields. The surface current is induced on the target by the transmitted electromagnetic field. Using electromagnetic boundary conditions and assuming linear, homogeneous and isotropic media, one may define electric and magnetic field integral equations to relate the incident field to a surface integral containing \vec{J}_s [1]. The MoM technique discretizes the integral equations over a target surface mesh and solves the resulting system of equations to obtain the surface current. Then the associated scattered field is computed. In general, MoM is highly accurate when the mesh size is adequately small ($\approx \frac{\lambda}{10}$) and is excellent at predicting scattering from planar perfect electrical conductor (PEC) targets such as a metallic dihedral [3]. However, MoM techniques have significant computational time and storage requirements. MoM computations can be accelerated by applying fast multipole method (FMM) and multilevel fast multipole algorithm (MLFMA), which are techniques for exploiting symmetry or periodicity in structures [5, 21, 22]. However, these techniques still require computation time on the order of hours rather than minutes (SBR) or seconds (closed-form GO-PO model) using a PC for the cases examined in this thesis.

2.3.4.3 Geometry Mesh.

The above electromagnetic prediction techniques both depend on some type of target surface geometry information. This geometry information is typically contained in a target surface mesh. The mesh file requires computational resources to create and subdivides the target surface into triangular facets where each triangle side is adjacent to another triangle side so that each node is shared between multiple triangles. The mesh can also be subdivided into other geometric representations such

as quadrilaterals or bicycle splines. Creating this target surface geometry information and modifying it for arbitrary orientation and position is an additional step of computational resources that is not required when using the closed form solution developed in this thesis. Further, increasing the target dimensions directly increases the number of mesh nodes, which increases the number of unknowns in a MoM solution and directly increases the computation requirements. This relation between target dimensions and computation time is also avoided by using the closed-form solution in this thesis.

2.3.5 AFIT RCS Range.

For various dihedral orientations used for validation in Chapter IV, AFIT RCS range data is used as an additional comparison waveform for the method developed in this thesis. This section describes the experimental setup for bistatic measurements in the AFIT RCS range and also provides calibration information.

2.3.5.1 Experimental Setup.

The experimental setup in the AFIT bistatic indoor range facility is shown in Figure 2.5. The dihedral target is located on a pedestal in the center of the range. The transmit antenna position is fixed, and the receive antenna moves in a circle of radius = 8' around the target. The target pedestal is rotated to achieve a transmitter azimuth aspect angle of ϕ_t . The receive azimuth ϕ_r varies as the bistatic arm moves.

The first orientation case measured experimentally is the dihedral at 90° roll and 45° pitch, while the second measurement is of the dihedral at 90° roll and 20° pitch, relative to the original dihedral position defined in Figure 3.3. Roll, pitch, and yaw are defined as right-hand rotation about the x , y , and z axes, respectively. Figure 2.6 shows the dihedral mounted on the pylon at these orientations. These

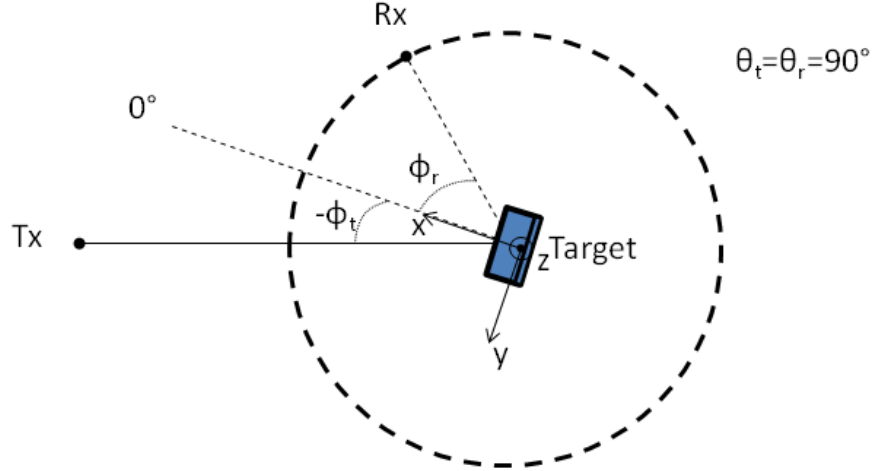


Figure 2.5. Bistatic AFIT RCS range experiment setup.

experiment orientations were chosen for two reasons. First, the orientations were physically realizable using styrofoam mounts. Styrofoam is used because its relative permeability and relative permittivity are nearly 1 at X-band frequencies, making it essentially invisible to the radar. This is required to allow the target dihedral to appear as if it is floating above the pylon. Second, the mainlobe forward scatter was positioned very close to waterline ($\theta = 90^\circ$). This is because the bistatic arm is fixed in θ , and is unable to be positioned at off-waterline elevations, therefore dihedral orientations which 'launch' the peak bistatic response far from waterline will produce weak sidelobe returns at the receiver and are not useful RCS data comparisons for this thesis effort.

2.3.5.2 Calibration.

In order to collect an accurate bistatic RCS measurement, the data collected from the AFIT RCS range needs to be calibrated. Four measurements are required to collect accurate target data. Once the data has been collected, it can be calibrated



Figure 2.6. Dihedral targets for bistatic RCS measurements. (a) 90° roll and 45° pitch, with bistatic receiver in background. (b) 90° roll and 20° pitch positioned on pedestal. Orientations are relative to the original dihedral position defined in Figure 3.3.

by [16]:

$$\sigma_{calibrated} = \frac{\sigma_{tar} - \sigma_{tar_B}}{\sigma_{cal} - \sigma_{cal_B}} \times \sigma_{thy} \quad (2.8)$$

where $\sigma_{calibrated}$ is calibrated RCS data, σ_{tar} is the target measurement, σ_{tar_B} is the target background measurement, σ_{cal} is the calibration target measurement, σ_{cal_B} is the calibration target background measurement, and σ_{thy} is the theoretical calibration target RCS. The theoretical response is found using MoM software. A cylinder is used as the calibration target due to relatively high RCS response and insensitivity to misalignment errors.

In order to verify calibration quality, two calibration cylinders (375mm and 450mm) were measured at $\phi_r = 45^\circ$. The calibration comparison and difference plot over 7-15 GHz for the 450mm cylinder are shown in Figure 2.7. The specific dihedral measurements shown in Chapter IV were taken at 10 GHz, for this frequency the magnitude difference between the calibrated 450mm cylinder measurement and the theoretical response is found to be -0.018 dB (HH-pol) and 0.318 dB (VV-pol). This error is very small and indicates data calibrated using the 450mm cylinder measurement is well calibrated.

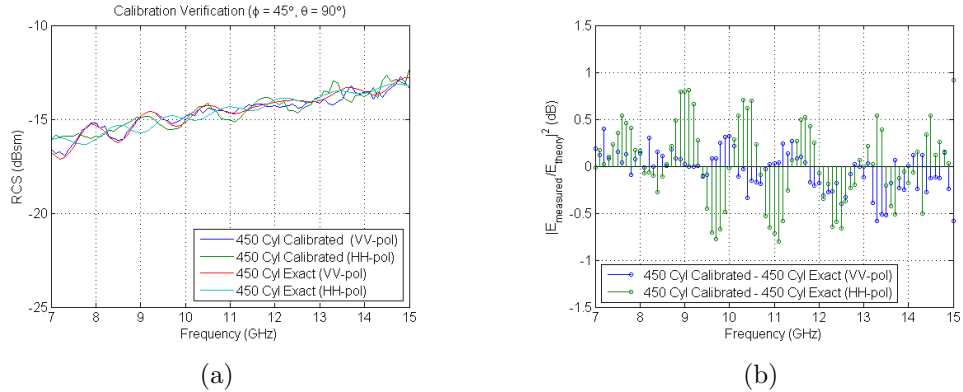


Figure 2.7. Calibration error for bistatic RCS measurements. (a) Calibration comparison and (b) calibration difference plots for the 450mm calibration cylinder bistatic measurement.

2.3.5.3 Measured Data Uncertainty.

Uncertainty in measured data is an important consideration because data collected in the AFIT RCS range is used in Section 4.4.2 as validation data. Three possible sources of measurement uncertainty in the dihedral measurements are inexact target orientation, surface inconsistencies, and transmitter antenna offset. Although great care was taken while cutting the styrofoam mounts, the blocks most likely do not tilt the dihedral at exactly 45° and 20° . Also, the surface of the target dihedral is likely marred by physical inconsistencies which could produce slightly different scattering behavior than from a dihedral composed of ideally planar surfaces. Finally, the horizontal and vertical transmitters in the AFIT RCS range are separated by approximately one foot. This can be accounted for in the monostatic case by manually shifting each polarization by a slightly different angular value. However, this physical antenna offset in the bistatic case results in slightly different transmitter aspect angles for each polarization because the target is centered to a point between the two antennas, not to each antenna individually. In practice, this causes the VV-polarization data to be slightly lower ($\approx 0.5\text{dB}$) in magnitude than expected because

the transmit antenna is positioned at a slightly larger angle than intended. Likewise, the HH-polarization measurements are generally higher than predictions because the antenna is positioned at a slightly smaller transmit angle than desired. These sources of measurement uncertainty are probable causes of the differences in scattering behavior observed in Section 4.4.2 between the measured data and computer based prediction methods.

2.4 Chapter Summary

This chapter has examined past research into dihedral scattering and 3D bistatic scattering models. It also summarized key concepts including RCS, scattering regimes, PO approximation, SBR and MoM prediction methods, and the AFIT RCS range. At this point, the reader is prepared to understand both the model derivation in Chapter III and validation in Chapter IV.

III. Scattering for Arbitrary Orientation and Position

3.1 Chapter Overview

The purpose of this chapter is to explain the bistatic 3D PO scattering solutions for both the simple plate and dihedral target types as well as a method to extend these solutions to arbitrary target orientation and position. The simple plate PO derivation is for a fixed orientation centered in the XY plane and follows the methods described in Section 2.3.3. The dihedral GO-PO solution was first computed in [12] and is for a fixed orientation with the dihedral seam aligned with the z axis. That derivation is summarized below. Then a method is presented to extend these solutions to the case of a flat plate or dihedral target at arbitrary orientation and position. The resulting closed form solutions produce an accurate representation of the scattering for these targets in significantly less time than predictive software based on SBR or MoM solutions. The simple plate is analyzed prior to the dihedral in order to gain familiarity with PO analysis for the bistatic 3D case as well as to reduce the complexity of the scattering behavior when observing the effects of arbitrary target orientation.

This chapter is organized as follows. Section 3.2 derives the bistatic 3D PO scattering solution for a simple plate in the XY plane. Section 3.3 summarizes the bistatic 3D scattering solution for the dihedral calculated in [12]. Finally, Section 3.4 presents a method to extend these solutions to arbitrary target orientation and position.

3.2 Bistatic 3D PO Solution for Simple Plate

This section will present the bistatic 3D PO scattering solution derivation for a simple plate centered in the XY plane. A plate is examined prior to the dihedral for the author and reader to become familiar with bistatic 3D PO analysis, to simplify the

scattering behavior when observing the effects of arbitrary target orientation, as well as to have greater confidence for validation of the arbitrary orientation and position transforms. The term ‘simple’ is used to indicate that the plate has no depth along the z axis.

This section contains two parts. Section 3.2.1 presents the simple plate geometry as well as coordinate system transform formulas. Section 3.2.2 contains the full derivation for the simple plate centered in the XY plane.

3.2.1 Plate Geometry.

The geometry for a simple plate centered in the XY plane with an arbitrary incident field is shown in Figure 3.1. This is referred to as the ‘original’ orientation when discussing orientation changes for the flat plate in Appendix 1.1. The coordinate axes, spherical angles, and incident field components are given a prime notation to indicate they are aligned with the target’s coordinate system and to differentiate these values from global axes, spherical angles and incident field components which will be defined in Section 3.4. In this case, \hat{z}' is the unit vector normal to the plate’s surface, \vec{k}' is the incident direction vector, and the vertical and horizontal components of the incident electric field are represented by \vec{E}'_{θ} and \vec{E}'_{ϕ} respectively. Finally, W indicates size of the plate in meters along the y' -axis and d indicates size of the plate along the x' -axis.

Prior to explaining the detailed derivation in the following section, it is useful to define the conversion formulas necessary to switch between Cartesian and spherical components. This begins with defining Cartesian and spherical vector representation in Equation (3.1). Converting between these forms is accomplished using Equation (3.2) to convert from Cartesian vector components to spherical vector components while Equation (3.3) is used to convert spherical vector components to Cartesian

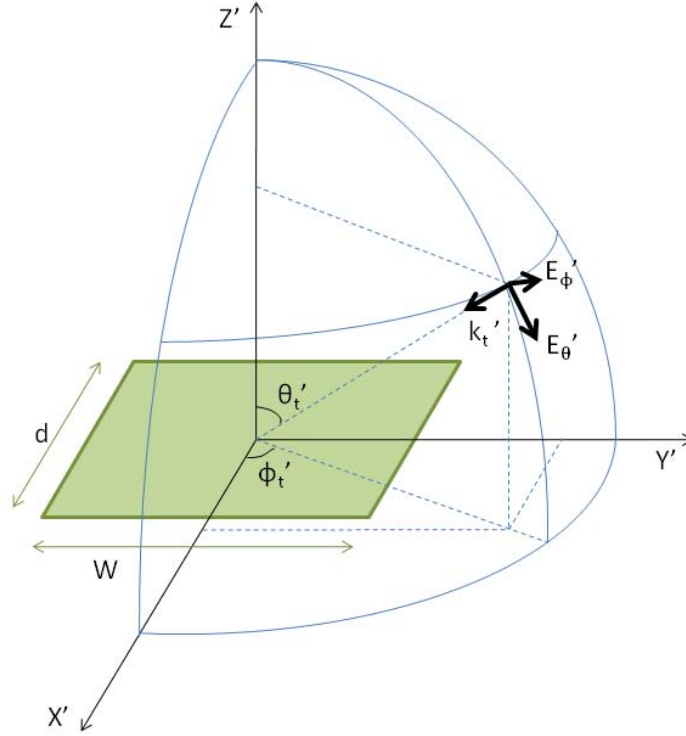


Figure 3.1. Geometry for simple plate centered in XY plane. Prime notation is used to indicate target coordinate system.

components [1].

$$\begin{aligned}
 \vec{A} &= \hat{x}A_x + \hat{y}A_y + \hat{z}A_z && \text{Cartesian} \\
 &= \hat{r}A_r + \hat{\theta}A_\theta + \hat{\phi}A_\phi && \text{Spherical}
 \end{aligned} \tag{3.1}$$

$$\begin{bmatrix} A_r \\ A_\theta \\ A_\phi \end{bmatrix} = \begin{bmatrix} \sin \theta \cos \phi & \sin \theta \sin \phi & \cos \theta \\ \cos \theta \cos \phi & \cos \theta \sin \phi & -\sin \theta \\ -\sin \phi & \cos \phi & 0 \end{bmatrix} \begin{bmatrix} A_x \\ A_y \\ A_z \end{bmatrix} \tag{3.2}$$

$$\begin{bmatrix} A_x \\ A_y \\ A_z \end{bmatrix} = \begin{bmatrix} \sin \theta \cos \phi & \cos \theta \cos \phi & -\sin \phi \\ \sin \theta \sin \phi & \cos \theta \sin \phi & \cos \phi \\ \cos \theta & -\sin \theta & 0 \end{bmatrix} \begin{bmatrix} A_r \\ A_\theta \\ A_\phi \end{bmatrix} \tag{3.3}$$

These transforms are used in the following PO derivation as well as the method to account for arbitrary orientation.

3.2.2 Plate Derivation.

The scattered electric field for an arbitrary field incident upon the PEC plate defined in Section 3.2.1 is derived as follows. This development follows the PO analysis method presented in [6]. The transmit direction unit vector (\hat{k}'_t) and receive unit vector (\hat{r}') for the bistatic configuration are shown in Figure 3.2. The unit vectors and the target surface vector (\vec{r}'') are written in Cartesian coordinates as

$$\hat{k}'_t = -(\hat{x}' \sin \theta'_t \cos \phi'_t + \hat{y}' \sin \theta'_t \sin \phi'_t + \hat{z}' \cos \theta'_t) \quad (3.4)$$

$$\hat{r}' = \hat{x}' \sin \theta'_r \cos \phi'_r + \hat{y}' \sin \theta'_r \sin \phi'_r + \hat{z}' \cos \theta'_r \quad (3.5)$$

$$\vec{r}'' = \hat{x}' x'' + \hat{y}' y'', \quad (3.6)$$

where double-prime notation is used to indicate a vector on the surface of the plate.

Using the far-field assumption [1], the transmit electric field has components orthogonal to \hat{k}'_t and is expressed in spherical coordinates as:

$$\begin{aligned} \vec{E}'_t &= \vec{E}'_{o,t} e^{-j\vec{k}'_t \cdot \vec{r}''} \\ &= (E'_\theta \hat{\theta}'_t + E'_\phi \hat{\phi}'_t) e^{jk(x' \sin \theta'_t \cos \phi'_t + y' \sin \theta'_t \sin \phi'_t + z' \cos \theta'_t)}. \end{aligned} \quad (3.7)$$

The transmit magnetic field is therefore:

$$\begin{aligned} \vec{H}'_t(\vec{r}') &= \frac{\hat{k}'_t \times \vec{E}'_t}{\eta} \\ &= \frac{-1}{\eta} (E'_\theta \hat{\phi}'_t - E'_\phi \hat{\theta}'_t) e^{jk(x' \sin \theta'_t \cos \phi'_t + y' \sin \theta'_t \sin \phi'_t + z' \cos \theta'_t)}. \end{aligned} \quad (3.8)$$

The surface current density induced on the illuminated side of the flat plate is

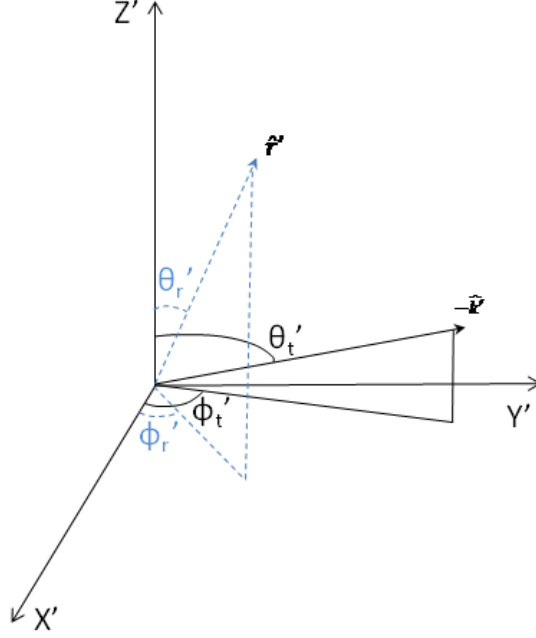


Figure 3.2. Spherical coordinate geometry for bistatic radar configuration. \hat{k}' is the transmit unit vector while \hat{r}' is the receive unit vector. Prime notation is used to indicate target coordinate system.

found by using the PO approximation described in Section 2.3.3. The surface current density is found by:

$$\begin{aligned}
 \vec{J}_s'(\vec{r}') &\approx 2\hat{n}' \times \vec{H}_t'(\vec{r}') \Big|_{z''=0} \\
 &= \frac{-2}{\eta} \hat{z}' \times (E'_\theta \hat{\phi}'_t - E'_\phi \hat{\theta}'_t) e^{jk(x'' \sin \theta'_t \cos \phi'_t + y'' \sin \theta'_t \sin \phi'_t)} \\
 &= \frac{2}{\eta} (E'_\theta (\hat{x}' \cos \phi'_t + \hat{y}' \sin \phi'_t) + E'_\phi (-\hat{x}' \cos \theta'_t \sin \phi'_t \\
 &\quad + \hat{y}' \cos \theta'_t \cos \phi'_t)) e^{jk(x'' \sin \theta'_t \cos \phi'_t + y'' \sin \theta'_t \sin \phi'_t)} \tag{3.9}
 \end{aligned}$$

Now that the surface current is known, the scattered far-field components gener-

ated by \vec{J}'_s are found by first solving for the far-field vector term \vec{N}' [10].

$$\begin{aligned}
\vec{N}' &= \int_S \vec{J}'_s(\vec{r}'') e^{jk\vec{r}' \cdot \vec{r}''} dS' \\
&= \frac{2}{\eta} (E'_\theta(\hat{x}' \cos \phi'_t + \hat{y}' \sin \phi'_t) + E'_\phi(-\hat{x}' \cos \theta'_t \sin \phi'_t + \hat{y}' \cos \theta'_t \cos \phi'_t)) \\
&\quad \int_{-d/2}^{d/2} e^{jx''k(\sin \theta'_r \cos \phi'_r + \sin \theta'_t \cos \phi'_t)} dx'' \int_{-W/2}^{W/2} e^{jy''k(\sin \theta'_r \sin \phi'_r + \sin \theta'_t \sin \phi'_t)} dy'' \quad (3.10)
\end{aligned}$$

The generic solution to integrals of this form is found by: $\int_{-\beta/2}^{\beta/2} e^{j\zeta\alpha} d\zeta = \frac{1}{j\alpha} (e^{\frac{j\beta\alpha}{2}} - e^{-\frac{j\beta\alpha}{2}}) = \frac{j2 \sin \frac{\beta\alpha}{2}}{j\alpha} = \frac{\beta \sin \frac{\beta\alpha}{2}}{\frac{\beta\alpha}{2}} = \beta \text{sinc}(\frac{\beta\alpha}{2})$. Using this relationship, the integrated form of \vec{N}' is:

$$\begin{aligned}
\vec{N}' &= \frac{2Wd}{\eta} \text{sinc}\left(\frac{d}{2}\mathcal{X}\right) \text{sinc}\left(\frac{W}{2}\mathcal{Y}\right) (E'_\theta(\hat{x}' \cos \phi'_t + \hat{y}' \sin \phi'_t) \\
&\quad + E'_\phi(-\hat{x}' \cos \theta'_t \sin \phi'_t + \hat{y}' \cos \theta'_t \cos \phi'_t)) \\
&\quad \text{where } \mathcal{X} = k(\sin \theta'_r \cos \phi'_r + \sin \theta'_t \cos \phi'_t) \\
&\quad \text{and } \mathcal{Y} = k(\sin \theta'_r \sin \phi'_r + \sin \theta'_t \sin \phi'_t). \quad (3.11)
\end{aligned}$$

The transverse of \vec{N}' is designated \vec{N}'_t and is found as:

$$\begin{aligned}
\vec{N}'_t &= \hat{\theta}'(\hat{\theta}' \cdot \vec{N}') + \hat{\phi}'(\hat{\phi}' \cdot \vec{N}') \\
&= \frac{2Wd}{\eta} \text{sinc}\left(\frac{d}{2}\mathcal{X}\right) \text{sinc}\left(\frac{W}{2}\mathcal{Y}\right) \left[\hat{\theta}'(E'_\theta(\cos \theta'_r \cos \phi'_r \cos \phi'_t + \cos \theta'_r \sin \phi'_r \sin \phi'_t) \right. \\
&\quad + E'_\phi(-\cos \theta'_r \cos \phi'_r \cos \theta'_t \sin \phi'_t + \cos \theta'_r \sin \phi'_r \cos \theta'_t \cos \phi'_t)) \\
&\quad + \hat{\phi}'(E'_\theta(-\sin \phi'_r \cos \phi'_t + \cos \phi'_r \sin \phi'_t) + E'_\phi(\sin \phi'_r \cos \theta'_t \sin \phi'_t \\
&\quad \left. + \cos \phi'_r \cos \theta'_t \cos \phi'_t)) \right]. \quad (3.12)
\end{aligned}$$

Finally, the scattered field is found, with the $\frac{e^{-jkr}}{r}$ propagation term accounted

for and suppressed, as:

$$\begin{aligned}
\vec{E}'_{s,xy} &= \frac{-jk\eta\vec{N}'_t}{4\pi} \\
&= \frac{-jkWd}{2\pi} \operatorname{sinc}\left(\frac{d}{2}\mathcal{X}\right) \operatorname{sinc}\left(\frac{W}{2}\mathcal{Y}\right) \left[\hat{\theta}'(E'_\theta(\cos\theta'_r \cos\phi'_r \cos\phi'_t \right. \\
&\quad + \cos\theta'_r \sin\phi'_r \sin\phi'_t) + E'_\phi(-\cos\theta'_r \cos\phi'_r \cos\theta'_t \sin\phi'_t \\
&\quad + \cos\theta'_r \sin\phi'_r \cos\theta'_t \cos\phi'_t)) + \hat{\phi}'(E'_\theta(-\sin\phi'_r \cos\phi'_t \\
&\quad + \cos\phi'_r \sin\phi'_t) + E'_\phi(\sin\phi'_r \cos\theta'_t \sin\phi'_t \\
&\quad \left. + \cos\phi'_r \cos\theta'_t \cos\phi'_t)) \right] \text{ for } \begin{cases} \theta'_r < 90^\circ & \text{if } \theta'_t < 90^\circ, \\ \theta'_r > 90^\circ & \text{if } \theta'_t > 90^\circ, \end{cases} \\
&\quad 0 \text{ otherwise.} \tag{3.13}
\end{aligned}$$

While Equation (3.13) is of the form useful for applying arbitrary orientation and position changes to be described in Section 3.4, the derivation is typically taken one step further by organizing into co/cross-pol scattering. In this form, V indicates vertical polarization (θ -pol), H indicates horizontal polarization (ϕ -pol), and the first subscript indicates receiver polarization while the second subscript indicates transmitter polarization. The co/cross-pol PO solution for bistatic scattering from a simple

plate is given as:

$$\vec{E}'_{VV,xy} = \frac{-jkWd}{2\pi} \text{sinc}\left(\frac{d}{2}\mathcal{X}\right) \text{sinc}\left(\frac{W}{2}\mathcal{Y}\right) (\cos\theta'_r \cos\phi'_r \cos\phi'_t + \cos\theta'_r \sin\phi'_r \sin\phi'_t) \quad (3.14a)$$

$$\vec{E}'_{HV,xy} = \frac{-jkWd}{2\pi} \text{sinc}\left(\frac{d}{2}\mathcal{X}\right) \text{sinc}\left(\frac{W}{2}\mathcal{Y}\right) (-\sin\phi'_r \cos\phi'_t + \cos\phi'_r \sin\phi'_t) \quad (3.14b)$$

$$\begin{aligned} \vec{E}'_{VH,xy} = \frac{-jkWd}{2\pi} \text{sinc}\left(\frac{d}{2}\mathcal{X}\right) \text{sinc}\left(\frac{W}{2}\mathcal{Y}\right) & (-\cos\theta'_r \cos\phi'_r \cos\theta'_t \sin\phi'_t \\ & + \cos\theta'_r \sin\phi'_r \cos\theta'_t \cos\phi'_t) \end{aligned} \quad (3.14c)$$

$$\vec{E}'_{HH,xy} = \frac{-jkWd}{2\pi} \text{sinc}\left(\frac{d}{2}\mathcal{X}\right) \text{sinc}\left(\frac{W}{2}\mathcal{Y}\right) (\sin\phi'_r \cos\theta'_t \sin\phi'_t + \cos\phi'_r \cos\theta'_t \cos\phi'_t) \quad (3.14d)$$

As shown in Equation (3.13), the PO bistatic 3D closed form solution for a simple plate centered in the XY plane is a function of the size of the plate (W, d), radar frequency (k), transmit and receive angles ($\theta'_t, \phi'_t, \theta'_r, \phi'_r$), as well as the polarization of the transmit signal, (E'_θ, E'_ϕ). Figures which compare this closed form solution to simulated data are provided in Appendix Section 1.1.1.

3.3 Bistatic 3D GO-PO Solution for Dihedral

This section will summarize the closed-form bistatic 3D GO-PO solution computed in [12] for scattering from the interior of a dihedral at fixed orientation. Section 3.3.1 contains information on the dihedral orientation used for this derivation, while Section 3.3.2 summarizes the derivation.

3.3.1 Dihedral Geometry.

The fixed dihedral geometry for this analysis is shown in Figure 3.3. The dihedral is centered vertically with its seam along the z' axis and its two plates aligned with

the x' and y' axes. This is referred to as the ‘original’ orientation when discussing orientation changes in Section 3.4. In this case, \hat{x}' is the unit vector normal to the YZ plate’s surface while \hat{y}' is normal to the XZ plate’s surface. The bistatic TX/RX geometry is the same as shown in Figure 3.2.

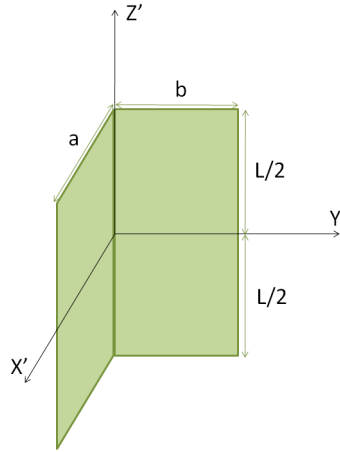


Figure 3.3. Dihedral geometry. L indicates height of the dihedral while a, b are the width of each of the plates. Prime notation used to indicate target coordinate system.

3.3.2 Dihedral Derivation.

The dihedral scattering solution is separated into three terms: two first order scattering terms from the vertically orientated plates in the YZ and XZ planes, and a second order scattering term for the double bounce that reflects from one plate to the other and then to the receiver. It is valid for aspect angles within the interior of the dihedral ($0^\circ \leq \phi'_t \leq 90^\circ, 0^\circ \leq \phi'_r \leq 90^\circ$). The PO solutions for the first order terms are derived in a similar manner as the solution for a simple plate centered in the XY plane described in Section 3.2.2. The first order scattering from the plate in

the XZ plane is [12]:

$$\begin{aligned}\vec{E}'_{xz1} &= \frac{jkaL}{2\pi} \operatorname{sinc}\left(\frac{L}{2}\mathcal{Z}\right) \operatorname{sinc}\left(\frac{a}{2}\mathcal{X}\right) e^{\frac{ja}{2}\mathcal{X}} \left(\hat{\theta}'_r (E'_\theta \sin \theta'_r \sin \phi'_t \right. \\ &\quad \left. - E'_\phi (\cos \theta'_r \cos \phi'_r \sin \theta'_t - \cos \theta'_t \cos \phi'_t \sin \theta'_r)) + \hat{\phi}'_r E'_\phi \sin \theta'_t \sin \phi'_r \right) \\ &\quad \text{where } \mathcal{X} = k (\sin \theta'_r \cos \phi'_r + \sin \theta'_t \cos \phi'_t) \\ &\quad \text{and } \mathcal{Z} = k (\cos \theta'_r + \cos \theta'_t)\end{aligned}\tag{3.15}$$

and similarly the first-order scattering from the plate in the YZ plane is [12]:

$$\begin{aligned}\vec{E}'_{yz1} &= \frac{-jkbL}{2\pi} \operatorname{sinc}\left(\frac{L}{2}\mathcal{Z}\right) \operatorname{sinc}\left(\frac{b}{2}\mathcal{Y}\right) e^{\frac{ib}{2}\mathcal{Y}} \left(\hat{\theta}'_r (E'_\theta \sin \theta'_r \cos \phi'_t \right. \\ &\quad \left. - E'_\phi (\cos \theta'_t \sin \phi'_t \sin \theta'_r - \cos \theta'_r \sin \phi'_r \sin \theta'_t)) + \hat{\phi}'_r E'_\phi \sin \theta'_t \cos \phi'_r \right) \\ &\quad \text{where } \mathcal{Y} = k (\sin \theta'_r \sin \phi'_r + \sin \theta'_t \sin \phi'_t)\end{aligned}\tag{3.16}$$

where prime indicates target domain coordinates.

There is one second order, double bounce scattering term for the dihedral. The ray reflection from the first plate is traced to determine the angle of incidence on the second plate, then the PO integral is found in a similar manner to Section 3.2.2, with different limits of integration. The limits depend on the order in which the plates are illuminated, the size of the two plates, and the transmit antenna's aspect angle. The PO scattered field for the double bounce mechanism is [12]:

$$\begin{aligned}\vec{E}'_2 &= \frac{-jk}{2\pi} \left(\hat{\theta}'_r \left(E'_\theta \sin \theta'_r (\mathcal{I}_{xz} \sin \phi'_t + \mathcal{I}_{yz} \cos \phi'_t) \right. \right. \\ &\quad \left. \left. + E'_\phi (\sin \theta'_t \cos \theta'_r (\mathcal{I}_{xz} \cos \phi'_r - \mathcal{I}_{yz} \sin \phi'_r) + \cos \theta'_t \sin \theta'_r (\mathcal{I}_{xz} \cos \phi'_t - \mathcal{I}_{yz} \sin \phi'_t)) \right) \right. \\ &\quad \left. - \hat{\phi}'_r E'_\phi \sin \theta'_t (\mathcal{I}_{xz} \sin \phi'_r + \mathcal{I}_{yz} \cos \phi'_r) \right)\end{aligned}\tag{3.17}$$

where \mathcal{I}_{xz} and \mathcal{I}_{yz} represent the integral term for the PO integral. Depending on

the transmit aspect angle and the size of the plates which compose the dihedral, the reflected field from one plate either partially or fully illuminates the other plate, resulting in different limits for these integral terms. Using GO to trace ray reflections there are six cases for illuminating the dihedral corner, with cases 1-3 corresponding to $0^\circ \leq \theta'_t \leq 90^\circ$ and 4-6 to $90^\circ \leq \theta'_t \leq 180^\circ$. The closed form solutions to the PO integrals for the six cases can be written as [12]:

$$\begin{aligned}
\mathcal{I}_{xz}^{1,2,3} &= \int_0^{\mathcal{X}} \int_{-\frac{L}{2}}^{\frac{L}{2}-x'' \frac{\cot \theta'_t}{\cos \phi'_t}} e^{-j(x''\mathcal{X}-z''\mathcal{Z})} dz'' dx'' \\
&= \frac{e^{j\frac{L}{2}\mathcal{Z}}}{j\mathcal{Z}} \mathbf{X} \operatorname{sinc}\left(\frac{\mathbf{X}}{2}\left(\mathcal{X} + \mathcal{Z} \frac{\cot \theta'_t}{\cos \phi'_t}\right)\right) e^{-j\frac{\mathbf{X}}{2}\left(\mathcal{X} + \mathcal{Z} \frac{\cot \theta'_t}{\cos \phi'_t}\right)} - \frac{e^{-j\frac{L}{2}\mathcal{Z}}}{j\mathcal{Z}} \mathbf{X} \operatorname{sinc}\left(\frac{\mathbf{X}}{2}\mathcal{X}\right) e^{-j\frac{\mathbf{X}}{2}\mathcal{X}}
\end{aligned} \tag{3.18}$$

$$\begin{aligned}
\mathcal{I}_{yz}^{1,2,3} &= \int_0^{\mathcal{Y}} \int_{-\frac{L}{2}}^{\frac{L}{2}-y'' \frac{\cot \theta'_t}{\sin \phi'_t}} e^{-j(y''\mathcal{Y}-z''\mathcal{Z})} dz'' dy'' \\
&= \frac{e^{j\frac{L}{2}\mathcal{Z}}}{j\mathcal{Z}} \mathbf{Y} \operatorname{sinc}\left(\frac{\mathbf{Y}}{2}\left(\mathcal{Y} + \mathcal{Z} \frac{\cot \theta'_t}{\sin \phi'_t}\right)\right) e^{-j\frac{\mathbf{Y}}{2}\left(\mathcal{Y} + \mathcal{Z} \frac{\cot \theta'_t}{\sin \phi'_t}\right)} - \frac{e^{-j\frac{L}{2}\mathcal{Z}}}{j\mathcal{Z}} \mathbf{Y} \operatorname{sinc}\left(\frac{\mathbf{Y}}{2}\mathcal{Y}\right) e^{-j\frac{\mathbf{Y}}{2}\mathcal{Y}}
\end{aligned} \tag{3.19}$$

$$\begin{aligned}
\mathcal{I}_{xz}^{4,5,6} &= \int_0^{\mathcal{X}} \int_{-\frac{L}{2}-x'' \frac{\cot \theta'_t}{\cos \phi'_t}}^{\frac{L}{2}} e^{-j(x''\mathcal{X}-z''\mathcal{Z})} dz'' dx'' \\
&= \frac{e^{j\frac{L}{2}\mathcal{Z}}}{j\mathcal{Z}} \mathbf{X} \operatorname{sinc}\left(\frac{\mathbf{X}}{2}\mathcal{X}\right) e^{-j\frac{\mathbf{X}}{2}\mathcal{X}} - \frac{e^{-j\frac{L}{2}\mathcal{Z}}}{j\mathcal{Z}} \mathbf{X} \operatorname{sinc}\left(\frac{\mathbf{X}}{2}\left(\mathcal{X} + \mathcal{Z} \frac{\cot \theta'_t}{\cos \phi'_t}\right)\right) e^{-j\frac{\mathbf{X}}{2}\left(\mathcal{X} + \mathcal{Z} \frac{\cot \theta'_t}{\cos \phi'_t}\right)}
\end{aligned} \tag{3.20}$$

$$\begin{aligned}
\mathcal{I}_{yz}^{4,5,6} &= \int_0^{\mathcal{Y}} \int_{-\frac{\mathcal{L}}{2} - y'' \frac{\cot \theta'_t}{\sin \phi'_t}}^{\frac{\mathcal{L}}{2}} e^{-j(y''\mathcal{Y} - z''\mathcal{Z})} dz'' dy'' \\
&= \frac{e^{j\frac{\mathcal{L}}{2}\mathcal{Z}}}{j\mathcal{Z}} \mathcal{Y} \operatorname{sinc}\left(\frac{\mathcal{Y}}{2}\mathcal{Y}\right) e^{-j\frac{\mathcal{Y}}{2}\mathcal{Y}} - \frac{e^{-j\frac{\mathcal{L}}{2}\mathcal{Z}}}{j\mathcal{Z}} \mathcal{Y} \operatorname{sinc}\left(\frac{\mathcal{Y}}{2}\left(\mathcal{Y} + \mathcal{Z} \frac{\cot \theta'_t}{\sin \phi'_t}\right)\right) e^{-j\frac{\mathcal{Y}}{2}\left(\mathcal{Y} + \mathcal{Z} \frac{\cot \theta'_t}{\sin \phi'_t}\right)}
\end{aligned} \tag{3.21}$$

where superscripts 1,2,3 and 4,5,6 indicate illumination cases 1-3 and 4-6, respectively, and double prime notation indicates target surface coordinates. Variables \mathcal{X}, \mathcal{Y} , and \mathcal{Z} are defined in Equations (3.15) and (3.16), and the terms \mathcal{X} and \mathcal{Y} are the upper limits of integration on x' and y' . The limits of integration are unique to each illumination case and are given in [12]. Singularities when $\mathcal{Z} = 0$ are avoided by implementing L'Hopital's rule to find the limiting equations in the numerical calculation of Equations (3.18)-(3.21). These limiting equations are [12]:

$$\lim_{\mathcal{Z} \rightarrow 0} \mathcal{I}_{xz} = \left(L\mathcal{X} \mp \frac{\mathcal{X}^2 \cot \theta'_t}{2 \cos \phi'_t} \right) \operatorname{sinc}\left(\frac{\mathcal{X}}{2}\mathcal{X}\right) e^{-j\frac{\mathcal{X}}{2}\mathcal{X}} \pm \frac{\mathcal{X} \cot \theta'_t}{j\mathcal{X} \cos \phi'_t} \left(\cos \frac{\mathcal{X}}{2}\mathcal{X} - \operatorname{sinc}\left(\frac{\mathcal{X}}{2}\mathcal{X}\right) \right) e^{-j\frac{\mathcal{X}}{2}\mathcal{X}} \tag{3.22}$$

$$\lim_{\mathcal{Z} \rightarrow 0} \mathcal{I}_{yz} = \left(L\mathcal{Y} \mp \frac{\mathcal{Y}^2 \cot \theta'_t}{2 \sin \phi'_t} \right) \operatorname{sinc}\left(\frac{\mathcal{Y}}{2}\mathcal{Y}\right) e^{-j\frac{\mathcal{Y}}{2}\mathcal{Y}} \pm \frac{\mathcal{Y} \cot \theta'_t}{j\mathcal{Y} \sin \phi'_t} \left(\cos \frac{\mathcal{Y}}{2}\mathcal{Y} - \operatorname{sinc}\left(\frac{\mathcal{Y}}{2}\mathcal{Y}\right) \right) e^{-j\frac{\mathcal{Y}}{2}\mathcal{Y}} \tag{3.23}$$

where the upper sign applies for cases 1-3 and lower sign applies for cases 4-6. However, singularities also exist in Equations (3.22) and (3.23) when $\mathcal{X} = 0$ and $\mathcal{Y} = 0$, respectively. In the case that both \mathcal{Z} and either \mathcal{X} or $\mathcal{Y} = 0$, the limiting equations are [12]:

$$\lim_{\mathcal{X} \rightarrow 0} \left(\lim_{\mathcal{Z} \rightarrow 0} \mathcal{I}_{xz} \right) = L\mathcal{X} \mp \frac{\mathcal{X}^2 \cot \theta'_t}{2 \cos \phi'_t} \tag{3.24}$$

$$\lim_{\mathcal{Y} \rightarrow 0} \left(\lim_{\mathcal{Z} \rightarrow 0} \mathcal{I}_{yz} \right) = L\mathcal{Y} \mp \frac{\mathcal{Y}^2 \cot \theta'_t}{2 \sin \phi'_t} \tag{3.25}$$

Equations (3.17)-(3.25) define the double bounce term. The total scattered field

for a dihedral is the sum of the two first order terms and the double bounce term:

$$\vec{E}'_{\text{total}} = \begin{cases} \vec{E}'_{xz^1} + \vec{E}'_{xy^1} + \vec{E}'_2 & \text{for } 0^\circ \leq \phi'_t \leq 90^\circ, 0^\circ \leq \phi'_r \leq 90^\circ, \\ 0 & \text{otherwise} \end{cases} \quad (3.26)$$

where the ϕ' aspect boundaries indicate the solution is valid for the interior of the dihedral. As in the simple plate PO derivation, Equation (3.26) is of the form useful for applying arbitrary orientation and position changes as described in the following section. Typically, the solution is taken one step farther by separating the total scattered field into co/cross-pol scattering equations. These equations are provided in Appendix B due to the size of the equations.

At this point, the GO-PO solution derived in [12] for the total scattered field for a dihedral at the orientation and position shown in Figure 3.3 is summarized. Results and validation with comparisons to simulated data generated by SBR and MoM based electromagnetic codes are provided in Chapter IV. The following section will derive a method to extend this bistatic 3D GO-PO solution to arbitrary orientation and position.

3.4 Extension to Arbitrary Orientation and Position

This section will explain a method to calculate the electromagnetic scattering from an arbitrarily orientated and positioned plate or dihedral using the bistatic 3D solutions for these objects defined in Sections 3.2.2 and 3.3, respectively. An example using the plate is shown in Figure 3.4.

The order in which changes to orientation and position are applied is important. Applying changes to position prior to orientation will result in a significantly different target configuration than applying changes to orientation followed by position. The following method employs the latter definition, i.e. apply arbitrary orientation then

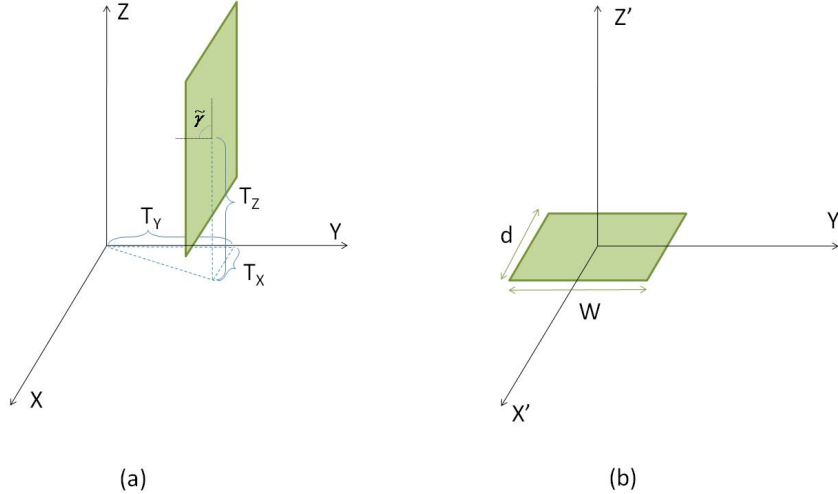


Figure 3.4. (a) Global coordinate system, (b) computation domain coordinate system. The real-world target’s orientation is offset from the computation domain by some rotation angle, in this case a roll angle of $\tilde{\gamma} = -90^\circ$. Also, the position is offset from the scene origin by Cartesian components T_x, T_y, T_z . The response from (a) can be found using a closed-form PO solution based on (b). Prime notation is used to indicate computation (target) domain coordinate system.

arbitrary position. The organization of this section follows this order: Section 3.4.1 will explain arbitrary orientation and Section 3.4.2 will explain arbitrary position. This section closes with a flowchart summarizing this method in Section 3.4.3.

3.4.1 Orientation.

The high-level approach to account for arbitrary orientation is to first modify the global TX/RX aspect angles and transmit electric field vector components into calculation (target) domain angles and vector components. Next, the calculation domain scattering response is calculated using the plate or dihedral scattering equations in Equations (3.13) and (3.26), respectively. Finally, the resulting calculation domain scattered electric field vector components are modified into global scattered electric field components. The details of this method are described in this section.

The first step when designing a method to account for arbitrary orientation is to define the order of rotations. For example, applying 30° rotations in the order zyx

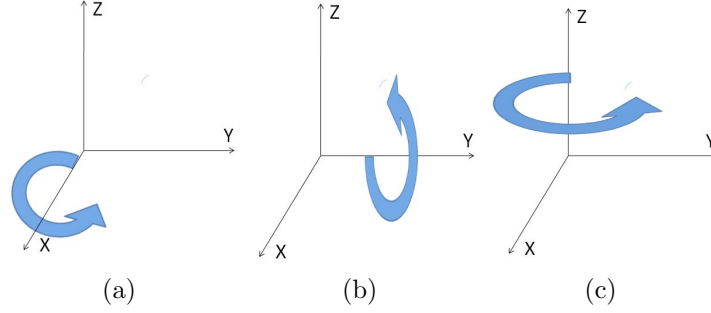


Figure 3.5. (a) Roll, (b) pitch, (c) yaw right-handed rotations. Rotation about all three axes is applied in the order roll, pitch, then yaw.

does not produce the same result as applying the same 30° rotations in the order xyz . In this thesis, rotation is applied in the latter order, and the 3×3 rotation matrix as a function of roll ($\tilde{\gamma}$), pitch ($\tilde{\theta}$), and yaw ($\tilde{\phi}$) rotations shown in Figure 3.5 is defined as: $\mathbf{R}(\tilde{\phi}, \tilde{\theta}, \tilde{\gamma}) = \mathbf{R}_z(\tilde{\phi})\mathbf{R}_y(\tilde{\theta})\mathbf{R}_x(\tilde{\gamma})$ where $\mathbf{R}_z, \mathbf{R}_y, \mathbf{R}_x$ are the 3×3 rotation matrixes corresponding to right-handed rotation about the subscripted axis and are defined as

$$\begin{aligned} \mathbf{R}(\tilde{\phi}, \tilde{\theta}, \tilde{\gamma}) &= \mathbf{R}_z(\tilde{\phi})\mathbf{R}_y(\tilde{\theta})\mathbf{R}_x(\tilde{\gamma}) \\ &= \begin{bmatrix} \cos \tilde{\phi} & -\sin \tilde{\phi} & 0 \\ \sin \tilde{\phi} & \cos \tilde{\phi} & 0 \\ 0 & 0 & 1 \end{bmatrix} \begin{bmatrix} \cos \tilde{\theta} & 0 & \sin \tilde{\theta} \\ 0 & 1 & 0 \\ -\sin \tilde{\theta} & 0 & \cos \tilde{\theta} \end{bmatrix} \begin{bmatrix} 1 & 0 & 0 \\ 0 & \cos \tilde{\gamma} & -\sin \tilde{\gamma} \\ 0 & \sin \tilde{\gamma} & \cos \tilde{\gamma} \end{bmatrix} \quad (3.27) \end{aligned}$$

Multiplying a cartesian column vector or point in 3D space by the rotation matrix \mathbf{R} will rotate the vector or point about the origin, while multiplying by \mathbf{R}^{-1} will rotate the coordinate system about the origin. A useful method to check the validity of each of the above 3×3 rotation matrixes ($\mathbf{R}, \mathbf{R}_x, \mathbf{R}_y, \mathbf{R}_z$) is to use the rotation matrix identity $\det(\mathbf{R}) = 1$, i.e. the rotation matrix is orthogonal and does not affect the length of the vector rotated.

Using the above rotation matrix, the next step is to convert the real-world transmit and receive angles ($\theta_t, \phi_t, \theta_r, \phi_r$) to computational domain coordinate system ($\theta'_t, \phi'_t, \theta'_r, \phi'_r$)

angles. This is performed by first applying a spherical-to-Cartesian conversion. Then the coordinate system is rotated by multiplying the Cartesian coordinates in 3x1 column form by the inverse rotation matrix \mathbf{R}^{-1} . Finally, the rotated vector is converted back to spherical coordinates. The spherical-to-Cartesian conversions are performed using Equation (3.28), while one may convert back to spherical values using Equation (3.29):

$$\begin{bmatrix} x \\ y \\ z \end{bmatrix} = \begin{bmatrix} \sin \theta \cos \phi \\ \sin \theta \sin \phi \\ \cos \theta \end{bmatrix} \quad (3.28)$$

$$\theta = \arccos\left(\frac{z}{\sqrt{x^2 + y^2 + z^2}}\right) \quad \text{and} \quad \phi = \arctan\left(\frac{y}{x}\right). \quad (3.29)$$

This step of converting the real-world angles into calculation domain angles is summarized in step 2 of the flow chart in Figure 3.7.

Now that the real-world TX/RX angles have been converted to calculation domain angles, the TX electric field components must also be converted. This is performed using the component conversions defined in Equations (3.2) and (3.3) by converting the spherical components (E_θ, E_ϕ) to Cartesian components (E_x, E_y, E_z) , applying the inverse rotation matrix \mathbf{R}^{-1} , then converting these calculation domain Cartesian components (E'_x, E'_y, E'_z) back to spherical components (E'_θ, E'_ϕ) using the calculation domain transmit angles (θ'_t, ϕ'_t) . For real-world transmit electric field strength of 1 V/m, this conversion will result in some scaled value between ± 1 V/m for E'_θ and E'_ϕ which is dependent on the real-world transmit polarization and target orientation and where $\sqrt{E'^2_\theta + E'^2_\phi} = 1$ V/m. This step is applied separately for real-world θ and ϕ polarizations and is summarized in step 3 of Figure 3.7. An example of the conversions for the TX/RX angles and electric field components for the scene shown in Figure 3.4 is given in Figure 3.6.

The above calculation domain angles and TX electric field components are used

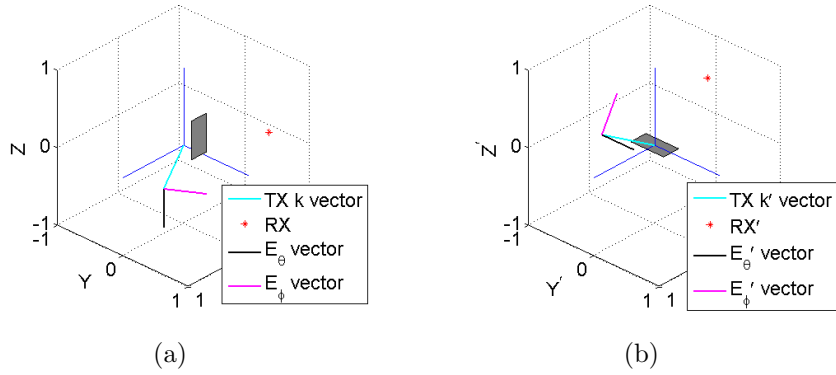


Figure 3.6. Electric field vector conversion. (a) Global coordinate system, (b) calculation domain coordinate system. For $(\theta_t, \phi_t) = (90^\circ, 30^\circ)$ and real-world target orientation at roll $= -90^\circ$ from the original scattering solution, a vertical polarization component of 1 V/m in the global domain is converted to a local horizontal component of 1 V/m in the calculation domain. Likewise, a global horizontal polarization component of 1 V/m is converted to a vertical component of -1 V/m in the calculation domain.

to find the calculation domain scattered field (\vec{E}'_s) using the applicable closed-form scattering solutions explained in Sections 3.2.2 and 3.3. The boundaries of the local scattering solutions in Equations (3.13) and (3.26) are applied using the calculation domain TX/RX angles. This is summarized in step 4 of Figure 3.7.

Finally, \vec{E}'_s is converted back into real-world scattering by using Equation (3.3) to convert the calculation domain θ' and ϕ' components to Cartesian components, applying the rotation matrix \mathbf{R} , then converting the resulting real-world Cartesian components to spherical components using Equation (3.2). This is performed separately for each real-world transmit polarization. The resulting spherical components are the polarized scattering solutions for the real-world target orientated at arbitrary roll, pitch, and yaw. This last step is summarized in step 5 of the flow chart in Figure 3.7. Validation examples for the dihedral with changes to orientation only are provided in Sections 4.4.2 and 4.5.

3.4.2 Position.

This section will explain a method to account for arbitrary target position in 3D space. Arbitrary position change from the scene origin produces an e^{jP} phase term where P is dependent on wavenumber k , the position offset from the scene center, and a sinusoidal term which accounts for 3D transmit and receive aspect angles. Multiplying the scattered field by these phase terms will accurately represent a target at arbitrary position. The following will explain the derivation of the sinusoidal phase terms.

Translation from the origin along the x and y axis can be derived by examining the bistatic 3D plate solution. The phase terms along these axes are directly related to the \mathcal{X} and \mathcal{Y} terms in Equation (3.11). This is because instead of the $\int_{-d/2}^{d/2} dx'$ and $\int_{-W/2}^{W/2} dy'$ integral bounds in Equation (3.10), the bounds in the real-world scene are actually $\int_{T_x-d/2}^{T_x+d/2} dx'$ and $\int_{T_y-W/2}^{T_y+W/2} dy'$, where T_x and T_y are translation distances in meters along the x and y axes from the original target positions shown in Figures 3.1 and 3.3. The generic solution for integrals of this form is shown to be:

$$\begin{aligned}
 \int_{A-\beta/2}^{A+\beta/2} e^{j\zeta\alpha} d\zeta &= \frac{1}{j\alpha} (e^{j\alpha(A+\frac{\beta}{2})} - e^{j\alpha(A-\frac{\beta}{2})}) \\
 &= \frac{1}{j\alpha} (e^{\frac{j\alpha\beta}{2}} - e^{-\frac{j\alpha\beta}{2}}) e^{jA\alpha} \\
 &= \frac{j2 \sin \frac{\alpha\beta}{2}}{j\alpha} e^{jA\alpha} \\
 &= \beta \operatorname{sinc}\left(\frac{\alpha\beta}{2}\right) e^{jA\alpha}.
 \end{aligned} \tag{3.30}$$

Using this equality and Equation (3.11), the phase term is found to vary as $e^{jkT_x(\sin \theta_r \cos \phi_r + \sin \theta_t \cos \phi_t)}$ for translation along the x axis and $e^{jkT_y(\sin \theta_r \sin \phi_r + \sin \theta_t \sin \phi_t)}$ for translation along the y axis.

The proof for the phase term for z translation is slightly different. Instead of

changing the surface integral bounds, the target surface vector in Equation (3.4) is changed to $\vec{r}'' = \hat{x}'x'' + \hat{y}'y'' + \hat{z}'T_z$ where T_z is translation from the origin along the z axis. This produces two changes to the PO derivation described in Section 3.2.2. First, the surface current density in Equation (3.9) is evaluated at $z'' = T_z$, not $z'' = 0$, resulting in an additional $e^{jkT_z \cos \theta'_t}$ term for $\vec{J}'_s(\vec{r}'')$. Also, the dot product $\hat{r}' \cdot \vec{r}''$ in Equation (3.10) produces an additional $e^{jkT_z \cos \theta'_r}$ term in \vec{N}' . The result is a phase term of $e^{jkT_z(\cos \theta_r + \cos \theta_t)}$ for translation along the z axis.

The resulting phase terms to account for arbitrary position are:

$$x \text{ translation: } e^{jkT_x(\sin \theta_r \cos \phi_r + \sin \theta_t \cos \phi_t)} \quad (3.31a)$$

$$y \text{ translation: } e^{jkT_y(\sin \theta_r \sin \phi_r + \sin \theta_t \sin \phi_t)} \quad (3.31b)$$

$$z \text{ translation: } e^{jkT_z(\cos \theta_r + \cos \theta_t)}. \quad (3.31c)$$

Multiplying the scattered field by these phase terms will produce an accurate prediction of the real-world scattering behavior. This step is summarized in step 6 of the flow chart in Figure 3.7. Example cases with position offsets from the scene origin are examined for the dihedral and plate in Section 4.4 and Appendix Section 1.1.2, respectively.

3.4.3 Flow Chart.

This section presents the complete method for accounting for arbitrary orientation and position in flow chart form. This flow chart is given in Figure 3.7. A detailed explanation of the steps is given in the preceding sections, 3.4.1 and 3.4.2.

The method summarized by the flow chart in Figure 3.7 is to first begin with a scattering solution for the applicable target in a defined orientation and position. Second, convert the real-world angles to computation domain angles. Third, convert

the real-world electric field components to calculation domain components. Fourth, find the calculation domain scattering. Fifth, convert the calculation domain scattering back into real-world scattering. The sixth and final step is to apply a phase shift to account for offset from the defined target position. This method is designed to be extendable to any scattering solution organized as a function of spherical transmit polarizations (E_θ, E_ϕ) .

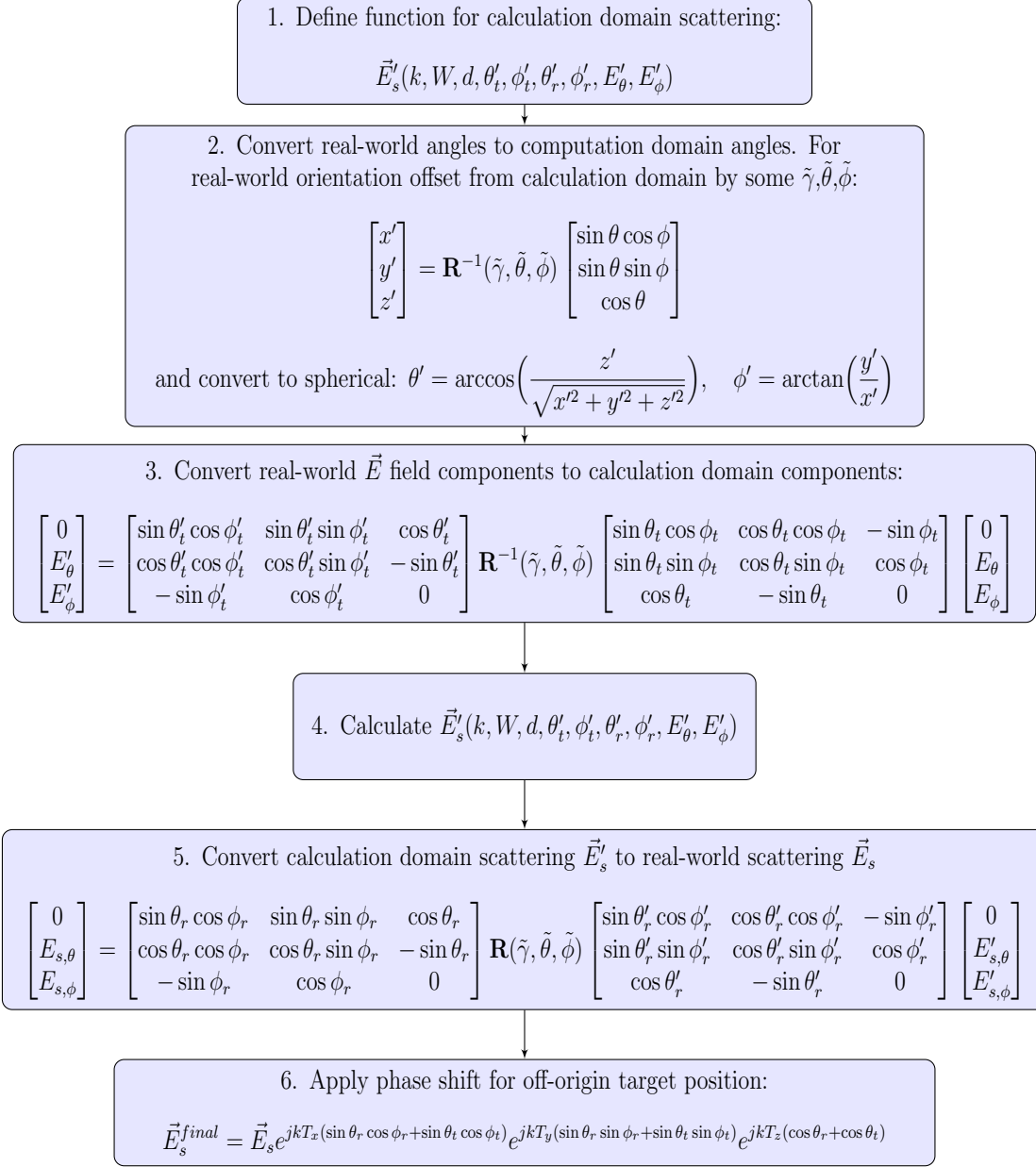


Figure 3.7. Flow chart for computing scattering for arbitrary orientation and position.

3.5 Chapter Summary

This chapter began by providing the bistatic 3D scattering solutions for both the simple plate and dihedral target at defined orientations and positions. It then explained a method to extend these solutions to arbitrary target orientation and position. The resulting method is capable of generating accurate scattering data for a dihedral or flat plate at any orientation or position within a scene in significantly less time than predictive software based on SBR or MoM solutions. Data generated using this method and comparisons to simulated data produced using SBR and MoM based software as well as measurements in the AFIT RCS range are given in Chapter IV and Appendix A.

IV. Results

4.1 Chapter Overview

This chapter presents data obtained through simulations and experimental measurements. Results comparing the model developed in this thesis against both SBR and MoM predictions are given. Comparisons against measured data and the 3D parametric model developed in [13] are also provided in some cases. Additional comparisons for flat plate targets can be found in the appendix.

This chapter is organized as follows. First, an overview of how scattering data is displayed and how the prediction methods are compared quantitatively is presented in Section 4.2. In order to become familiar with the performance of the closed-form GO-PO solution for the dihedral which the model developed in this thesis is based on, a dihedral at original orientation and position is examined in Section 4.3. Following this, results showcasing the orientation and position transforms central to this thesis are provided in Section 4.4. First, in Section 4.4.1, a case is presented where the dihedral is positioned with changes to all six possible parameters - roll, pitch, yaw, and translation along the x , y , and z axes. Model, SBR, and MoM predictions are presented and compared for these cases. Second, in Section 4.4.2, two cases are presented which contrast the model in this thesis with measured data collected in the AFIT RCS range and the 3D parametric model developed in [13]. Finally, in Section 4.5, model, SBR, and MoM data is presented and compared for dihedral orientations commonly used for calibration purposes. Section 4.6 includes a summary of computation times for the cases examined in this chapter.

4.2 Data Presentation

This section discusses how scattering data and differences between model, SBR, and MoM data is presented in this chapter. Because the model in this thesis is intended to be accurate for 3D TX/RX angles (i.e. not restricted to waterline or constant azimuth position), verification cannot be fully accomplished solely by traditional RCS plots which typically present data for an azimuth sweep at constant elevation or frequency sweep for constant TX/RX position. Data presented in this chapter is given as the RCS magnitude for a $(\theta_r, \phi_r) = (\pm 20^\circ, \pm 20^\circ)$ window centered around the peak forward scatter response for a single transmitter aspect. Angular step-size is 0.1° for both θ_r and ϕ_r . As a subset of this data, traditional magnitude and phase plots are presented for an azimuth sweep with constant θ_r , where θ_r is chosen to intersect the peak response in the scene. A single frequency is used (10GHz), and the dihedral dimensions are $L=0.5\text{m}$ (16.67λ), $a=b=0.25\text{m}$ (8.33λ). The exception to this is for the comparisons to measured data in Section 4.4.2, where the dihedral dimensions are $L=15.24\text{cm}$ (5.08λ), $a=b=7.62\text{cm}$ (2.54λ).

The RCS dynamic range for the following figures is -20 to 30 dBsm. This scale is used primarily to focus on the forward scatter mainlobe and first few sidelobes. Both potential applications of the model developed in this thesis, bistatic SAR and airborne SAR calibration, require accurate mainlobe modeling but are not dependent on sidelobe accuracy [13]. Also, PO-based techniques are known to be inaccurate for significantly off-specular angles [16]. For these reasons, values less than -20 dBsm are not examined in this thesis.

In order to consider both magnitude and phase accuracy between model, SBR, and MoM data, two types of comparison plots are presented. The first is termed coherent difference and is given in dBsm. The second is named magnitude ratio and is given in dB.

Coherent difference is defined as $20 \log_{10} |\sqrt{\sigma_1} - \sqrt{\sigma_2}|$ where $\sqrt{\sigma_1}$ and $\sqrt{\sigma_2}$ contain the magnitude and phase data for the prediction models being examined. It is indicated in the following charts by “|Model-SBR|” or “|Model-MoM|” and is presented on the same dBsm scale as the scattering data. A ‘good’ coherent difference value is determined with respect to the scattering amplitude for the polarization being examined and indicates that both the amplitude and phase are in agreement.

Magnitude ratio is defined as $20 \log_{10} |\sqrt{\sigma_1}| - 20 \log_{10} |\sqrt{\sigma_2}|$. It is indicated in the following charts by “|Model|/|SBR|” or “|Model|/|MoM|” and is presented for a ± 20 dB range about 0 dB. For the magnitude ratio figures, the color white is at 0 dB and indicates a perfect match in magnitude between the waveforms being examined.

For each target case examined, a figure is provided to help visualize the real-world orientation, position, transmit angle, and receiver sweep. A table is also included which quantitatively summarizes the scattering data and difference calculations at the peak forward scatter position. Finally, polarimetric data is presented with one polarization per page, in the order VV-HV-VH-HH.

4.3 Dihedral at Original Orientation and Position

The scene visualization for this case is shown in Figure 4.1. The polarimetric scattering for a dihedral with no orientation or position change and transmitter position $(\theta_t, \phi_t) = (50^\circ, 60^\circ)$ is shown in Figures 4.2-4.5. The quantitative summary of scattering at the peak forward scatter angle is given in Table 4.1. This case is examined prior to the others in this chapter to provide the reader a baseline understanding of how the GO-PO dihedral solution compares to SBR and MoM predictions without adding the effects of changes to target orientation or position.

The following analysis focuses primarily on the dominant polarization for this dihedral orientation, co-pol scattering. It then covers the cross-pols and finishes by

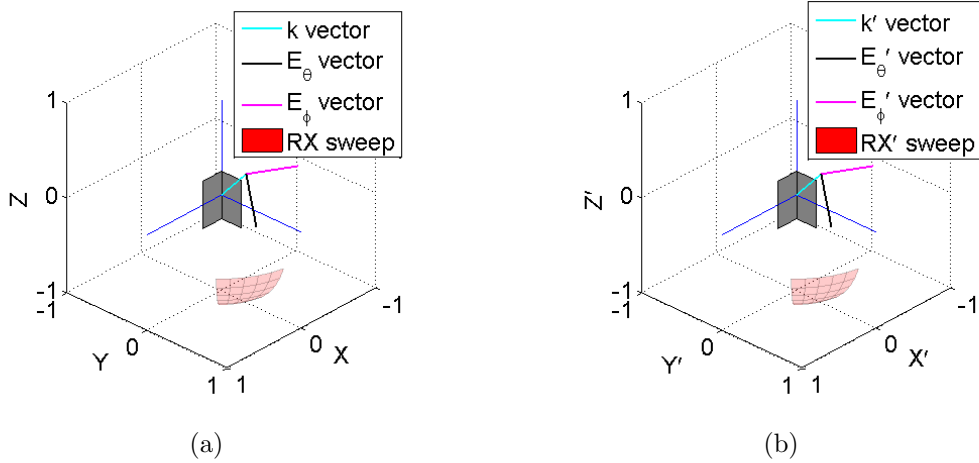


Figure 4.1. Geometry and TX/RX angles for scene with dihedral at original orientation and position, (a) global coordinate system, (b) target coordinate system. Transmit location is $(\theta_t, \phi_t) = (50^\circ, 60^\circ)$ and $(\theta'_t, \phi'_t) = (50^\circ, 60^\circ)$ in the target coordinate system. Dihedral height is 0.5m, the sides are 0.25m. Prime notation used to indicate target coordinate system.

presenting computation times for each prediction method.

As shown in Table 4.1 and Figures 4.2 and 4.5, the co-pol magnitude predicted by the model in this thesis shows excellent agreement with SBR (< 0.33 dB difference) and MoM predictions (< 0.35 dB difference) at the specular angle. For the entire $\pm 20^\circ \times \pm 20^\circ$ receiver range, the magnitude ratio between the model and SBR data is near 0 dB, and the coherent difference is < -20 dBsm, indicating that the model developed in this thesis shows excellent agreement with SBR predictions in both magnitude and phase. This is expected as SBR calculates multiple-bounce rays using geometric optics and performs the PO integral for the last surface contacted by the ray, in a similar manner to the GO-PO solution developed in [12] which this thesis is based on.

Examining the differences between MoM and both the GO-PO model and SBR predictions, one observes the co-pol response matches well in magnitude at the peak forward scatter (< 0.35 dB magnitude ratio). While the coherent difference is low

Table 4.1. Scattering amplitudes and differences at specular angle for dihedral at original orientation and position

Peak Magnitude (dBsm)	VV	HV	VH	HH
Model	18.47	$-\infty$	-10.45	18.84
SBR	18.44	$-\infty$	-9.95	18.80
MoM	18.79	-7.91	-7.94	18.98
Coherent Difference (dBsm)	VV	HV	VH	HH
Model-SBR	-28.51	$-\infty$	-34.25	-29.24
Model-MoM	-1.35	-7.91	-16.33	0.18
SBR-MoM	-1.47	-7.91	-17.28	0.28
Magnitude Ratio (dB)	VV	HV	VH	HH
Model / SBR	0.03	∞	-0.49	0.03
Model / MoM	-0.33	$-\infty$	-2.5	-0.14
SBR / MoM	-0.35	$-\infty$	-2.01	-0.18

(coherent difference is much lower than actual scattering), there is not an exact coherent match along the elevation angle which intersects the peak response ($\theta_t = 130^\circ$). This behavior is observed in the coherent difference between the model and MoM as well as SBR and MoM predictions, and is between -1 and 0.5 dBsm. By examining the co-pol phase plots in Figures 4.2k and 4.5k, one observes a slight mismatch in phase between the PO-based and more exact MoM predictions. The primary cause of this coherent difference at the forward scatter response is the GO ray calculation which assumes the double bounce interaction between the two plates is in the far field, i.e. that the double bounce electromagnetic wave is planar as it impinges on the second plate. As discussed in [8], this can be resolved by calculating the near-field reflection from the PO approximation on the first plate; however, this provides minimal increase in accuracy for a right angle dihedral with a very significant increase to computational complexity. In conclusion, the model prediction shows perfect agreement in magnitude and phase with SBR and excellent agreement in magnitude but not phase when compared to MoM for co-pol.

As expected, the model and SBR cross-pol response for this dihedral orientation is very low, HV: $-\infty$ dBsm, while VH ranges from -20 to -10 dBsm because of the off-waterline transmit elevation. Note the GO-PO prediction for VH-pol reduces to $-\infty$ dBsm when θ_t and θ_r are waterline (90°); see Appendix B, Equation (B.1). Due to HV-pol predictions of $-\infty$ dBsm, the magnitude ratio between prediction codes and the model computes to be $\pm\infty$ dB. The VH-pol data shows fairly significant magnitude ratio (2 dB) when comparing model and SBR to MoM predictions. This is because although the MoM prediction is low (< -10 dBsm), the dominant scattering mechanisms are second order effects (near-field interaction for the double-bounce and diffraction from the dihedral edges) which are not accounted for in the PO-based model and SBR predictions.

The VH magnitude and phase plots in Figures 4.4j and k show a difference between the model and SBR. This is due to differences in how the surface current integral is calculated. While SBR numerically calculates the integral, the closed-form solution developed in [12] uses L'Hopital's rule to account for singularities in the integral, see Equations (3.22-3.25). For polarizations with low scattering levels (< 0 dBsm) and at angles which approach scattering nulls, these differences produce small differences in magnitude and phase between model and SBR data.

Calculation time on Dell Precision 690TM workstations with one Quad 3.00 GHz Intel Xeon[®] processor and 32GB random access memory (RAM) for the $400(\theta_r) \times 400(\phi_r)$ dataset in this example is approximately 13.5 hours for MoM, 6 minutes for SBR, and 2.6 seconds for the model used in this thesis. Calculation time does not take into account time used for target mesh creation or modification required for the SBR and MoM methods. The model developed in this thesis does not require these additional files. Thus, the increase to computational efficiency is greater than the ratio of run times.

VV-polarization

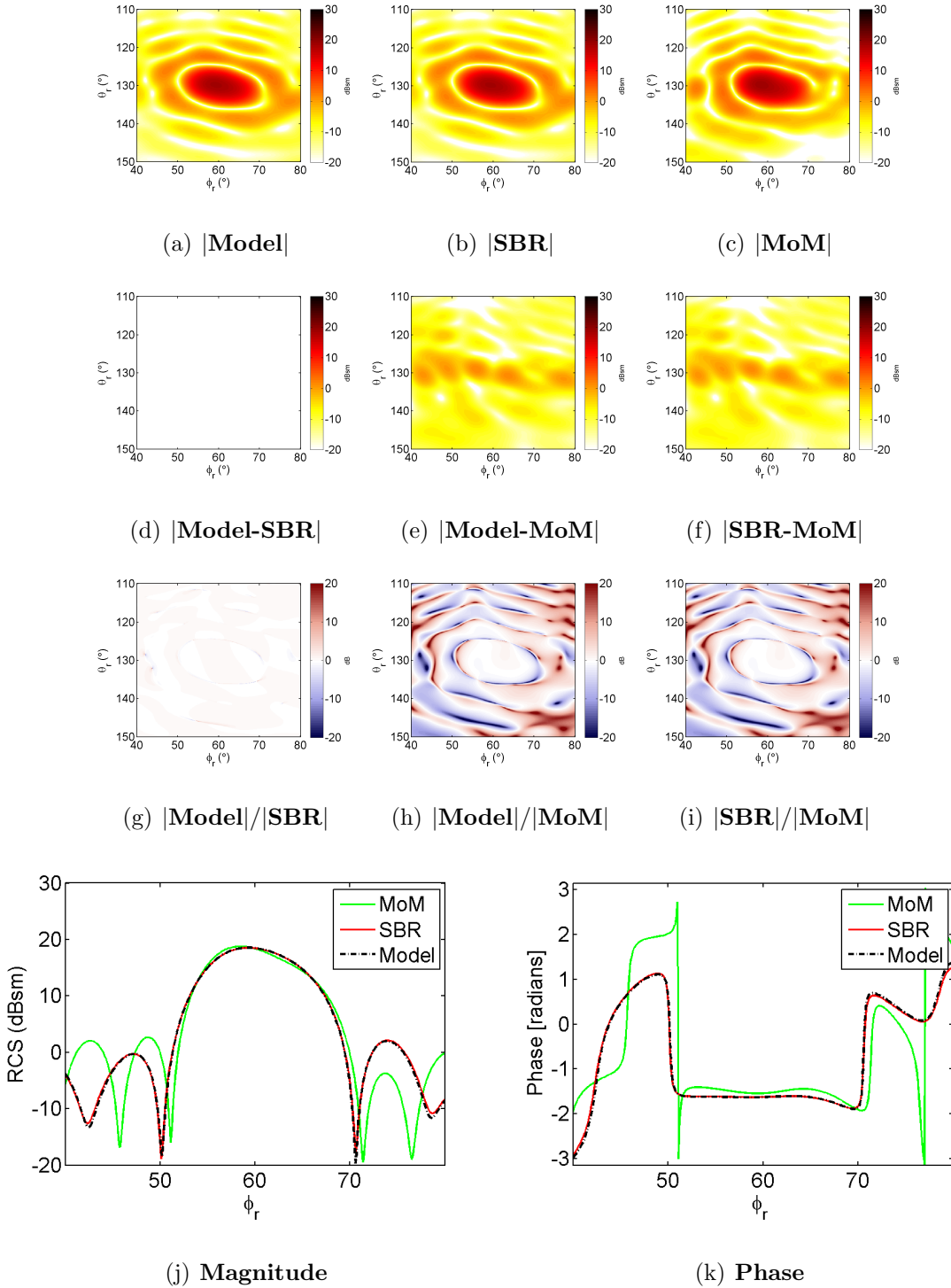


Figure 4.2. Comparison of VV-pol scattering for the dihedral at original orientation and position shown in Figure 4.1 with incident aspect $(\theta_t, \phi_t) = (50^\circ, 60^\circ)$. Figures a-c show the magnitude response for the model developed in this thesis, SBR, and MoM data respectively. Figures d-f show the coherent difference, and g-i show the magnitude ratio between these waveforms. Figures j and k show magnitude and phase for an azimuth sweep for constant elevation through the peak response, in this case $\theta_r = 130^\circ$.

HV-polarization

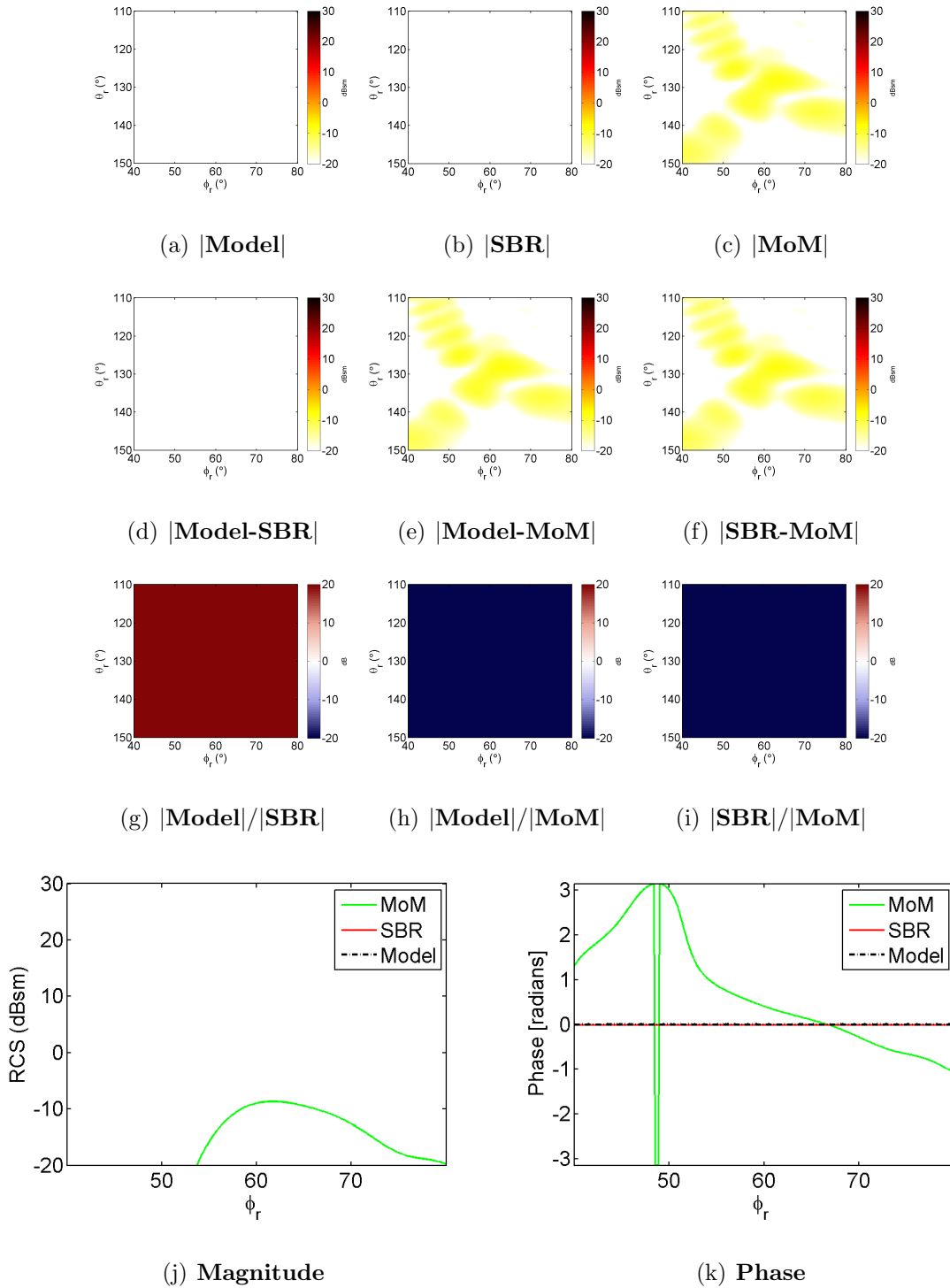


Figure 4.3. Comparison of HV-pol scattering for the dihedral at original orientation and position shown in Figure 4.1 with incident aspect $(\theta_t, \phi_t) = (50^\circ, 60^\circ)$. Figures a-c show the magnitude response for the model developed in this thesis, SBR, and MoM data respectively. Figures d-f show the coherent difference, and g-i show the magnitude ratio between these waveforms. Figures j and k show magnitude and phase for an azimuth sweep for constant elevation through the peak response, in this case $\theta_r = 130^\circ$.

VH-polarization

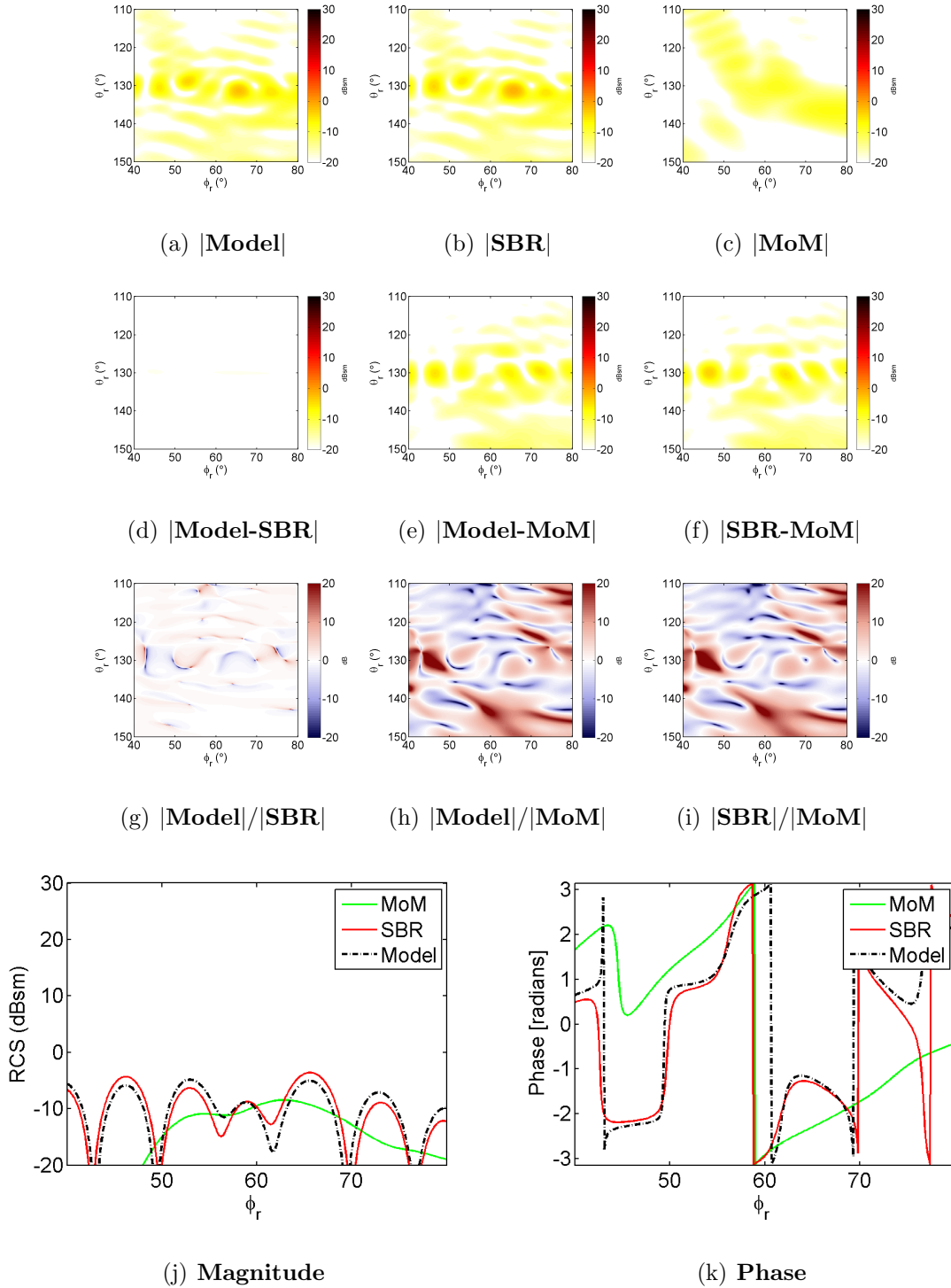


Figure 4.4. Comparison of VH-pol scattering for the dihedral at original orientation and position shown in Figure 4.1 with incident aspect $(\theta_t, \phi_t) = (50^\circ, 60^\circ)$. Figures a-c show the magnitude response for the model developed in this thesis, SBR, and MoM data respectively. Figures d-f show the coherent difference, and g-i show the magnitude ratio between these waveforms. Figures j and k show magnitude and phase for an azimuth sweep for constant elevation through the peak response, in this case $\theta_r = 130^\circ$.

HH-polarization

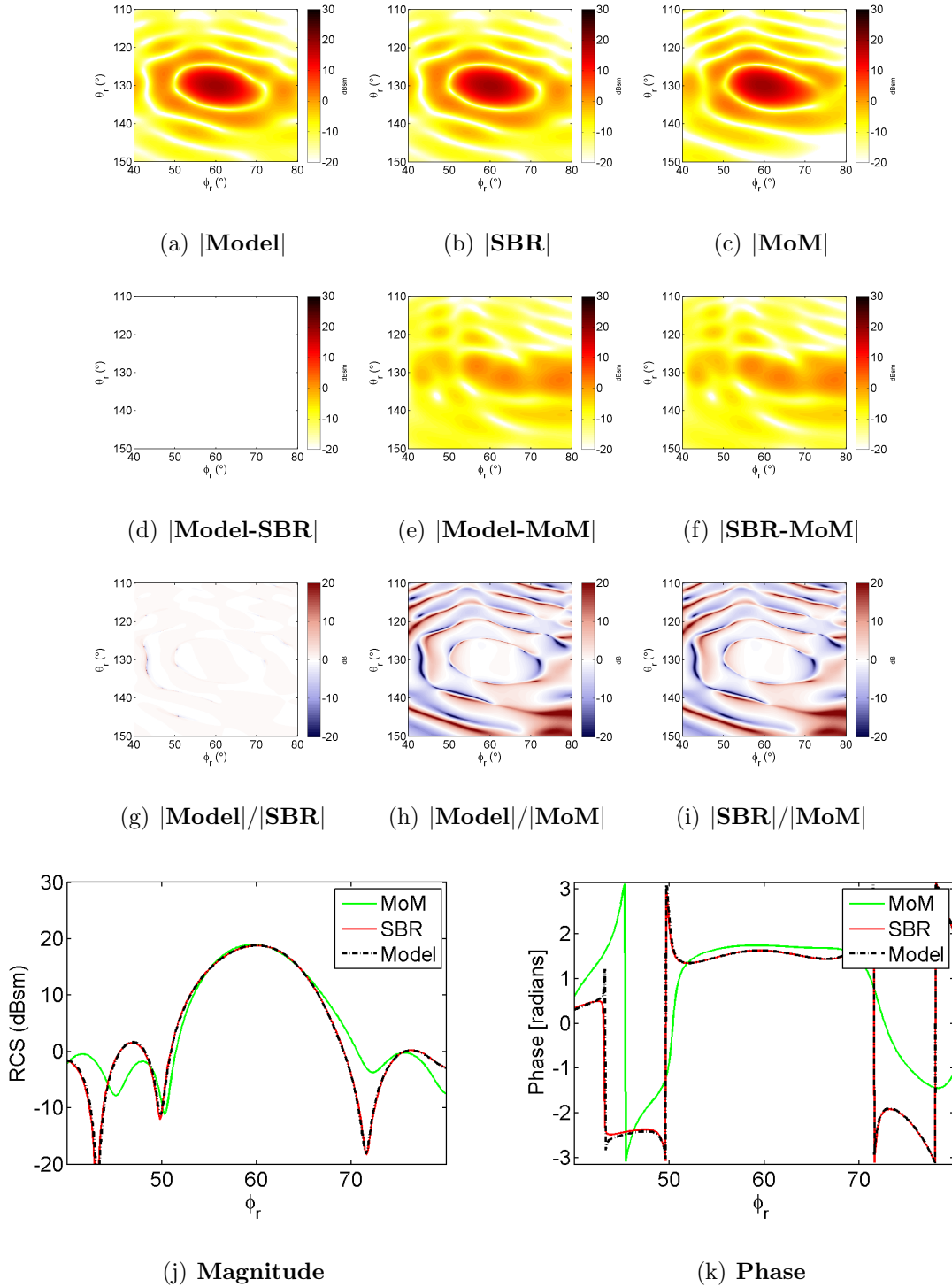


Figure 4.5. Comparison of HH-pol scattering for the dihedral at original orientation and position shown in Figure 4.1 with incident aspect $(\theta_t, \phi_t) = (50^\circ, 60^\circ)$. Figures a-c show the magnitude response for the model developed in this thesis, SBR, and MoM data respectively. Figures d-f show the coherent difference, and g-i show the magnitude ratio between these waveforms. Figures j and k show magnitude and phase for an azimuth sweep for constant elevation through the peak response, in this case $\theta_r = 130^\circ$.

4.4 Arbitrary Orientation and Position Model Validation

This section will provide two types of data comparisons. First, a case is examined where the model developed in this thesis is used to predict the scattering from a dihedral with changes to all six orientation and position parameters - roll, pitch, yaw, T_x , T_y , and T_z . As in Section 4.3, comparisons will be performed against SBR and MoM predictions. Second, the model developed in this thesis is compared to the 3D parametric model developed in [13] and measurements in the AFIT RCS range.

4.4.1 Dihedral with Roll, Pitch, Yaw Rotation and Translation from Origin.

The scene visualization for this case is provided in Figure 4.6. The polarimetric scattering for a dihedral at roll 60° , pitch 45° , yaw 10° and translated $X=0.2\text{m}$, $Y=-0.3\text{m}$, $Z=0.4\text{m}$ from the origin with transmitter position $(\theta_t, \phi_t) = (90^\circ, -10^\circ)$ is shown in Figures 4.8-4.11. The quantitative scattering summary at the peak forward scatter angle is given in Table 4.2. This case is examined to showcase the ability for the model in this thesis to account for any combination of arbitrary orientation and position for the dihedral. A similar case for the flat plate at arbitrary orientation and position is given in Appendix Section 1.1.2.

Positioning the dihedral at this orientation produces significant scattering magnitude at the forward mainlobe for all polarizations (co-pols: ≈ 17 dBsm, cross-pols: ≈ 14 dBsm). An explanation of this depolarizing behavior and how it relates to dihedral orientation is provided in Section 4.5. Because all four polarizations are dominated by the mainlobe double-bounce response (not diffraction and near-field double-bounce effects), the model shows excellent agreement with SBR and MoM predictions for this dihedral orientation. As shown in Table 4.2, the coherent difference between model and SBR is < -38 dBsm for all polarizations, and the magnitude

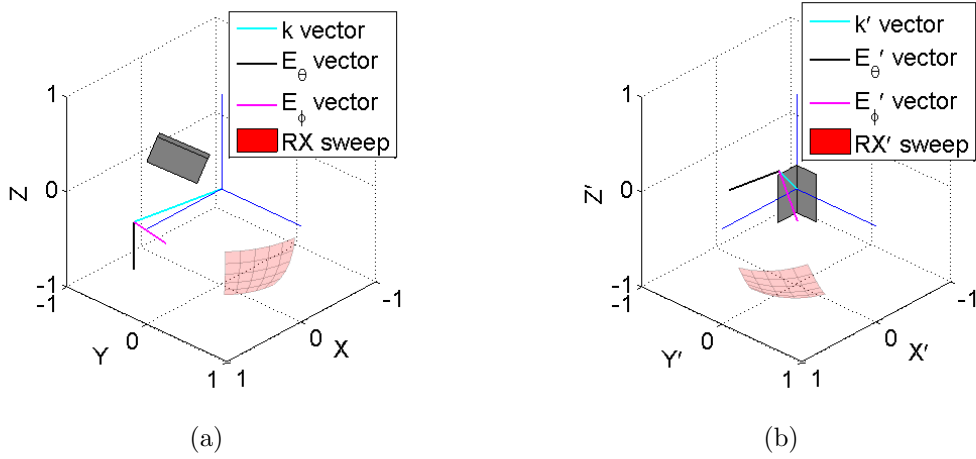


Figure 4.6. Geometry and TX/RX angles for scene with rotated and translated dihedral, (a) global coordinate system, (b) target coordinate system. Dihedral is at roll 60° , pitch 45° , yaw 10° and translated $X=0.2\text{m}$, $Y=-0.3\text{m}$, $Z=0.4\text{m}$ from the origin. Transmit location is $(\theta_t, \phi_t) = (90^\circ, -10^\circ)$ and $(\theta'_t, \phi'_t) = (51.07^\circ, 31.33^\circ)$ in the target coordinate system. Dihedral height is 0.5m , the sides are 0.25m . Prime notation used to indicate target coordinate system.

ratio is also very low (< 0.02 dB). This indicates the model in this thesis is capable of accurately accounting for the effects of orientation and position change.

Comparing the model and MoM predictions at the forward scatter angle, one observes very small magnitude ratio (< 0.7 dB) for all polarizations except HH-pol which is slightly higher at 1.33 dB. The coherent difference at the forward scatter angle is 1.2 dBsm for VV-pol, -2.3 dBsm for HV-pol, 0.2 dBsm for VH-pol, and 4.5 dBsm for HH-pol; these values are approximately 16 dB less than the predicted scattering magnitude for each polarization. As in the the case of the dihedral at original orientation and position, there is a range of relatively high coherent difference between the PO-based and more exact MoM predictions, due to the planar wave assumption used to calculate the double bounce and lack of diffraction terms for the model in this thesis. However, the overall low level of coherent difference is not increased due to the changes to dihedral orientation and position. Example coherent difference figures which show the effects of incorrect phase terms to account

Table 4.2. Scattering amplitudes and differences at specular angle for dihedral with roll, pitch, yaw rotation and translation from origin

Peak Magnitude (dBsm)	VV	HV	VH	HH
Model	17.41	14.4	13.93	17.71
SBR	17.41	14.38	13.93	17.71
MoM	17.81	15.1	14.4	19.05
Coherent Difference (dBsm)	VV	HV	VH	HH
Model-SBR	-51.85	-38.12	-54.52	-41.74
Model-MoM	1.173	-2.33	0.20	4.48
SBR-MoM	1.17	-2.25	0.20	4.45
Magnitude Ratio (dB)	VV	HV	VH	HH
Model / SBR	0.00	0.02	0.00	-0.01
Model / MoM	-0.40	-0.70	-0.47	-1.34
SBR / MoM	-0.40	-0.71	-0.47	-1.33

for position offset are given in Figure 4.7. Clearly the coherent difference plots in Figures 4.8-4.11 do not show the effects of incorrect phase translation terms.

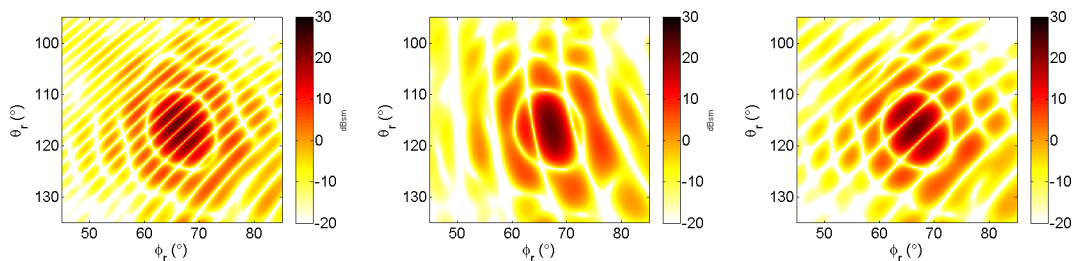


Figure 4.7. Example coherent difference plots where incorrect phase correction is applied to account for target position. Each figure is the VV-polarization coherent difference between a model which uses incorrect phase terms and the SBR prediction for the case examined in this section. Similar behavior is not observed in the coherent difference plots in Figures 4.8-4.11, indicating that the model in this thesis accurately accounts for the effects of arbitrary target position.

Calculation time on Dell Precision 690TM workstations with one Quad 3.00 GHz Intel Xeon® processor and 32GB RAM for the $400(\theta_r) \times 400(\phi_r)$ dataset in this example is approximately 13.74 hours for MoM, 7 minutes for SBR, and 2.7 seconds for the model developed in this thesis. Calculation time does not take into account

time used for target mesh creation or modification required for the SBR and MoM methods. The model developed in this thesis does not require these additional files. Thus, the increase to computational efficiency is greater than the ratio of run times.

VV-polarization

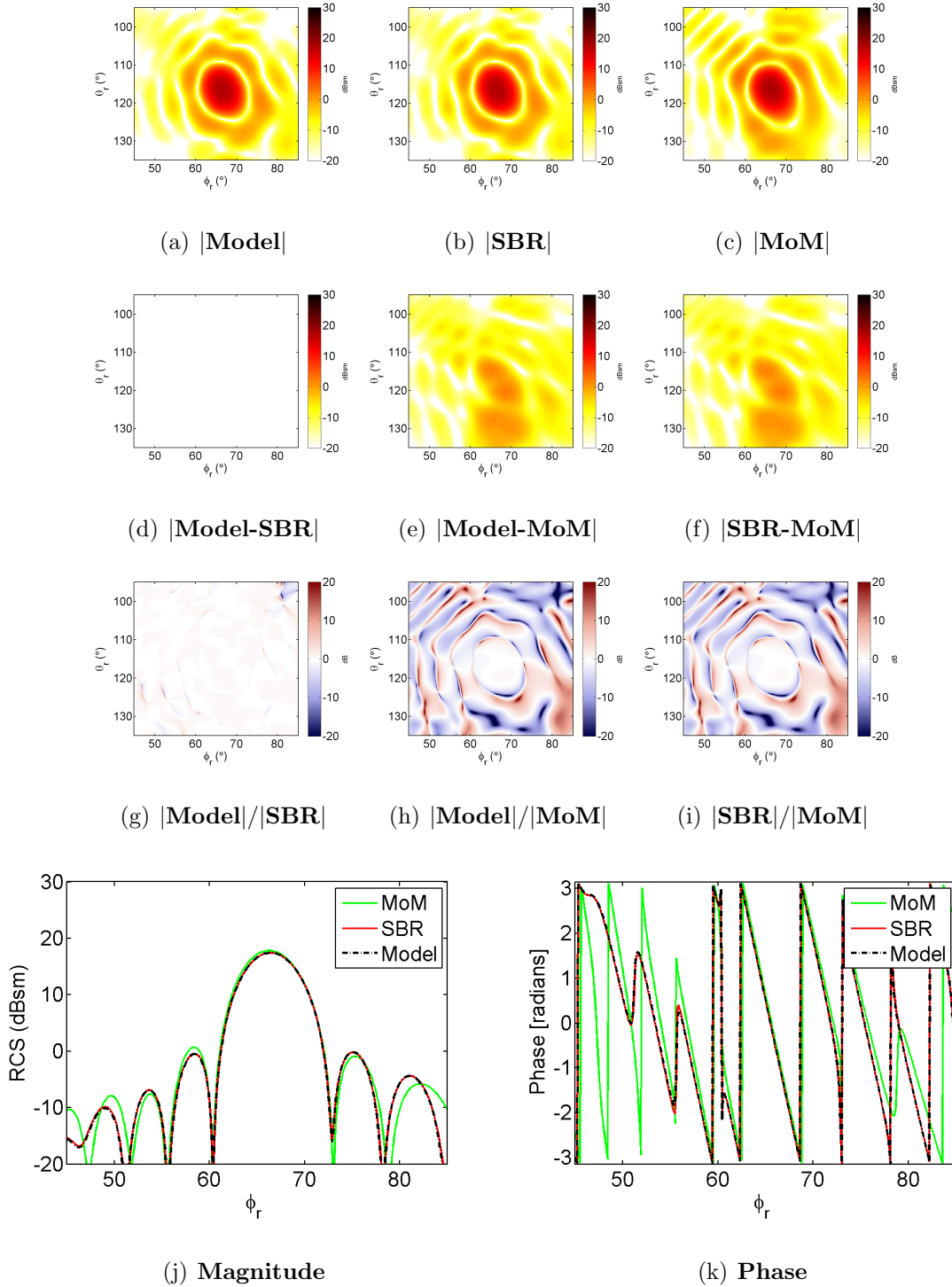


Figure 4.8. Comparison of VV-pol scattering for the rotated and translated dihedral shown in Figure 4.6 with incident aspect $(\theta_t, \phi_t) = (90^\circ, -10^\circ)$. Figures a-c show the magnitude response for the model developed in this thesis, SBR, and MoM data respectively. Figures d-f show the coherent difference, and g-i show the magnitude ratio between these waveforms. Figures j and k show magnitude and phase for an azimuth sweep for constant elevation through the peak response, in this case $\theta_r = 116^\circ$.

HV-polarization

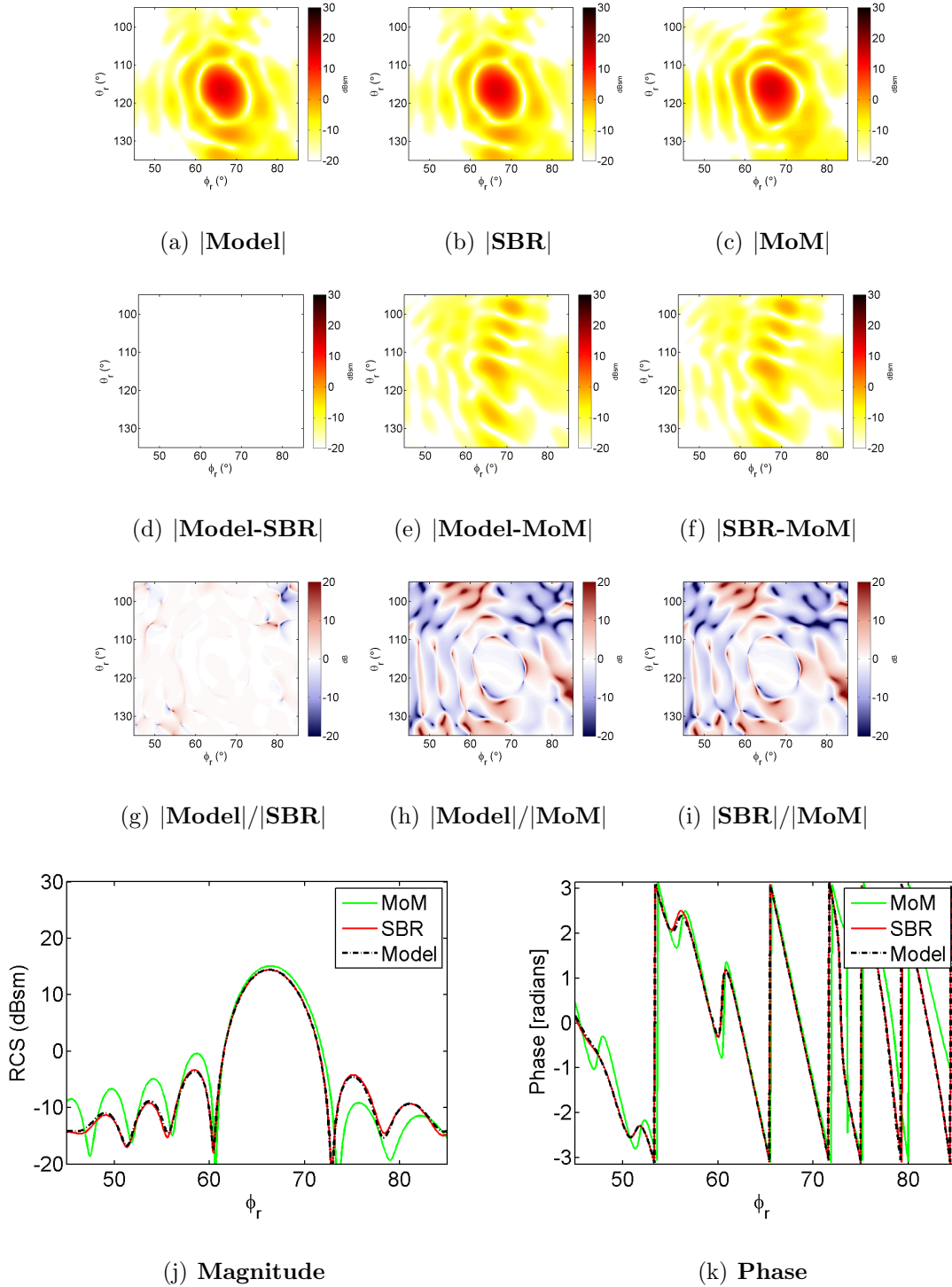


Figure 4.9. Comparison of HV-pol scattering for the rotated and translated dihedral shown in Figure 4.6 with incident aspect $(\theta_t, \phi_t) = (90^\circ, -10^\circ)$. Figures a-c show the magnitude response for the model developed in this thesis, SBR, and MoM data respectively. Figures d-f show the coherent difference, and g-i show the magnitude ratio between these waveforms. Figures j and k show magnitude and phase for an azimuth sweep for constant elevation through the peak response, in this case $\theta_r = 116^\circ$.

VH-polarization

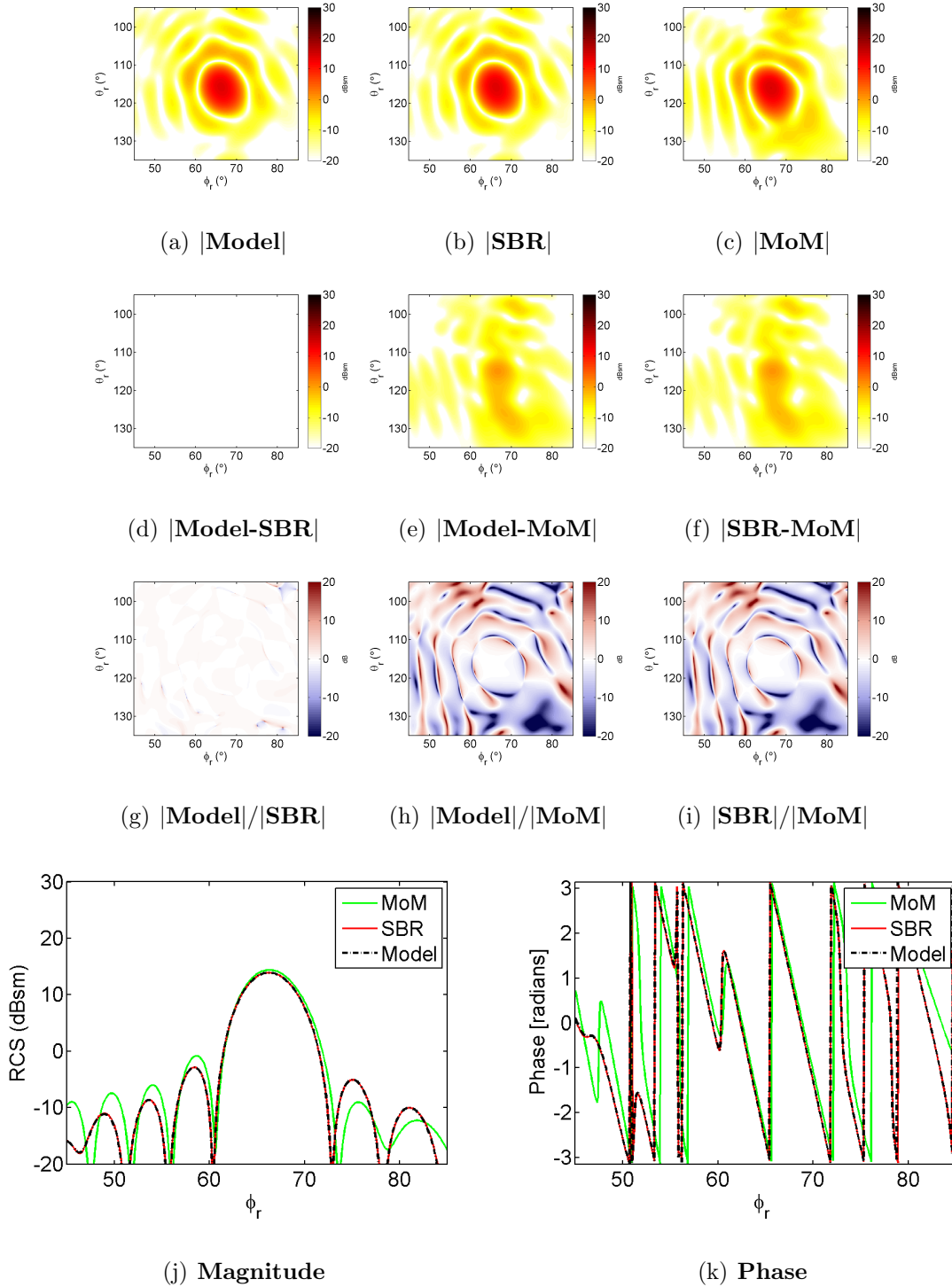


Figure 4.10. Comparison of VH-pol scattering for the rotated and translated dihedral shown in Figure 4.6 with incident aspect $(\theta_t, \phi_t) = (90^\circ, -10^\circ)$. Figures a-c show the magnitude response for the model developed in this thesis, SBR, and MoM data respectively. Figures d-f show the coherent difference, and g-i show the magnitude ratio between these waveforms. Figures j and k show magnitude and phase for an azimuth sweep for constant elevation through the peak response, in this case $\theta_r = 116^\circ$.

HH-polarization

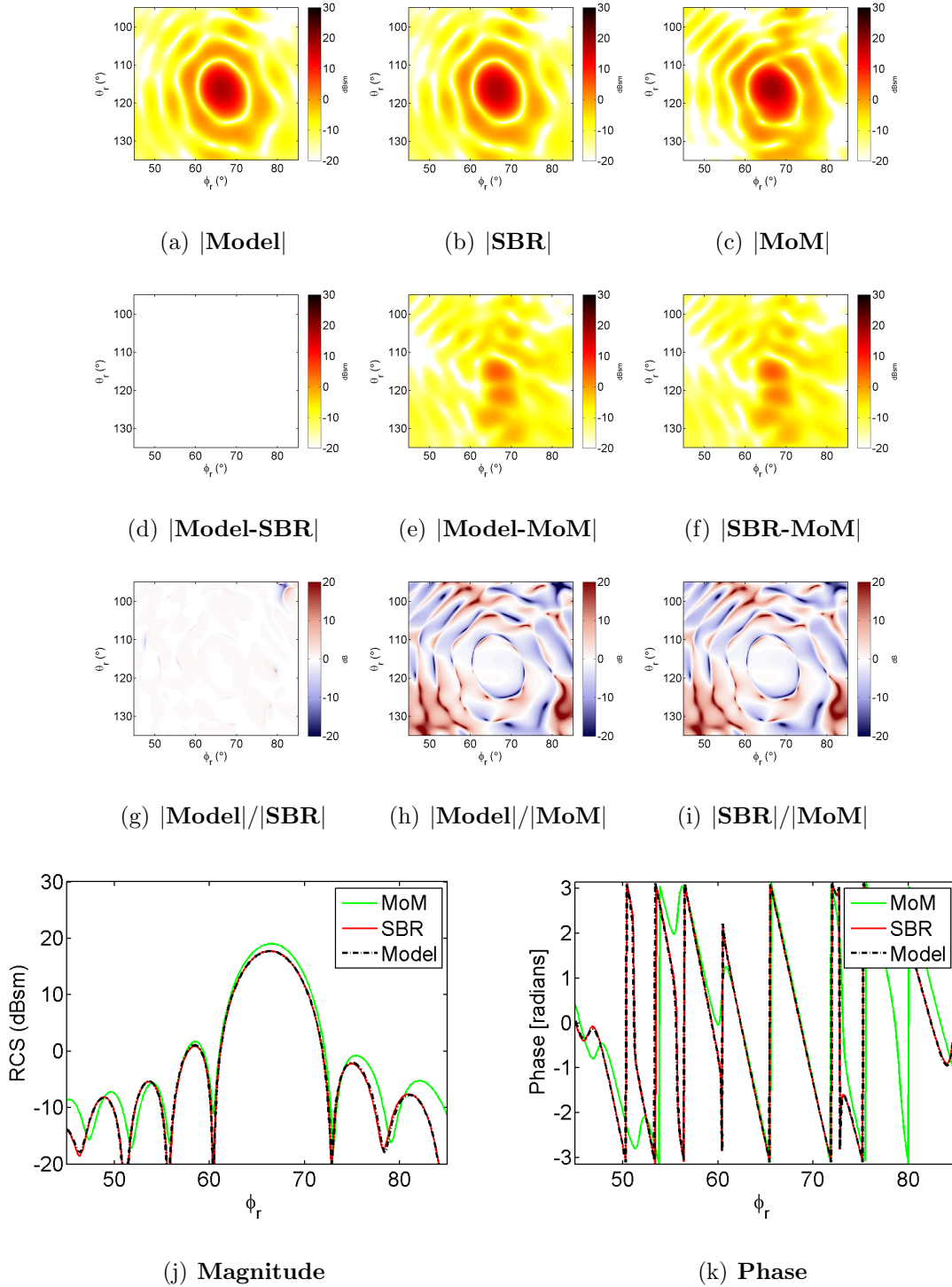


Figure 4.11. Comparison of HH-pol scattering for the rotated and translated dihedral shown in Figure 4.6 with incident aspect $(\theta_t, \phi_t) = (90^\circ, -10^\circ)$. Figures a-c show the magnitude response for the model developed in this thesis, SBR, and MoM data respectively. Figures d-f show the coherent difference, and g-i show the magnitude ratio between these waveforms. Figures j and k show magnitude and phase for an azimuth sweep for constant elevation through the peak response, in this case $\theta_r = 116^\circ$.

4.4.2 Comparison to Measured RCS Data.

In this section, the model in this thesis is compared to RCS data collected in the AFIT RCS range. Range information and a description of the two measurement scenarios are given in Section 2.3.5. The test matrix is summarized in Table 4.3. Also, the parametric model (PM) described in Section 2.2.2 is used as a prediction method in this section in order to observe any differences in accuracy when compared to the model in this thesis. Note that this section contains data originally presented in [23].

Table 4.3. Measurement matrix for AFIT RCS range

Scenario	Dihedral Orientation	ϕ_t	ϕ_r	$\Delta\phi_r$
S1	roll: 90°, pitch: 45°	-30°	[-30°, 70°]	0.5°
S2	roll: 90°, pitch: 20°	-10°	[-10°, 50°]	0.5°

There are a few changes to how data is presented compared to the other sections in this chapter. Because the bistatic range measurements are collected for an azimuth sweep at waterline, data is not presented for an $\theta_r \times \phi_r$ range. Also, only co-pol measurement data is available, therefore cross-pols are not analyzed in this section. The measured data is calibrated for magnitude but not phase, consequently coherent difference plots are not provided. Calibration information is provided in Section 2.3.5.2. Because the measured data is manually aligned in ϕ_r , quantitative data is calculated as the peak scattering for each waveform, not at the peak scattering for a specific receiver position. Finally, to present the data more clearly, the measurement comparisons in this section are calculated as the absolute value of the magnitude ratio between the measured data and prediction waveforms, $\left| 20 \log_{10} \frac{|\text{prediction}|}{|\text{measured}|} \right|$. Values nearest to 0 dB indicate excellent agreement in magnitude.

4.4.2.1 Measurement Scenario 1.

The orientation for this scene is shown in Figure 4.12. The RCS and magnitude ratio plots for scenario 1 are given in Figure 4.13, while the quantitative waveform summary is provided in Table 4.4.

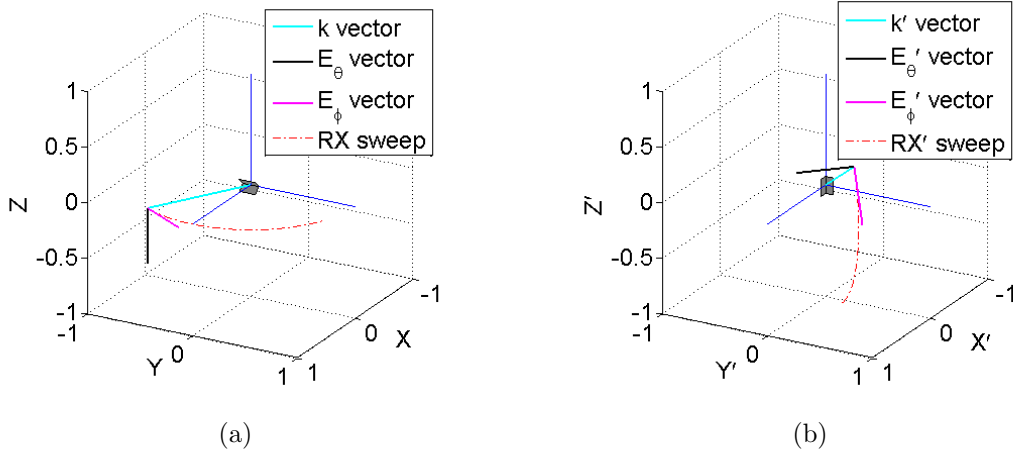


Figure 4.12. Geometry and TX/RX angles for measurement scenario 1, (a) global coordinate system, (b) target coordinate system. Dihedral is at roll 90° , pitch 45° . Transmit location is $(\theta_t, \phi_t) = (90^\circ, -30^\circ)$ and $(\theta'_t, \phi'_t) = (60^\circ, 45^\circ)$ in the target coordinate system. Dihedral height is $6''$, the sides are $3''$. Prime notation used to indicate target coordinate system.

Table 4.4. Quantitative summary for measurement scenario 1

Prediction Method	Peak (dBsm)	Magnitude Ratio at Peak (dB)	3dB Width (degrees)	Computation Time
	vv-pol, hh-pol	vv-pol, hh-pol	vv-pol, hh-pol	
Measure	0.78, 1.87	-, -	$12.6^\circ, 11.25^\circ$	Order(hours)
Model	2.90, 2.17	-2.12, -0.30	$13.7^\circ, 14.2^\circ$	Order(10^{-2} sec.)
PM	4.52, 4.52	-3.74, -2.65	$10.9^\circ, 10.9^\circ$	Order(10^{-2} sec.)
MoM	1.90, 0.65	-1.12, 1.22	$13.6^\circ, 14.6^\circ$	Order(minutes)
SBR	2.93, 2.21	-2.15, -0.34	$13.6^\circ, 14.2^\circ$	Order(seconds)

Visual inspection of Figure 4.13 confirms that the model, SBR, and MoM waveforms closely follow the measured data amplitude and mainlobe width near the peak

forward scatter response. The PM prediction over-estimates the peak magnitude and has a narrower 3dB width compared to the measured data and other prediction methods. As expected, the simple PM prediction begins to diverge from the measured data outside of the first null and is significantly different for $\phi_r < 20^\circ$ and $\phi_r > 40^\circ$. The not-insignificant (1.2 dB) magnitude ratio between the peak MoM and measured data is likely due to differences between measurement data collection and simulation data collection. For example, the styrofoam block used to tilt the dihedral forward in the RCS range is most likely not exactly 45° . Also, the surface of the dihedral is likely marred by physical inconsistencies which are the probable cause of the repeatable disjointed behavior on the left side of the measured data mainlobe.

There is a small measurement inaccuracy in the mainlobe located near 32° in VV-polarization and 35° in HH-polarization. This is most apparent in the magnitude difference plots in Figure 4.13, which show an additional 1.2 dB magnitude difference at these angles. Global range plots of the original, unshifted measurement data are provided in Figure 4.14. These plots show that this measurement inaccuracy exists over every frequency (i.e. along the entire range) for this specific receiver angle. Most likely, this indicates that the mobile bistatic receiver arm was not completely settled for this specific angle. However, this measurement collection dataset is the best overall quality of the many data collection attempts for this orientation. Other attempts suffered from significant range clutter and other measurement issues. The global range plots show that range clutter is not a significant factor for this specific measurement inaccuracy.

The computation times for this case are not as varied between the prediction methods as for the other cases examined in this chapter. There are two reasons for this. First, the size of the dihedral is smaller, leading to a smaller amount of unknown elements in the MoM calculation. Also, this case involves a significantly lower amount

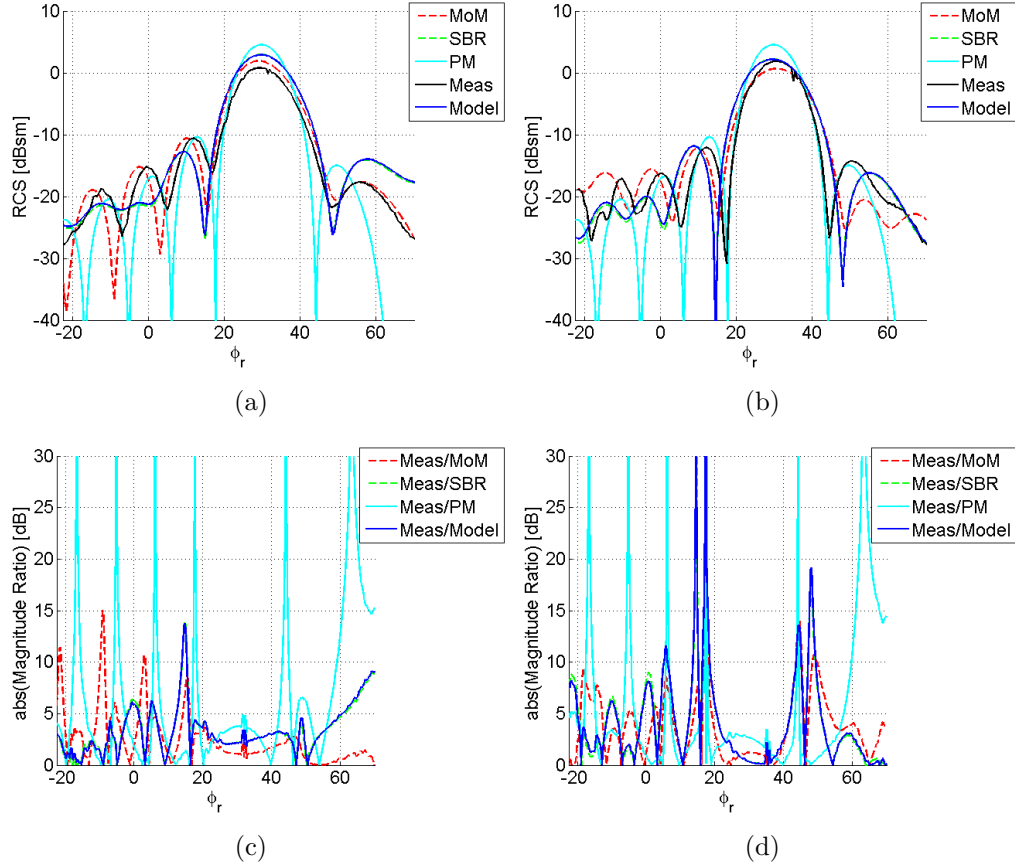


Figure 4.13. Comparison of measured vs. predicted scattering for measurement scenario 1 (a,b = 3", L = 6", f=10GHz, roll 90°, pitch 45°, $(\theta_t, \phi_t) = 90^\circ, -30^\circ$, and azimuth receiver sweep at $\theta_r = 90^\circ$). (a) VV, (b) HH, (c) magnitude ratio for VV, (d) magnitude ratio for HH. ‘MoM’ indicates method of moments prediction, ‘SBR’ indicates shooting and bouncing ray prediction, ‘PM’ indicates parametric model developed in [13] for ATR, ‘Meas.’ indicates measured data collected in AFIT RCS range, and ‘Model’ indicates the method developed in this thesis.

of receiver data points (201) than the 3D cases in this chapter ($401 \times 401 = 160801$). However, as shown in Table 4.4, there is still an appreciable computational savings for using both the model in this thesis or PM compared to MoM predictions. This measurement comparison shows that the model in this thesis is as computationally fast as the PM model, is as accurate as the SBR prediction, and is more accurate than the PM model.

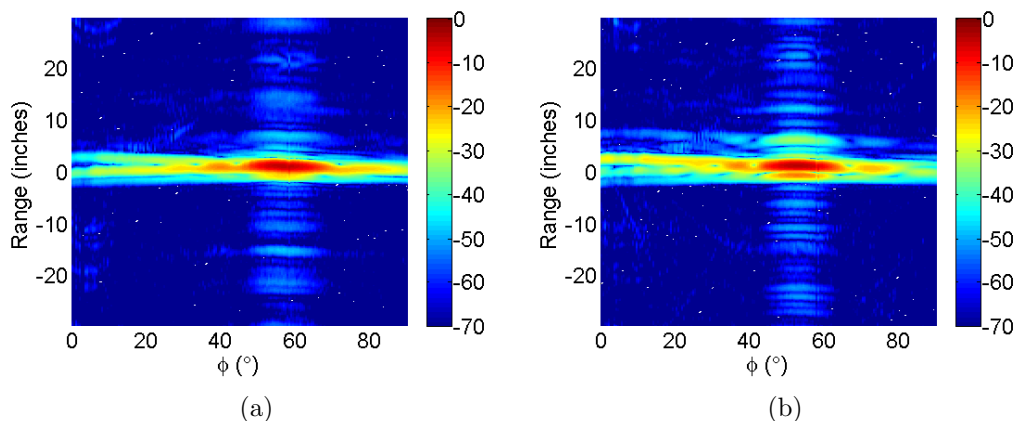


Figure 4.14. Global range for Scenario 1 measured data, (a) VV, (b) HH. Global range plots are used for insight into the scattering mechanisms behind the collected RCS data, and to examine possible range clutter. These global range plots show a slight inaccuracy at 58° for all range positions, indicating that most likely the mobile bistatic receiver arm was not settled for this measurement. This results in the small measured data 'blip' to the right of the peak mainlobe in Figure 4.13.

4.4.2.2 Measurement Scenario 2.

The orientation for this scene is shown in Figure 4.15. The RCS and magnitude ratio for scenario 2 are shown in Figure 4.16, and the quantitative summary is given in Table 4.5.

Table 4.5. Quantitative summary for measurement scenario 2

Prediction Method	Peak (dBsm)	Magnitude Ratio at Peak (dB)	3dB Width (degrees)	Computation Time
	vv-pol, hh-pol	vv-pol, hh-pol	vv-pol, hh-pol	
Measure	0.20, 0.24	-, -	$10.5^\circ, 11.4^\circ$	Order(hours)
Model	-2.27, 0.22	2.47, 0.02	$10.6^\circ, 10.5^\circ$	Order(10^{-2} sec.)
PM	-0.68, -0.68	0.87, 0.92	$10.1^\circ, 10.1^\circ$	Order(10^{-2} sec.)
MoM	-3.25, 1.55	3.45, -1.31	$10.43^\circ, 10.8^\circ$	Order(minutes)
SBR	-2.04, 0.39	2.24, -0.15	$10.6^\circ, 10.5^\circ$	Order(seconds)

This measurement scenario follows the previous example in that the model, SBR, and MoM waveforms closely match the measured data amplitude and mainlobe width

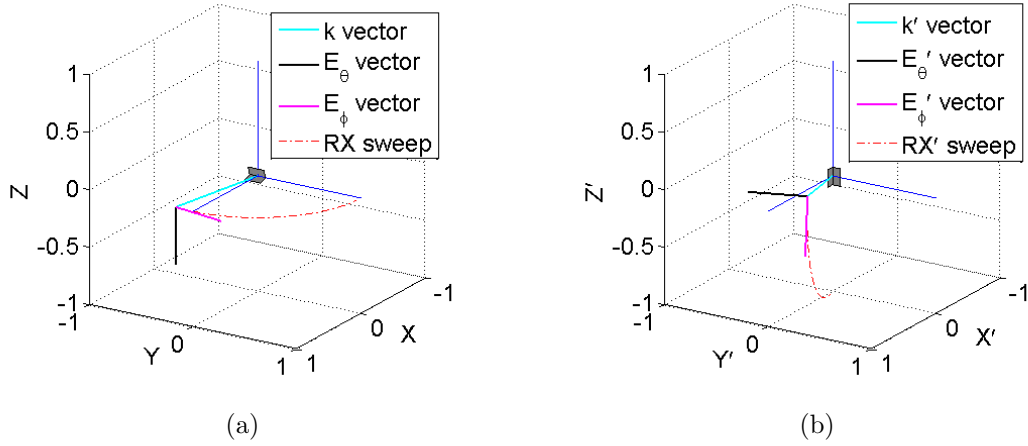


Figure 4.15. Geometry and TX/RX angles for measurement scenario 2, (a) global coordinate system, (b) target coordinate system. Dihedral is at roll 90° , pitch 20° . Transmit location is $(\theta_t, \phi_t) = (90^\circ, -10^\circ)$ and $(\theta'_t, \phi'_t) = (80^\circ, 20^\circ)$ in the target coordinate system. Dihedral height is $6''$, the sides are $3''$. Prime notation used to indicate target coordinate system.

near the peak forward scatter response. Overall, the magnitude ratio between all four of the prediction methods and the measured data is smaller for this scenario. Also of note is that changing the dihedral pitch and TX position causes the peak RCS magnitude for each of the prediction methods to be lower (VV-pol: ≈ -5 dB, HH-pol: ≈ -3 dB) for scenario 2 than scenario 1. However, the measured data does not follow this behavior (VV-pol: $+0.1$ dB, HH-pol: -1.7 dB). Again, this is most likely due to inaccuracies in precisely orienting the dihedral in the AFIT RCS range. In this scenario, the model in this thesis is able to accurately account for scattering at arbitrary dihedral orientation.

The global range plots in Figure 4.17 show 'jumps' in the scattering data at 4° and 8° to 12° . This is most likely due to undesired interactions between the bistatic receiver arm and the transmitter at these near-monostatic angles. This results in the slight measured data inaccuracy on the left side of the mainlobe to the null near -2° in Figure 4.16

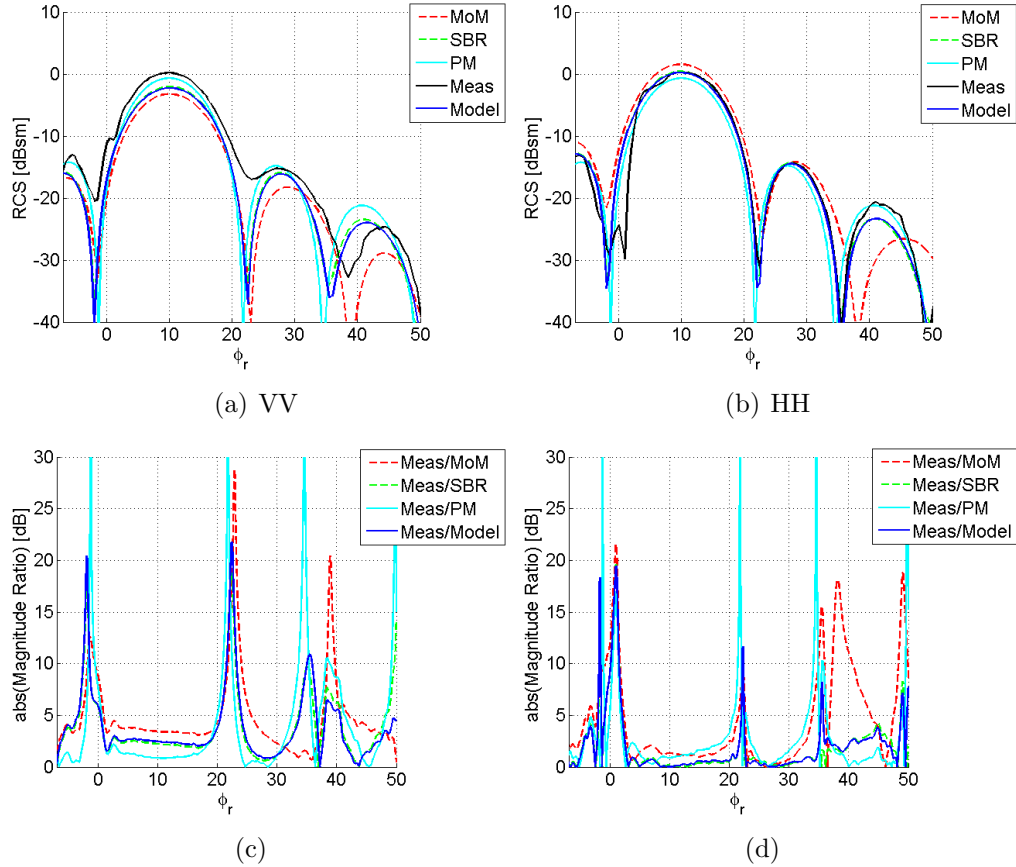


Figure 4.16. Comparison of measured vs. predicted scattering for measurement scenario 2 ($a, b = 3''$, $L = 6''$, $f = 10\text{GHz}$, roll 90° , pitch 20° , $(\theta_t, \phi_t) = 90^\circ, -10^\circ$, and azimuth receiver sweep at $\theta_r = 90^\circ$). (a) VV, (b) HH, (c) magnitude ratio for VV, (d) magnitude ratio for HH. ‘MoM’ indicates method of moments prediction, ‘SBR’ indicates shooting and bouncing ray prediction, ‘PM’ indicates parametric model developed in [13] for ATR, ‘Meas.’ indicates measured data collected in AFIT RCS range, and ‘Model’ indicates the method developed in this thesis.

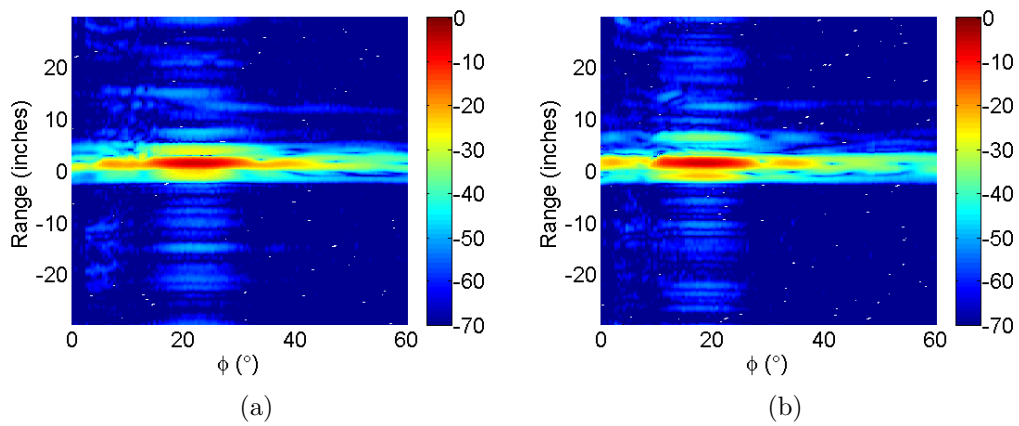


Figure 4.17. Global range for Scenario 2 measured data, (a) VV, (b) HH. Global range plots are used for insight into the scattering mechanisms behind the collected RCS data, and to examine possible range clutter. These global range plots show a slight inaccuracy at 4° and 8° to 12° . This is most likely due to undesired interactions between the bistatic receiver arm and the transmitter at these near-monostatic angles. This results in the slight measured data inaccuracy on the left side of the mainlobe in Figure 4.16.

4.5 Additional Dihedral Validation

This section will examine two interesting dihedral orientation cases. First, the dihedral at roll angle 45° will be examined, followed by a dihedral at roll angle 22.5° .

An important property of PEC dihedrals is that they act to depolarize the reflected field from the incident field. This effect is due to the reversal of the tangential surface component of the electric field at reflection [15] as shown in Figure 4.18. Because the tangential component of the electric field is essentially zero for a PEC surface, the sum of the tangential components of the incident and scattered electric fields at the surface must be zero ($\hat{n} \times \vec{E} = 0$ where $\vec{E} = \vec{E}_i + \vec{E}_s$).

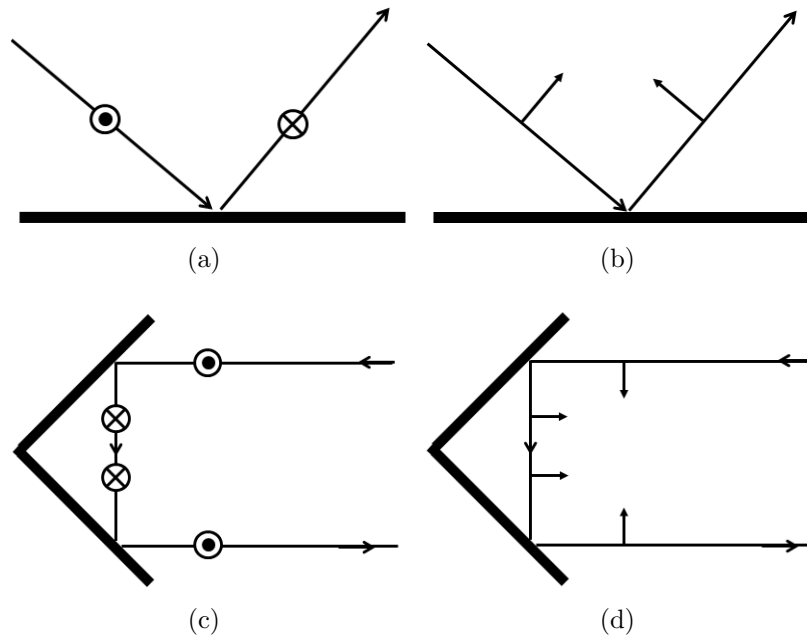


Figure 4.18. Polarization effects for PEC plate and dihedral. (a) polarization perpendicular to plane of incidence, (b) polarization parallel to plane of incidence, (c) polarization parallel to dihedral axis, (d) polarization perpendicular to dihedral axis. For a PEC obstacle, the tangential surface component of the incident electric field vector is reversed in the reflected electric field vector. When the incident electric field is perpendicular to the axis of the dihedral (d), the reflected polarization is reversed. When it is parallel to the dihedral axis (c), the reflected polarization is the same as the incident polarization.

It is shown in [15] that for the monostatic case the polarization of the reflected

wave varies with the polarization angle ψ measured with respect to the dihedral axis. If the incident polarization is rotated away from the dihedral axis by ψ , the reflected polarization is rotated by this same angle, but in the opposite direction. The same is true for the bistatic 3D case. The bistatic polarization factor P is found as follows. For dihedral rotation ζ_i about the transmitter LOS, the incident and scattered polarization is expressed as:

$$\begin{aligned}
\hat{e}_{\parallel}^i &= \hat{y} \cos \zeta_i + \hat{z} \sin \zeta_i \\
\hat{e}_{\parallel}^s &= -\hat{y} \cos \zeta_i + \hat{z} \sin \zeta_i \\
\hat{e}_{\perp}^i &= -\hat{y} \sin \zeta_i + \hat{z} \cos \zeta_i \\
\hat{e}_{\perp}^s &= \hat{y} \sin \zeta_i + \hat{z} \cos \zeta_i
\end{aligned} \tag{4.1}$$

where superscripts i and s indicate incident and scattered polarizations, subscripts \parallel and \perp indicate the parallel and perpendicular components of the incident polarization as seen from the transmit LOS, \hat{y} and \hat{z} are real-world coordinates where \hat{x} is pointed in the direction of the transmitter, and ζ_i indicates polarization rotation about the transmitter LOS and is defined in [13].

The intensity of the received field is proportional to the dot product $\hat{e}_r \cdot \hat{e}_s$, where \hat{e}_r is aligned with the receiver polarization. The unit vector \hat{e}_r in the bistatic case is:

$$\begin{aligned}
\hat{e}_{\parallel, \text{co-pol}}^r &= \hat{y} \cos \zeta_r + \hat{z} \sin \zeta_r \\
\hat{e}_{\parallel, \text{cross-pol}}^r &= -\hat{y} \sin \zeta_r + \hat{z} \cos \zeta_r \\
\hat{e}_{\perp, \text{co-pol}}^r &= -\hat{y} \sin \zeta_r + \hat{z} \cos \zeta_r \\
\hat{e}_{\perp, \text{cross-pol}}^r &= \hat{y} \cos \zeta_r + \hat{z} \sin \zeta_r
\end{aligned} \tag{4.2}$$

where ζ_r indicates dihedral rotation about the receiver LOS and is defined in [13].

Therefore, the bistatic polarization factor P for the dihedral at arbitrary orienta-

tion is:

$$\begin{aligned}
P = \begin{bmatrix} P_{VV} & P_{HV} \\ P_{VH} & P_{HH} \end{bmatrix} &= \begin{bmatrix} \hat{e}_{\parallel, \text{co-pol}}^r \cdot \hat{e}_{\parallel}^s & \hat{e}_{\parallel, \text{cross-pol}}^r \cdot \hat{e}_{\parallel}^s \\ \hat{e}_{\perp, \text{cross-pol}}^r \cdot \hat{e}_{\perp}^s & \hat{e}_{\perp, \text{co-pol}}^r \cdot \hat{e}_{\perp}^s \end{bmatrix} \\
&= \begin{bmatrix} -\cos(\zeta_i + \zeta_r) & \sin(\zeta_i + \zeta_r) \\ \sin(\zeta_i + \zeta_r) & \cos(\zeta_i + \zeta_r) \end{bmatrix} \tag{4.3}
\end{aligned}$$

where (4.3) reduces to the form given in [15] for the monostatic case.

From (4.3), one can see that the co-polarization RCS peaks when both the incident and receive polarization is parallel ($\zeta_i = \zeta_r = 0^\circ$) or perpendicular ($\zeta_i = \zeta_r = 90^\circ$) to the dihedral seam, and that the cross-polarization RCS peaks at 45° from those orientations ($\zeta_i = \zeta_r = \pm 45^\circ, \pm 135^\circ$). At these angles, the co-polarization RCS is minimum. Further, at $\zeta_i = \zeta_r = \pm 22.5^\circ$, the co- and cross-polarization RCS is equivalent. This property makes dihedrals effective calibration devices for both co- and cross- polarization measurements. The following two sections will examine the predicted scattering for these cases.

4.5.1 Dihedral Oriented for High Cross-Pol Intensity.

The visualization of this scene is shown in Figure 4.19. The polarimetric scattering for a dihedral with sides 0.25m and length 0.5m at roll 45° and transmitter position $(\theta_t, \phi_t) = (90^\circ, 45^\circ)$ is shown in Figures 4.20-4.23. The quantitative summary of scattering at the peak forward scatter angle is given in Table 4.6. For this transmitter position, ζ_i in Equation (4.3) is equal to the dihedral roll angle of 45° , and ζ_r at the peak forward scatter angle is also 45° . Using Equation (4.3), the predicted scattering behavior for $\zeta_i = \zeta_r = 45^\circ$ is minimum magnitude for co-polarizations and maximum magnitude for cross-polarizations.

This analysis will examine the high magnitude polarizations (cross-pols) first, fol-

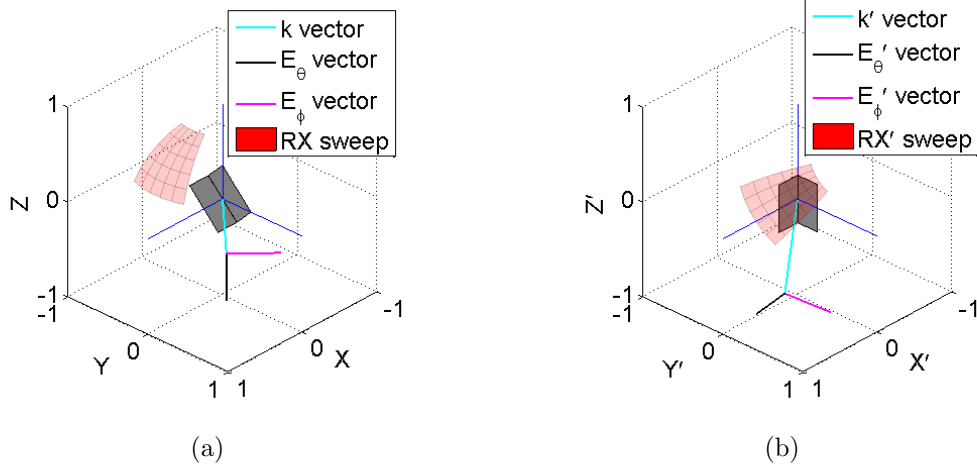


Figure 4.19. Geometry and TX/RX angles for scene with dihedral oriented for high cross-pol scattering, (a) global coordinate system, (b) target coordinate system. Dihedral is oriented at roll 45° from original position. Transmit location is $(\theta_t, \phi_t) = (90^\circ, 45^\circ)$ and $(\theta'_t, \phi'_t) = (120^\circ, 35.26^\circ)$ in the target coordinate system. Dihedral height is 0.5m, the sides are 0.25m. Prime notation used to indicate target coordinate system.

Table 4.6. Scattering amplitudes and differences at specular angle for dihedral oriented for high cross-pol intensity

Peak Magnitude (dBsm)	VV	HV	VH	HH
Model	-9.05	21.78	21.61	-5.48
SBR	-9.59	21.77	21.62	-5.74
MoM	-2.58	22.36	22.16	-3.13
Coherent Difference (dBsm)	VV	HV	VH	HH
Model-SBR	-33.05	-37.45	-37.44	-36.07
Model-MoM	-7.64	4.01	3.49	-5.81
SBR-MoM	-7.20	4.00	3.51	-5.83
Magnitude Ratio (dB)	VV	HV	VH	HH
Model / SBR	0.53	0.01	-0.01	0.26
Model / MoM	-6.47	-0.59	-0.54	-2.35
SBR / MoM	-7.00	-0.60	-0.54	-2.61

lowed by the low magnitude polarizations (co-pols), and finish by giving computation time for each simulation. The magnitude ratio at the peak forward scatter angle for the cross-pol terms shows excellent agreement for all three waveform comparisons (< 0.6 dB). The coherent difference between model and SBR predictions is extremely

low (< -37 dbsm), indicating that the model in this thesis is at least as accurate as SBR predictions for dihedrals oriented at for high cross-pol scattering. As in the analysis in Sections 4.4 and 4.4.1, there is significant coherent difference (4 dBsm) between the cross-pol model and MoM predictions. This behavior is in a band perpendicular to the dihedral seam, and does not significantly vary in magnitude over this range. This indicates that the coherent difference is most likely due to second order effects (diffraction, near-field interaction between two plates), which the GO-PO dihedral solution does not account for, and not errors in applying the arbitrary orientation transforms central to this thesis.

Comparisons for the low magnitude co-pols for this case are similar to the low magnitude cross-pols for a dihedral at the original orientation given in Section 4.3. While the model and SBR data is perfectly matched in magnitude and phase, the PO-based model and SBR predictions do not show perfect agreement in magnitude or phase with the exact MoM prediction. As explained in Section 4.3, this is because the PO-based predictions do not account for the dominant scattering behavior at these low magnitudes: near-field interaction between the dihedral plates and diffraction from the target edges.

Calculation time on Dell Precision 690TM workstations with one Quad 3.00 GHz Intel Xeon® processor and 32GB RAM for the $400(\theta_r) \times 400(\phi_r)$ dataset in this example is approximately 13.6 hours for MoM, 6 minutes for SBR, and 2.3 seconds for the model developed in this thesis. Again, these run times do not take into account time used for target mesh creation or modification for the SBR and MoM methods.

VV-polarization

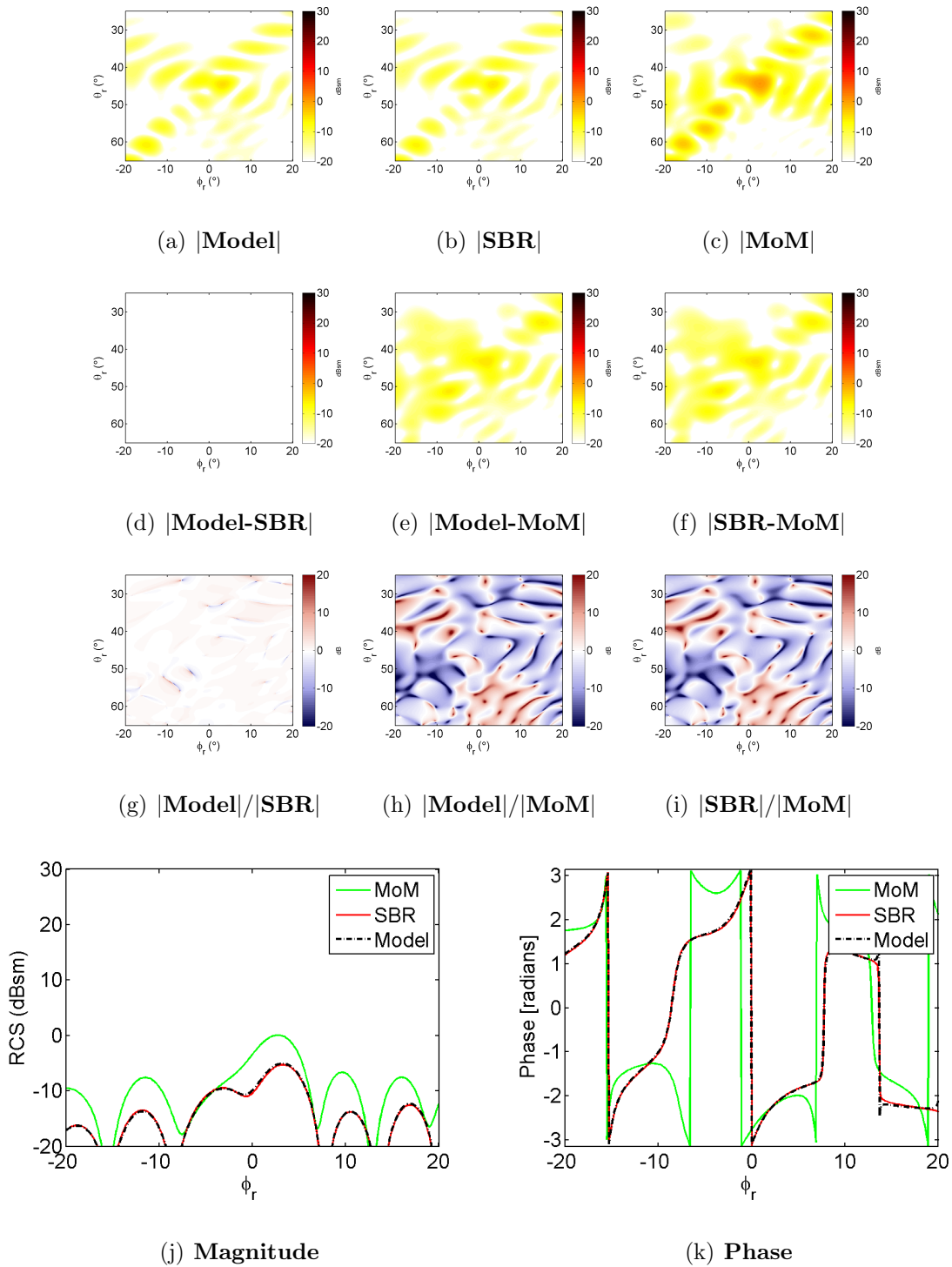


Figure 4.20. Comparison of VV-pol scattering for the dihedral oriented for high cross-pol RCS shown in Figure 4.19 with roll 45° and incident aspect $(\theta_t, \phi_t) = (90^\circ, 45^\circ)$. Figures a-c show the magnitude response for the model developed in this thesis, SBR, and MoM data respectively. Figures d-f show the coherent difference, and g-i show the magnitude ratio between these waveforms. Figures j and k show magnitude and phase for an azimuth sweep for constant elevation through the peak response, in this case $\theta_r = 45^\circ$.

HV-polarization

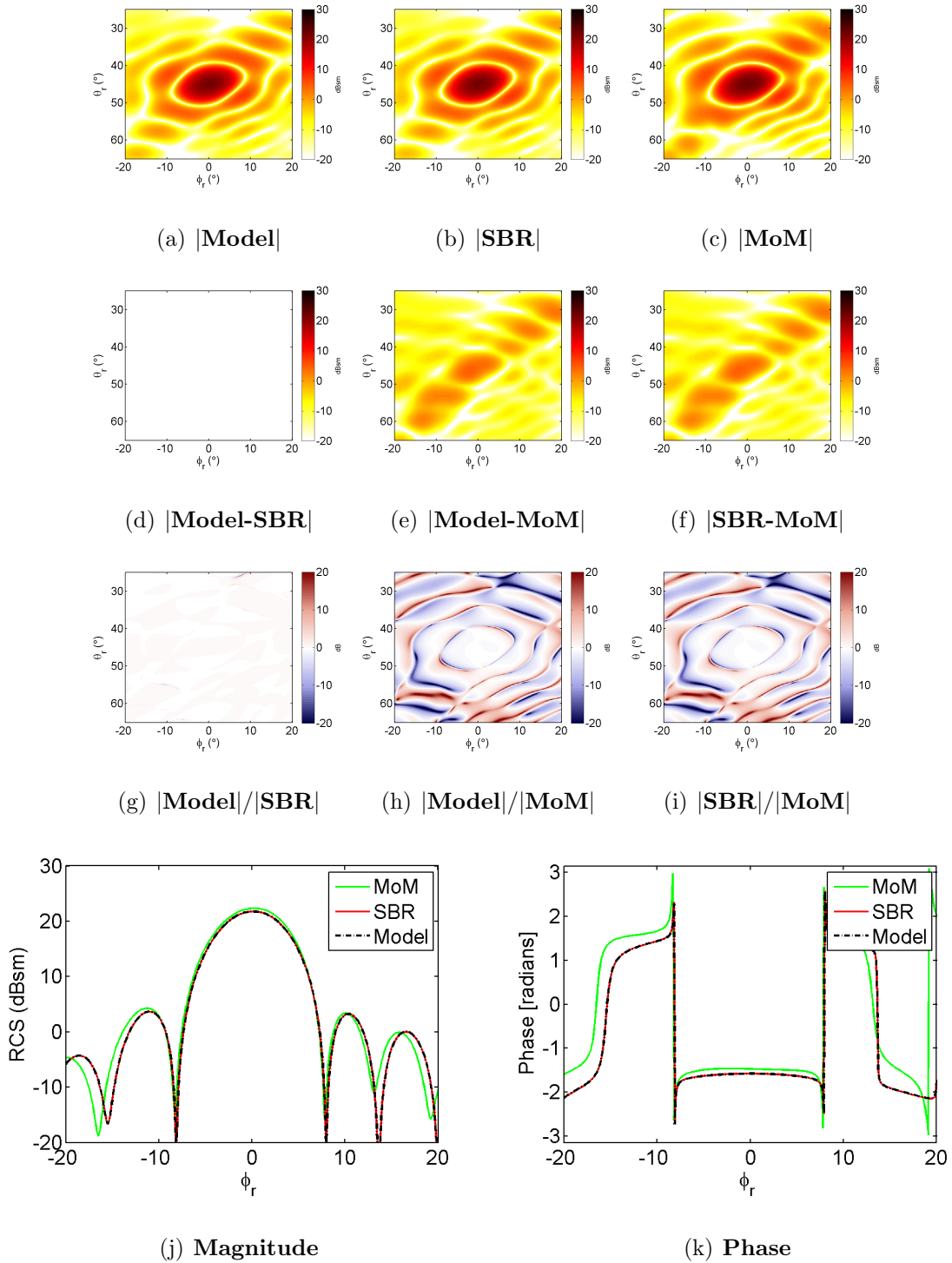


Figure 4.21. Comparison of HV-pol scattering for the dihedral oriented for high cross-pol RCS shown in Figure 4.19 with roll 45° and incident aspect $(\theta_t, \phi_t) = (90^\circ, 45^\circ)$. Figures a-c show the magnitude response for the model developed in this thesis, SBR, and MoM data respectively. Figures d-f show the coherent difference, and g-i show the magnitude ratio between these waveforms. Figures j and k show magnitude and phase for an azimuth sweep for constant elevation through the peak response, in this case $\theta_r = 45^\circ$.

VH-polarization

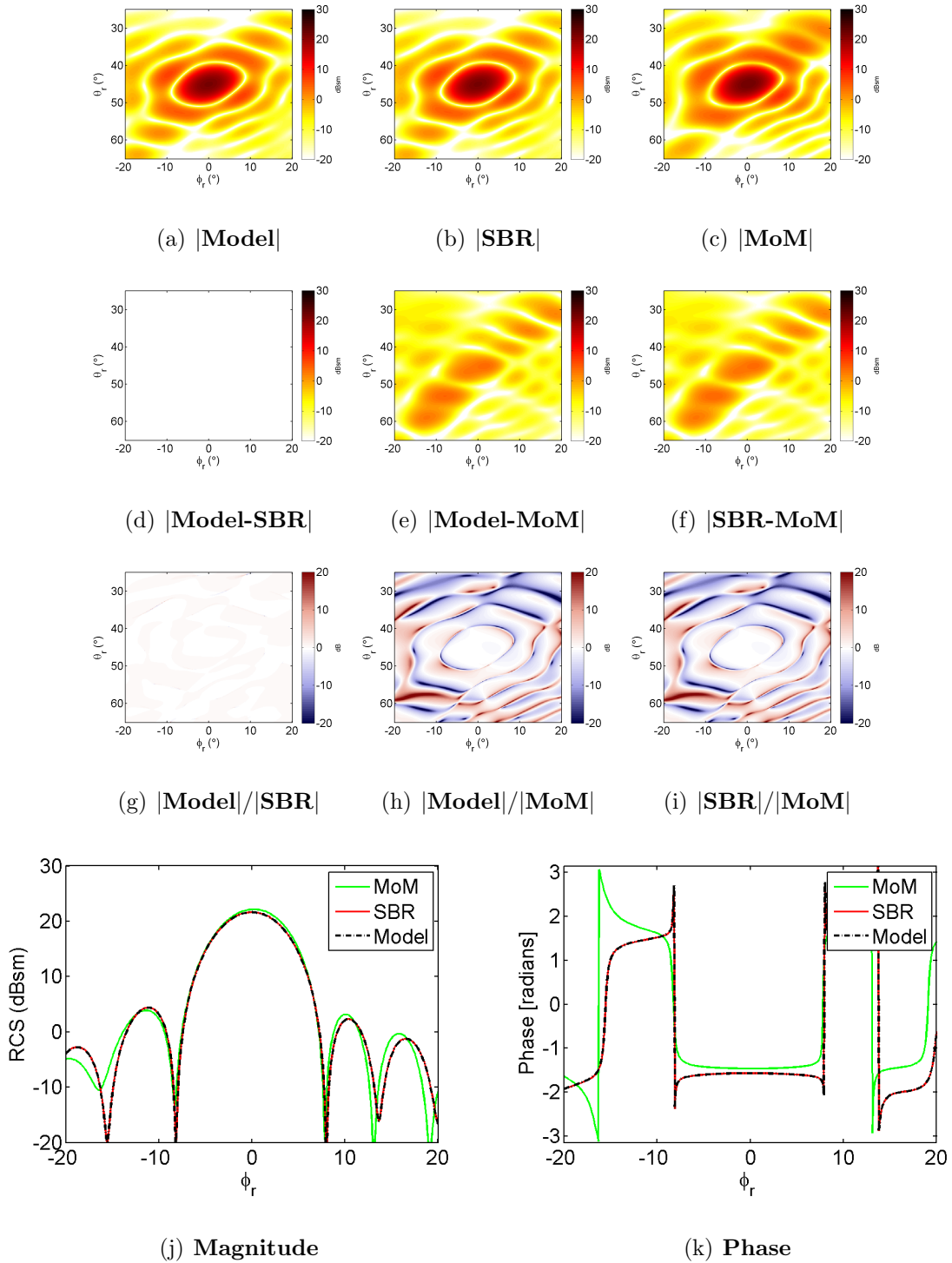


Figure 4.22. Comparison of VH-pol scattering for the dihedral oriented for high cross-pol RCS shown in Figure 4.19 with roll 45° and incident aspect $(\theta_t, \phi_t) = (90^\circ, 45^\circ)$. Figures a-c show the magnitude response for the model developed in this thesis, SBR, and MoM data respectively. Figures d-f show the coherent difference, and g-i show the magnitude ratio between these waveforms. Figures j and k show magnitude and phase for an azimuth sweep for constant elevation through the peak response, in this case $\theta_r = 45^\circ$.

HH-polarization

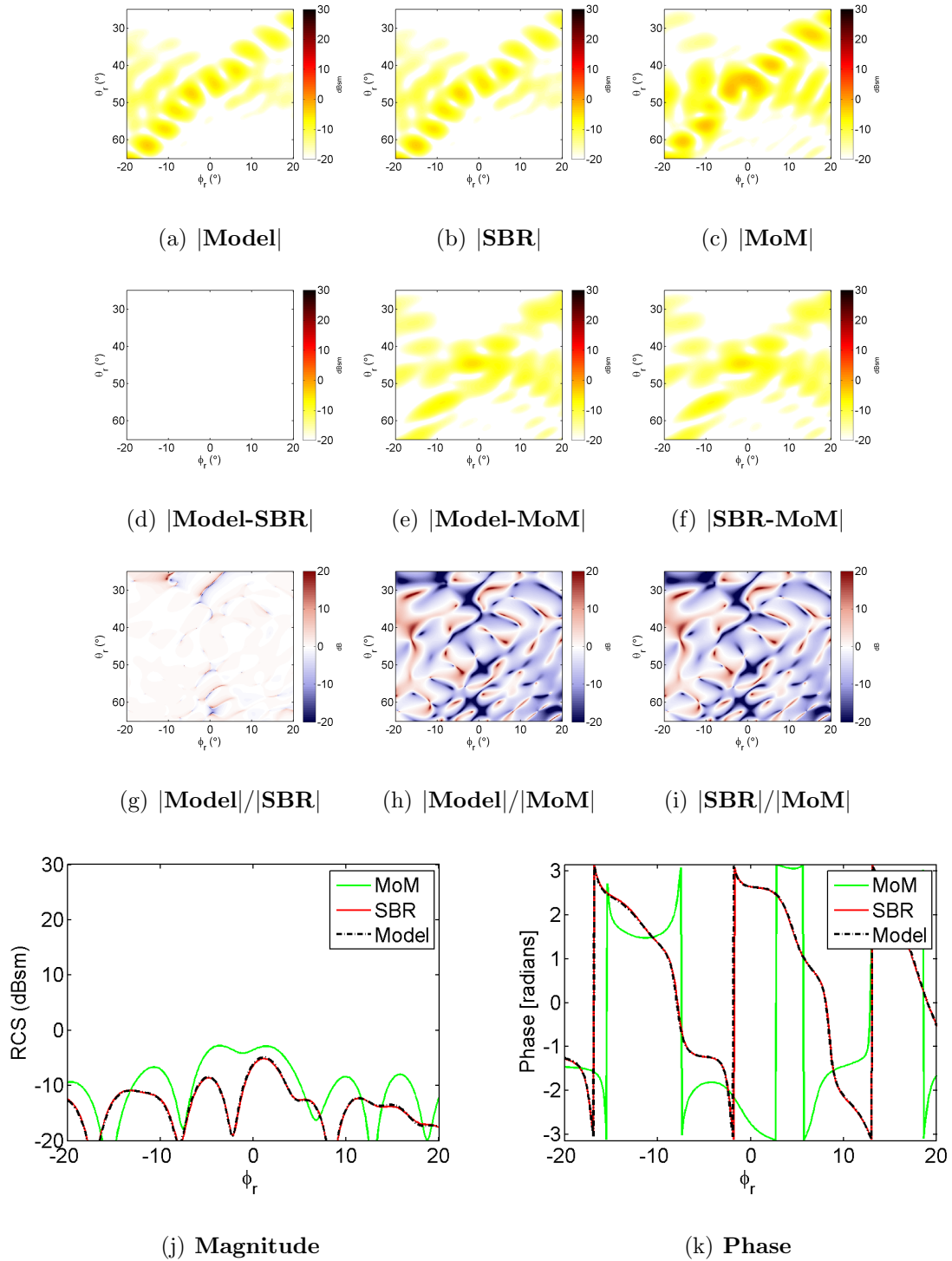


Figure 4.23. Comparison of HH-pol scattering for the dihedral oriented for high cross-pol RCS shown in Figure 4.19 with roll 45° and incident aspect $(\theta_t, \phi_t) = (90^\circ, 45^\circ)$. Figures a-c show the magnitude response for the model developed in this thesis, SBR, and MoM data respectively. Figures d-f show the coherent difference, and g-i show the magnitude ratio between these waveforms. Figures j and k show magnitude and phase for an azimuth sweep for constant elevation through the peak response, in this case $\theta_r = 45^\circ$.

4.5.2 Dihedral Oriented for Similar Co/Cross-Pol Intensity.

The orientation of this scene is shown in Figure 4.24. The polarimetric scattering for a dihedral with sides 0.25m and length 0.5m at roll 22.5° and transmitter position $(\theta_t, \phi_t) = (90^\circ, 45^\circ)$ is shown in Figures 4.25-4.28, and a quantitative summary of scattering at the peak forward scatter angle is given in Table 4.7. Using Equation (4.3) and $\zeta_i = \zeta_r = 22.5^\circ$, the predicted scattering behavior for this target orientation is similar intensity for co- and cross- polarizations.

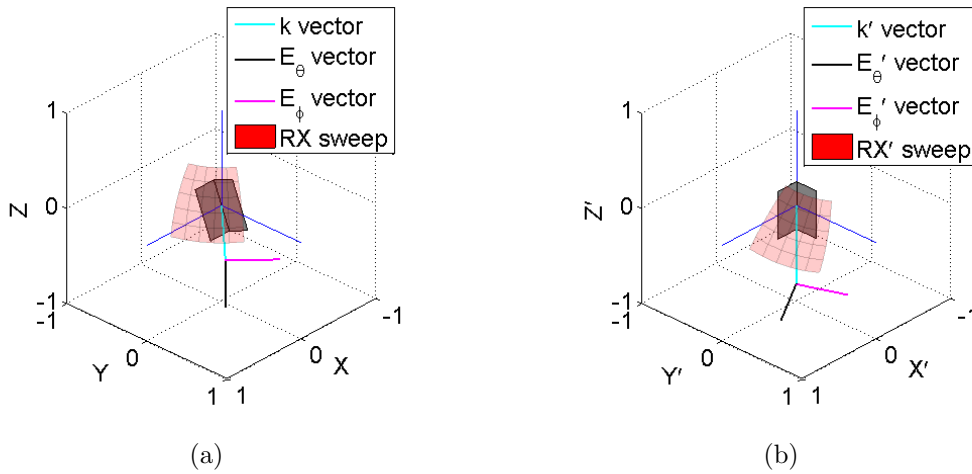


Figure 4.24. Geometry and TX/RX angles for scene with dihedral oriented for similar co/cross-pol scattering, (a) global coordinate system, (b) target coordinate system. Dihedral is oriented at roll 22.5° from original position. Transmit location is $(\theta_t, \phi_t) = (90^\circ, 45^\circ)$ and $(\theta'_t, \phi'_t) = (105.7^\circ, 42.73^\circ)$ in the target coordinate system. Dihedral height is 0.5m, the sides are 0.25m. Prime notation used to indicate target coordinate system.

This combination of dihedral orientation and transmitter position produces significant intensity across all four polarizations. For this reason, the three prediction methods show excellent agreement in magnitude (< 0.38 dB magnitude ratio) at the forward scatter angle. Like the other cases examined in this chapter, the coherent difference between model and SBR predictions is extremely low (< -33 dBsm). Also like the previously examined cases, there is a coherent difference mismatch (≈ 7 dBsm, about 15 dB lower than predicted intensity at the forward scatter angle) between

Table 4.7. Scattering amplitudes and differences at specular angle for dihedral oriented for similar co/cross-pol intensity

Peak Magnitude (dBsm)	VV	HV	VH	HH
Model	23.22	20.08	20.05	22.96
SBR	23.21	20.07	20.05	22.97
MoM	23.59	20.38	20.30	23.16
Coherent Difference (dBsm)	VV	HV	VH	HH
Model-SBR	-33.18	-49.02	-51.01	-37.71
Model-MoM	6.86	4.29	3.93	7.75
SBR-MoM	6.84	4.29	3.94	7.77
Magnitude Ratio (dB)	VV	HV	VH	HH
Model / SBR	0.01	0.00	0.00	-0.01
Model / MoM	-0.37	-0.30	-0.26	-0.20
SBR / MoM	-0.38	-0.30	-0.26	-0.19

the PO-based and more exact MoM predictions. As in the 45° roll case, this complex difference band is positioned along an axis perpendicular to the dihedral axis and is produced by a small phase mismatch due to differences in how the double bounce scattering mechanism is calculated.

Calculation time on Dell Precision 690TM workstations with one Quad 3.00 GHz Intel Xeon[®] processor and 32GB RAM for the $400(\theta_r) \times 400(\phi_r)$ dataset in this example is approximately 13.5 hours for MoM, 6 minutes for SBR, and 2.3 seconds for the model developed in this thesis. Again, calculations are performed on quad-core workstations with 32GB RAM and do not take into account time used for target mesh creation or modification for the SBR and MoM methods.

VV-polarization

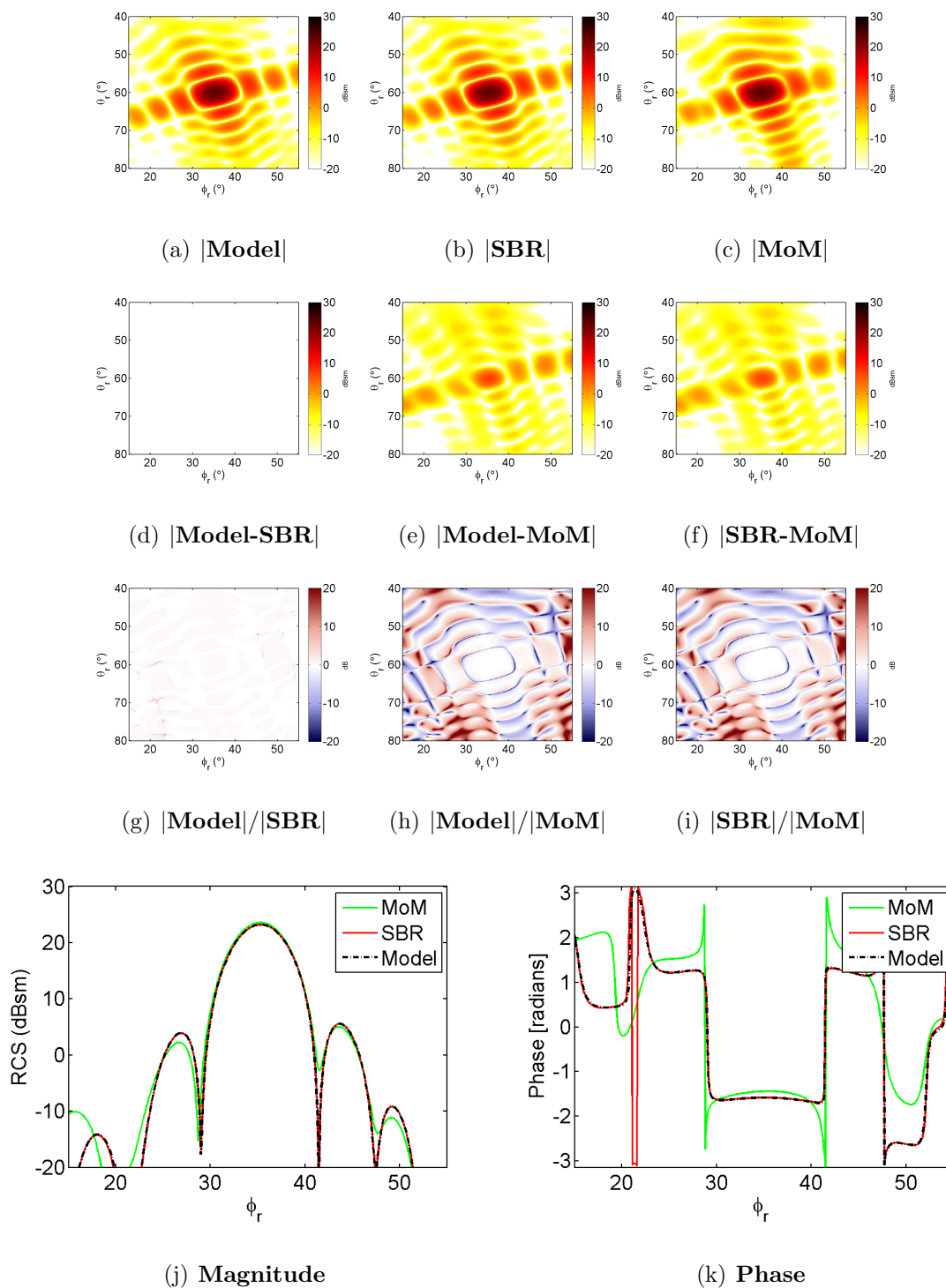


Figure 4.25. Comparison of VV-pol scattering for the dihedral oriented for similar co/cross-pol RCS shown in Figure 4.24 with roll 22.5° and incident aspect $(\theta_t, \phi_t) = (90^\circ, 45^\circ)$. Figures a-c show the magnitude response for the model developed in this thesis, SBR, and MoM data respectively. Figures d-f show the coherent difference, and g-i show the magnitude ratio between these waveforms. Figures j and k show magnitude and phase for an azimuth sweep for constant elevation through the peak response, in this case $\theta_r = 60^\circ$.

HV-polarization

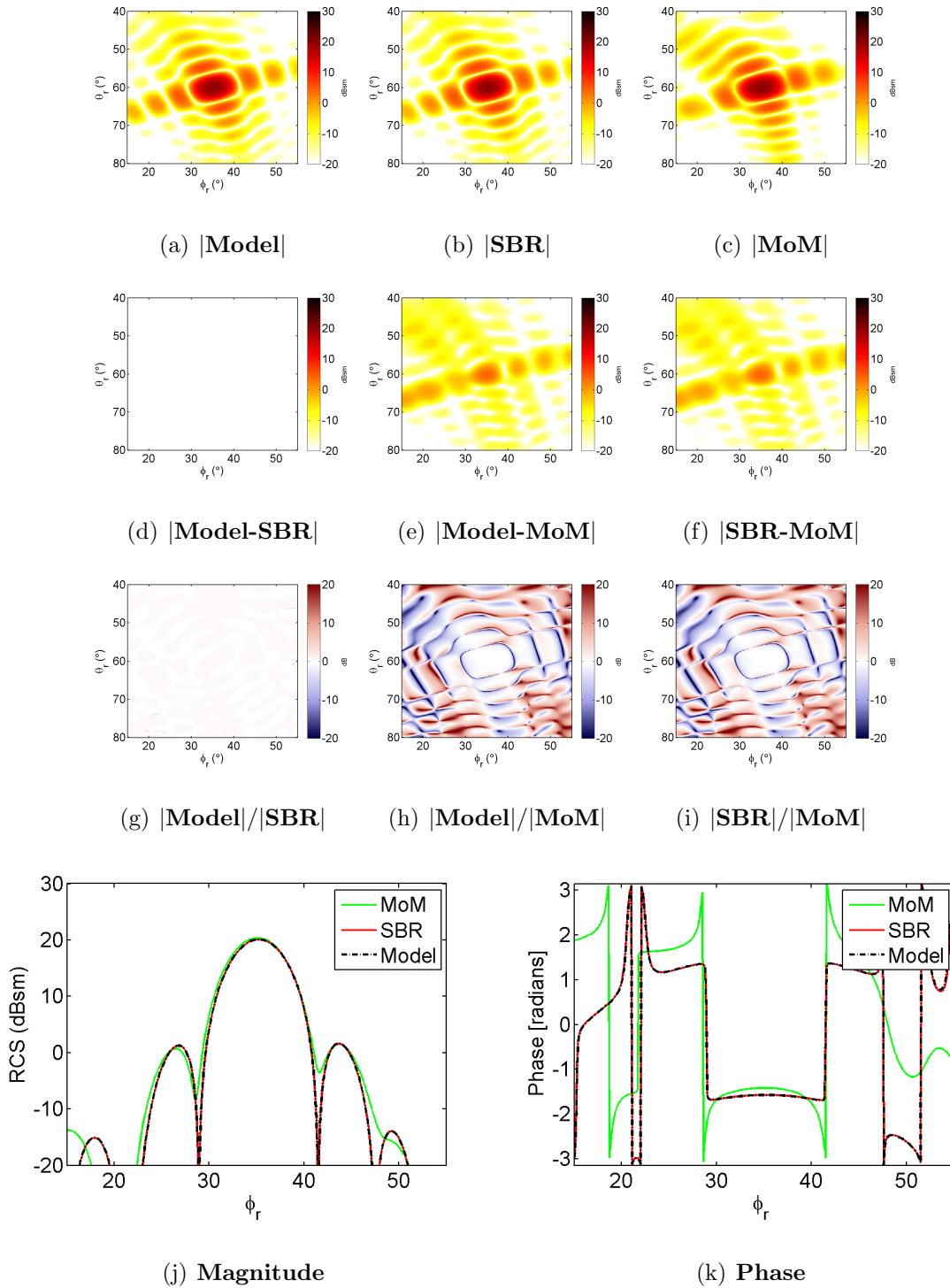


Figure 4.26. Comparison of HV-pol scattering for the dihedral oriented for similar co/cross-pol RCS shown in Figure 4.24 with roll 22.5° and incident aspect $(\theta_t, \phi_t) = (90^\circ, 45^\circ)$. Figures a-c show the magnitude response for the model developed in this thesis, SBR, and MoM data respectively. Figures d-f show the coherent difference, and g-i show the magnitude ratio between these waveforms. Figures j and k show magnitude and phase for an azimuth sweep for constant elevation through the peak response, in this case $\theta_r = 60^\circ$.

VH-polarization

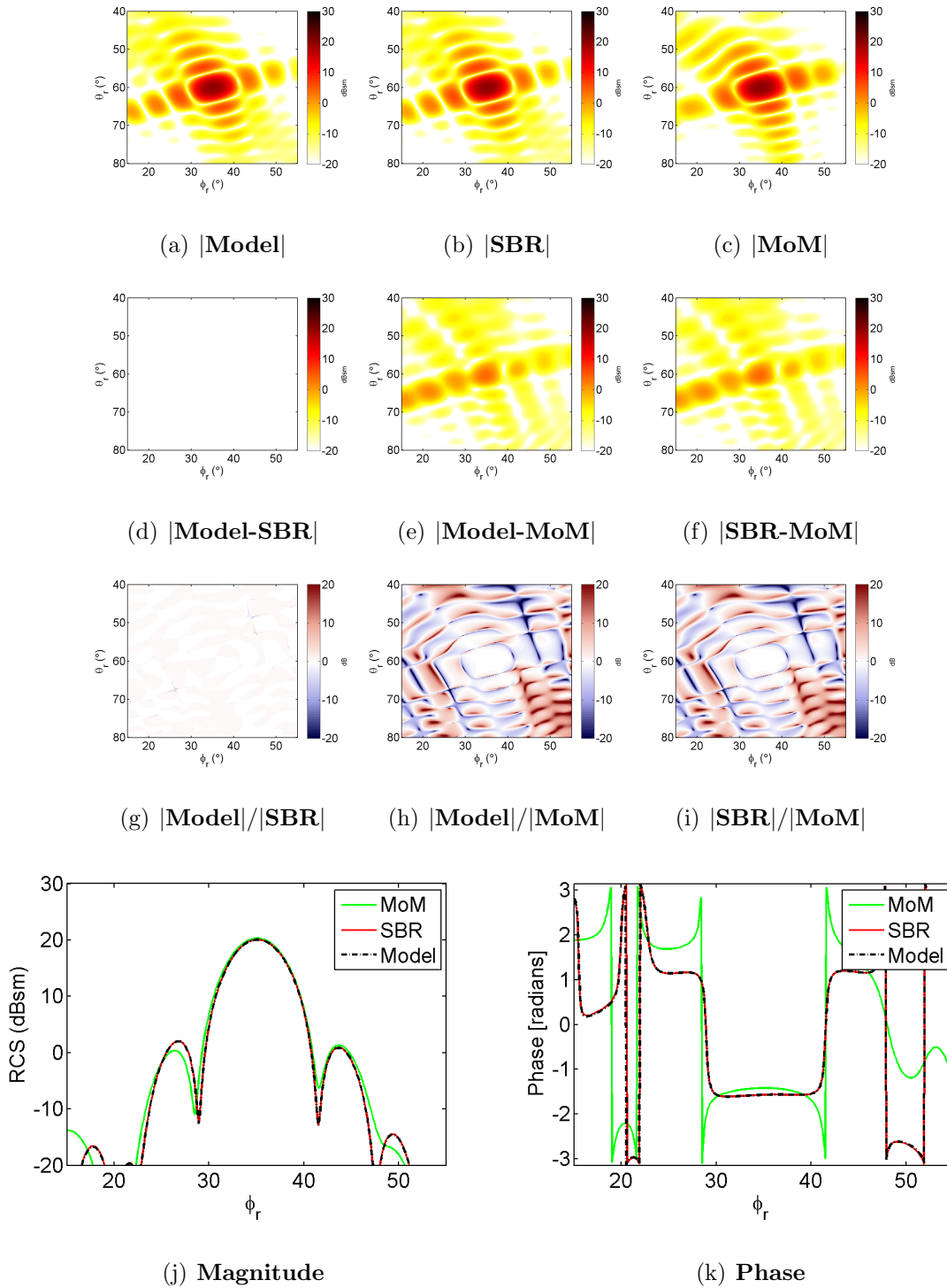


Figure 4.27. Comparison of VH-pol scattering for the dihedral oriented for similar co/cross-pol RCS shown in Figure 4.24 with roll 22.5° and incident aspect $(\theta_t, \phi_t) = (90^\circ, 45^\circ)$. Figures a-c show the magnitude response for the model developed in this thesis, SBR, and MoM data respectively. Figures d-f show the coherent difference, and g-i show the magnitude ratio between these waveforms. Figures j and k show magnitude and phase for an azimuth sweep for constant elevation through the peak response, in this case $\theta_r = 60^\circ$.

HH-polarization

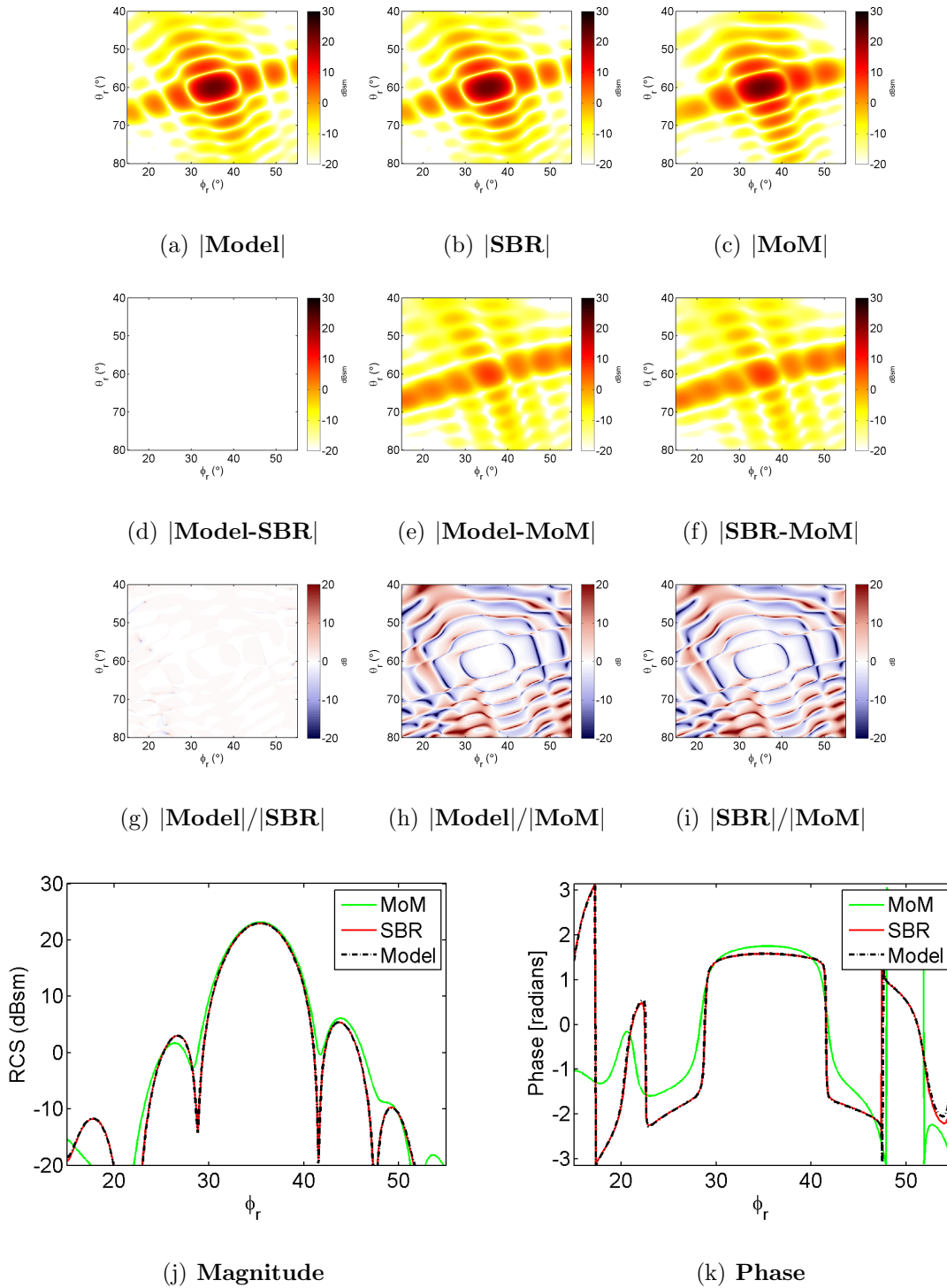


Figure 4.28. Comparison of HH-pol scattering for the dihedral oriented for similar co/cross-pol RCS shown in Figure 4.24 with roll 22.5° and incident aspect $(\theta_t, \phi_t) = (90^\circ, 45^\circ)$. Figures a-c show the magnitude response for the model developed in this thesis, SBR, and MoM data respectively. Figures d-f show the coherent difference, and g-i show the magnitude ratio between these waveforms. Figures j and k show magnitude and phase for an azimuth sweep for constant elevation through the peak response, in this case $\theta_r = 60^\circ$.

4.6 Summary

This chapter began by examining the GO-PO solution, SBR, and MoM scattering predictions for a dihedral orientated with its seam centered along the z axis. The next case examined was a dihedral at roll= 60° , pitch= 45° , yaw= 10° and translated $X=0.2\text{m}$, $Y=-0.3\text{m}$, $Z=0.4\text{m}$ from the origin in order to verify that the model in this thesis successfully accounted for changes to orientation and position. Following this, two cases were provided which compared measured data collected in the AFIT RCS range with four prediction methods: SBR, MoM, PM, and the model in this thesis. Finally, two cases were examined that showcase dihedral orientations commonly used for calibration purposes.

The six cases provided in this chapter show that the model developed in this thesis is capable of accurately modeling a dihedral at any orientation and position. The model shows excellent agreement with SBR predictions in magnitude and phase for each case examined. It also is closely matched with MoM predictions in magnitude. For some combinations of dihedral orientation and TX position, there are small phase inaccuracies between the model and MoM predictions. However, the coherent difference between SBR and MoM is identical to the coherent difference between model and MoM for these cases. This indicates that phase inaccuracies are due to inherent differences between GO-PO assumptions and an exact solution, and not a result of the transforms required for arbitrary orientation and position.

In addition to accurately modeling the scattering behavior, the model in this thesis is computationally efficient. Typical run times for these six cases were 13 hours for MoM, 6 minutes for SBR, and 2 seconds for the model (see Table 4.8). Additionally, the model in this thesis is easily added to other applications as a MATLABTM function.

Table 4.8. Computation time for cases examined

Case	MoM (hours)	SBR (minutes)	Model (seconds)
Dihedral at original orientation (Section 4.3)	13.5	6	2.6
Dihedral with rotation and translation (Section 4.4.1)	13.7	7	2.7
Dihedral orientated for high cross-pol intensity (Section 4.5.1)	13.6	6	2.3
Dihedral orientated for similar co/cross-pol intensity (Section 4.5.2)	13.5	6	2.3

V. Conclusion and Future Work

5.1 Conclusion

The model developed in this thesis accurately accounts for the effects of arbitrary orientation and position. It is applied to the bistatic 3D polarimetric scattering solutions for a dihedral and plate target. This model produces scattering data that shows excellent agreement in magnitude and phase with SBR predictions. Comparisons to MoM predictions show excellent agreement in magnitude. For some combinations of target orientation and TX position, there are small phase differences between the model and MoM predictions. It is shown that these phase inaccuracies are due to inherent differences between the underlying scattering solutions (PO approximation, GO assumption for dihedral double-bounce mechanism) and the more exact MoM solution and not due to the methods used to account for arbitrary orientation and position. Furthermore, the model in this thesis requires a fraction of the computation time required for SBR and MoM predictions. Due to the model's excellent accuracy and timeliness, it shows great promise for application to bistatic SAR ATR and airborne bistatic SAR calibration.

5.2 Future Work

There are many different avenues for future work related to the model developed in this thesis. In terms of increasing the accuracy of the underlying scattering solutions, diffraction terms and non-PEC materials should be investigated. Validating the diffraction terms would require a SBR simulation which takes into account edge scattering. Validating the non-PEC material solution would require a new set of SBR and MoM simulations using appropriate boundary conditions. If even more accuracy is desired, the method developed in [9] for monostatic dihedral scattering should be in-

investigated for extension to the bistatic case. That method uses numerical integration to find the PO near-field integral for the double-bounce reflection. These solutions would show reduced coherent difference when compared to MoM predictions at the cost of computation time.

There are also research possibilities related to future bistatic ATR applications. First, the efficiency and accuracy of feature estimation using the methods described in [11] should be investigated using the model developed in this thesis compared to the previously developed 3D parametric models. The impacts of increased model complexity should also be studied for models that account for diffraction terms and non-PEC materials. Also, other canonical target solutions should be investigated. The trihedral should be examined using the same GO-PO method that is developed in [13] for the dihedral. However, a trihedral GO-PO solution will most likely suffer in accuracy more than the dihedral case due to using a planar wave assumption for two consecutive double-bounce reflections. Additionally, GO-PO solutions for dihedrals with non-90° interior angles could be developed as separate target types. GO-PO solutions for obtuse ($> 90^\circ$) angles will be more accurate than acute ($< 90^\circ$) angles which have multiple-bounce scattering effects. Future target scattering solutions can be extended to arbitrary orientation and position using the method described in this thesis.

The model in this thesis should also be investigated for use in bistatic SAR calibration. Because the model is capable of quickly predicting accurate scattering behavior for a dihedral at any orientation and position and for any bistatic TX/RX angles within the dihedral interior, it could be used to calibrate bistatic SAR data scenes containing known dihedral targets in near-real time.

Appendix A. Additional Data Comparisons

This appendix contains two additional data comparisons used in the derivation of the arbitrary position and orientation PO solution. Simple plate targets were used when developing the MATLABTM function to account for arbitrary orientation and position. Advantages to using a simple plate compared to the dihedral include simpler scattering behavior and more efficient creation of SBR and MoM prediction data for benchmark comparisons during MATLABTM code development.

1.1 Simple Plate

This section provides comparisons between the model for a simple plate developed in Chapter III vs. SBR and MoM predictions. First, a plate orientated as shown in Figure 3.1 is examined to verify the 3D bistatic PO model developed in Section 3.2.2. Then, to further verify the method to account for arbitrary orientation and position developed in Section 3.4, an example scene is examined where the plate's roll, pitch, yaw, and translation from the origin along all three axes are nonzero.

1.1.1 Plate at Original Orientation and Position.

The visualization for this scene is shown in Figure A.1. The 3D polarimetric scattering for a plate centered in the XY plane with sides 0.25m and length 0.5m and transmitter position $(\theta_t, \phi_t) = (45^\circ, -60^\circ)$ is shown in Figures A.2-A.5. The quantitative summary of scattering at the peak forward scatter angle is given in Table A.1.

Results for the plate centered in the XY plane are similar to results for the dihedral at original orientation and position examined in Section 4.3. The plate PO model closely matches SBR data in magnitude and phase, and shows excellent agreement

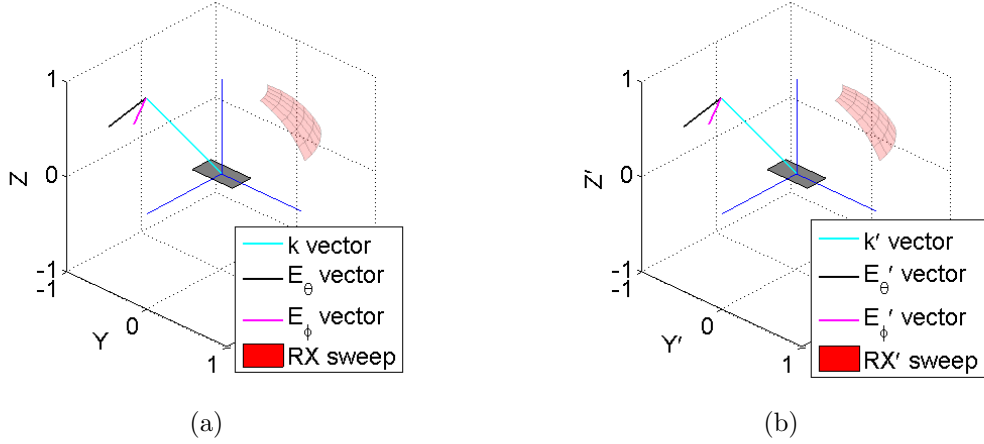


Figure A.1. Geometry and TX/RX angles for plate centered in XY plane, (a) global coordinate system, (b) target coordinate system. Transmit location is $(\theta_t, \phi_t) = (45^\circ, -60^\circ)$ and $(\theta'_t, \phi'_t) = (45^\circ, -60^\circ)$ in the target coordinate system. Plate dimensions are $W = 0.5\text{m}$, $d = 0.25\text{m}$. Prime notation used to indicate target coordinate system.

Table A.1. Scattering amplitudes and differences at specular angle for plate at original orientation and position

Peak Magnitude (dBsm)	VV	HV	VH	HH
Model	20.40	-3.19	-8.44	20.38
SBR	20.40	-3.19	-8.43	20.38
MoM	20.62	-0.56	-0.14	20.48
Coherent Difference (dBsm)	VV	HV	VH	HH
Model-SBR	-89.10	-83.59	-91.17	-89.17
Model-MoM	-5.25	-12.05	-4.32	-8.29
SBR-MoM	-5.25	-12.06	-4.32	-8.29
Magnitude Ratio (dB)	VV	HV	VH	HH
Model / SBR	0.00	0.00	-0.00	-0.00
Model / MoM	-0.23	-2.63	-8.29	-0.10
SBR / MoM	-0.23	-2.63	-8.29	-0.10

with MoM predictions in magnitude but not phase. This is due to inherent differences in the PO approximation compared to an exact solution.

Calculation time on Dell Precision 690TM workstations with one Quad 3.00 GHz Intel Xeon® processor and 32GB RAM for the $400(\theta_r) \times 400(\phi_r)$ dataset in this

example is approximately 6.6 hours for MoM, 3.4 minutes for SBR, and 0.9 seconds for the model developed in this thesis. Again, calculations are performed on quad-core workstations with 32GB RAM and do not take into account time used for target mesh creation or modification required for the SBR and MoM methods.

VV-polarization

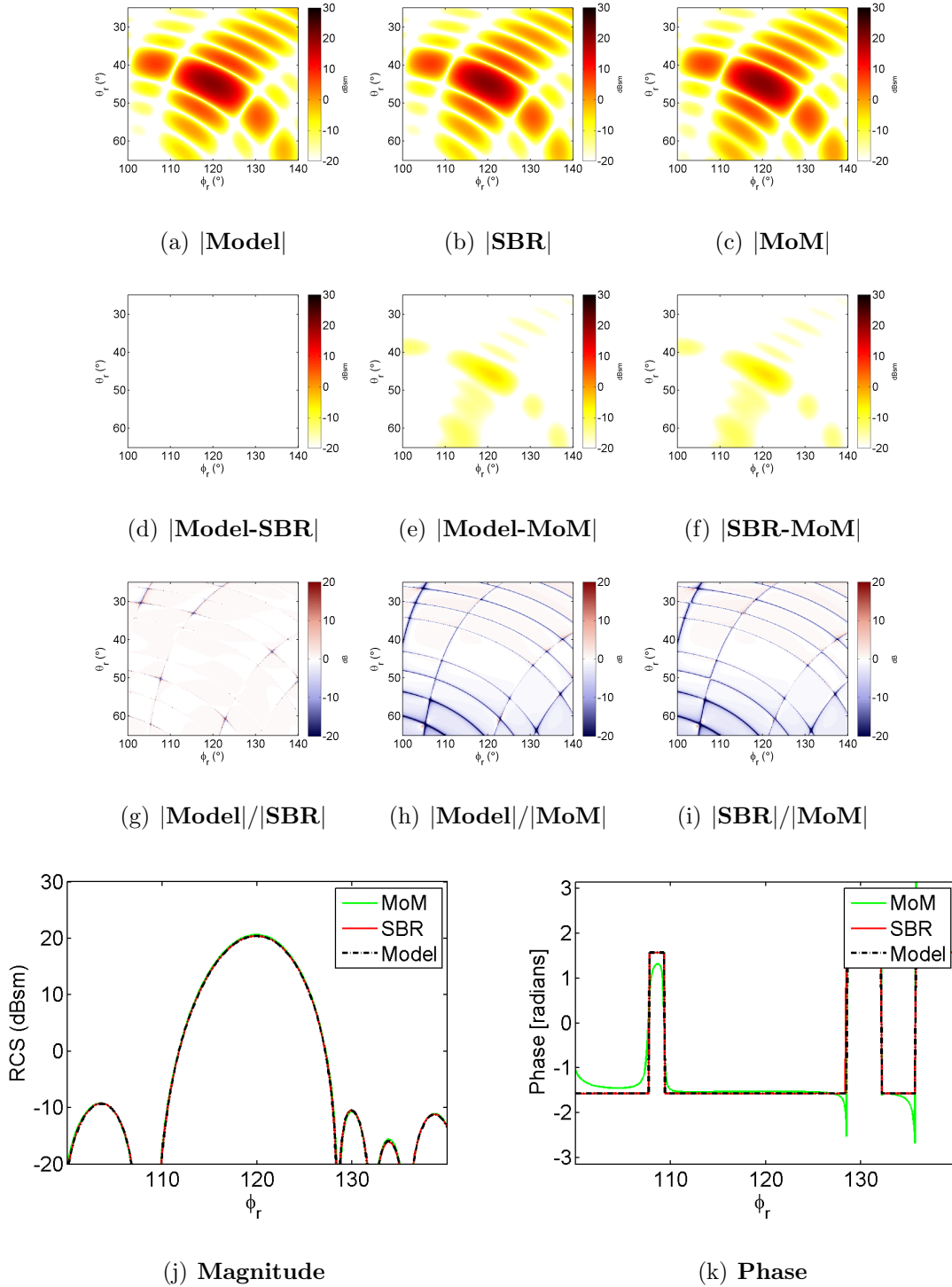


Figure A.2. Comparison of VV-pol scattering for the plate centered in XY plane shown in Figure A.1 with incident aspect $(\theta_t, \phi_t) = (45^\circ, -60^\circ)$. Figures a-c show the magnitude response for the model developed in this thesis, SBR, and MoM data respectively. Figures d-f show the coherent difference, and g-i show the magnitude ratio between these waveforms. Figures j and k show magnitude and phase for an azimuth sweep for constant elevation through the peak response, in this case $\theta_r = 45^\circ$.

HV-polarization

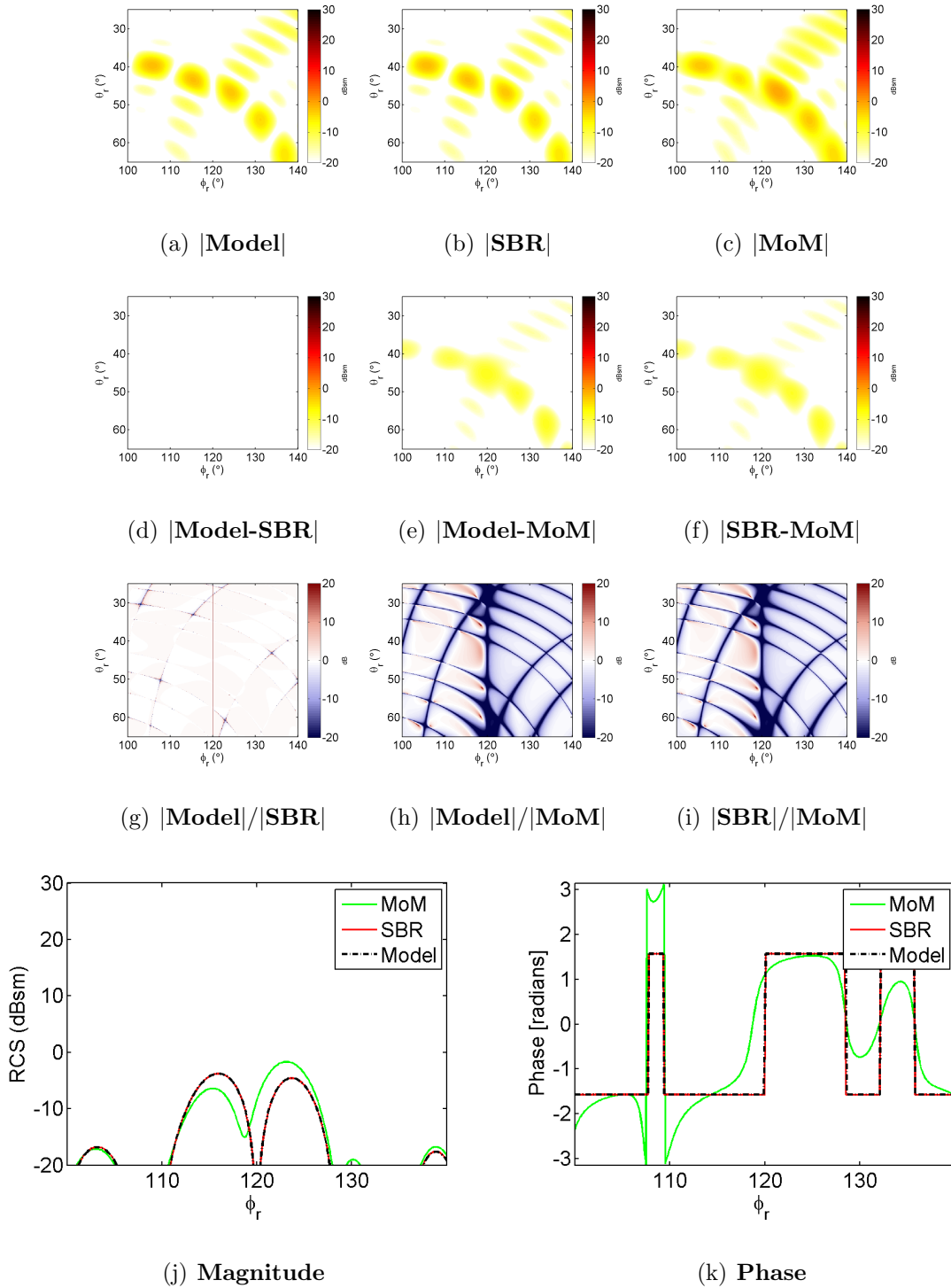


Figure A.3. Comparison of HV-pol scattering for the plate centered in XY plane shown in Figure A.1 with incident aspect $(\theta_t, \phi_t) = (45^\circ, -60^\circ)$. Figures a-c show the magnitude response for the model developed in this thesis, SBR, and MoM data respectively. Figures d-f show the coherent difference, and g-i show the magnitude ratio between these waveforms. Figures j and k show magnitude and phase for an azimuth sweep for constant elevation through the peak response, in this case $\theta_r = 45^\circ$.

VH-polarization

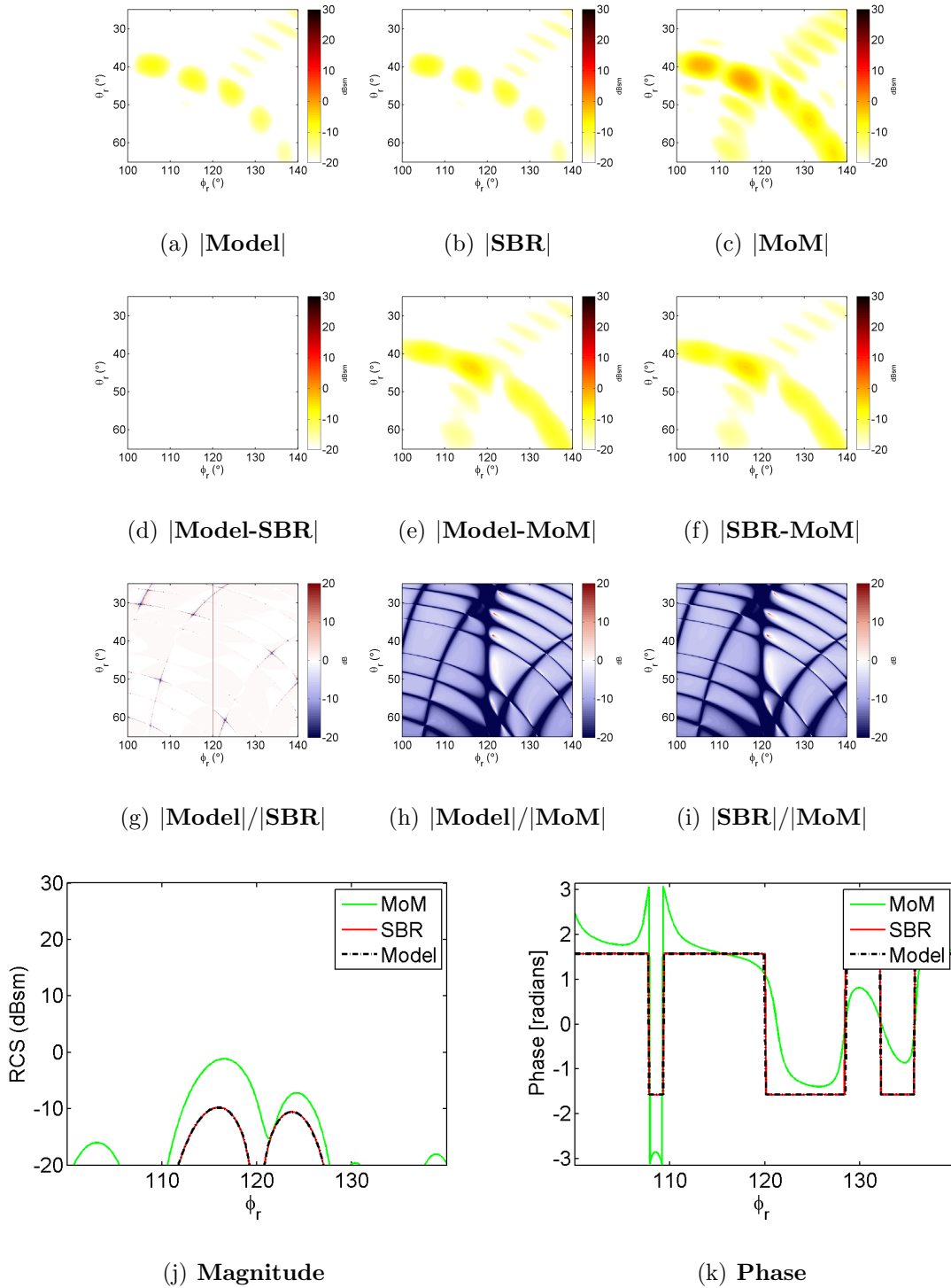


Figure A.4. Comparison of VH-pol scattering for the plate centered in XY plane shown in Figure A.1 with incident aspect $(\theta_t, \phi_t) = (45^\circ, -60^\circ)$. Figures a-c show the magnitude response for the model developed in this thesis, SBR, and MoM data respectively. Figures d-f show the coherent difference, and g-i show the magnitude ratio between these waveforms. Figures j and k show magnitude and phase for an azimuth sweep for constant elevation through the peak response, in this case $\theta_r = 45^\circ$.

HH-polarization

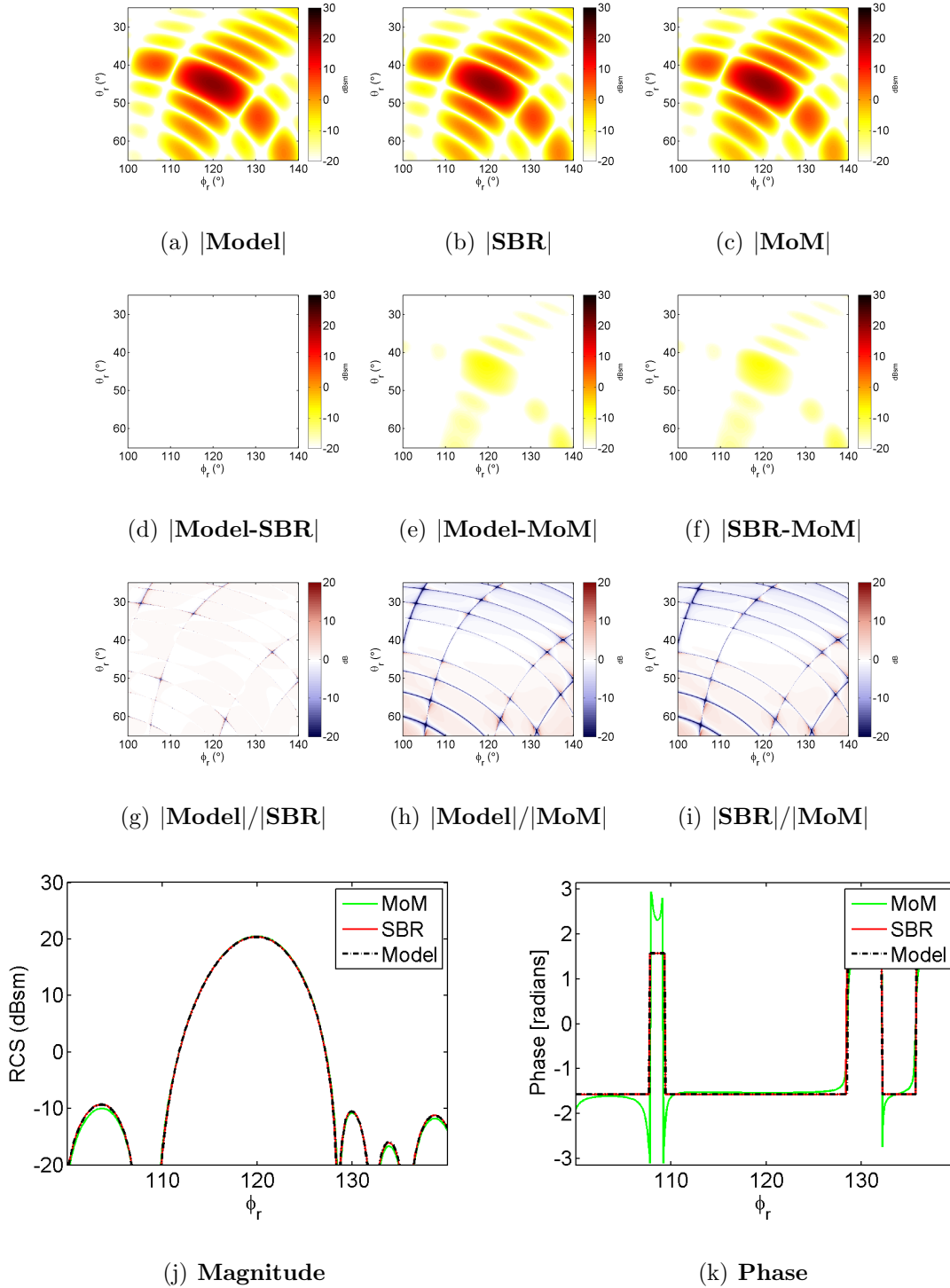


Figure A.5. Comparison of HH-pol scattering for the plate centered in XY plane shown in Figure A.1 with incident aspect $(\theta_t, \phi_t) = (45^\circ, -60^\circ)$. Figures a-c show the magnitude response for the model developed in this thesis, SBR, and MoM data respectively. Figures d-f show the coherent difference, and g-i show the magnitude ratio between these waveforms. Figures j and k show magnitude and phase for an azimuth sweep for constant elevation through the peak response, in this case $\theta_r = 45^\circ$.

1.1.2 Plate at Non-Original Orientation and Position.

The visualization for this scene is shown in Figure A.6. The 3D polarimetric scattering for a plate with roll= -40° , pitch= 55° , yaw= 65° , and translated $X = -0.3\text{m}$, $Y=0.6\text{m}$, and $Z=-0.1\text{m}$, with transmitter position $(\theta_t, \phi_t) = (90^\circ, 30^\circ)$ is shown in Figures A.7-A.10. The plate dimensions are sides $d = 0.25\text{m}$ and length $W = 0.5\text{m}$. The quantitative summary of scattering at the peak forward scatter angle is given in Table A.2.

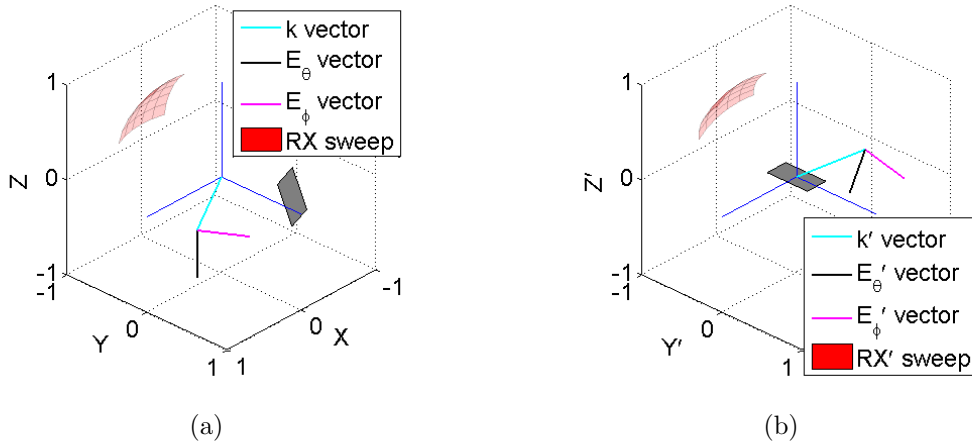


Figure A.6. Geometry and TX/RX angles for rotated and translated plate, (a) global coordinate system, (b) target coordinate system. Plate is at roll -40° , pitch 55° , yaw -65° and translated $X=-0.3\text{m}$, $Y=0.6\text{m}$, $Z=-0.1\text{m}$ from the origin. Transmit location is $(\theta_t, \phi_t) = (90^\circ, 30^\circ)$ and $(\theta'_t, \phi'_t) = (54.15^\circ, 93.54^\circ)$ in the target coordinate system. Plate dimensions are $W = 0.5\text{m}$, $d = 0.25\text{m}$. Prime notation used to indicate target coordinate system.

Table A.2. Scattering amplitudes and differences at specular angle for plate at non-original orientation and position

Peak Magnitude (dBsm)	VV	HV	VH	HH
Model	15.84	15.57	15.68	15.88
SBR	15.84	15.57	15.68	15.87
MoM	15.36	16.53	15.51	17.14
Coherent Difference (dBsm)	VV	HV	VH	HH
Model-SBR	-53.36	-53.51	-53.39	-53.29
Model-MoM	-9.03	0.67	-5.44	3.89
SBR-MoM	-9.08	0.68	-5.45	3.90
Magnitude Ratio (dB)	VV	HV	VH	HH
Model / SBR	0.00	0.00	0.00	0.00
Model / MoM	0.48	-0.96	0.17	-1.26
SBR / MoM	0.48	-0.96	0.16	-1.27

Results for this case closely match the rotated and translated dihedral examined in Section 4.4.1. The model in this thesis accurately accounts for changes to orientation and position. Note the model also accounts for depolarizing effects (cross-pols have similar magnitude to co-pols) due to the change in orientation and PEC boundary conditions ($\hat{n} \times \vec{E}' = 0$).

Calculation time on Dell Precision 690TM workstations with one Quad 3.00 GHz Intel Xeon® processor and 32GB RAM for the $400(\theta_r) \times 400(\phi_r)$ dataset in this example is approximately 6.75 hours for MoM, 4.2 minutes for SBR, and 0.9 seconds for the model developed in this thesis. Again, calculations are performed on quad-core workstations with 32GB RAM and do not take into account time used for target mesh creation or modification needed for the SBR and MoM methods.

VV-polarization

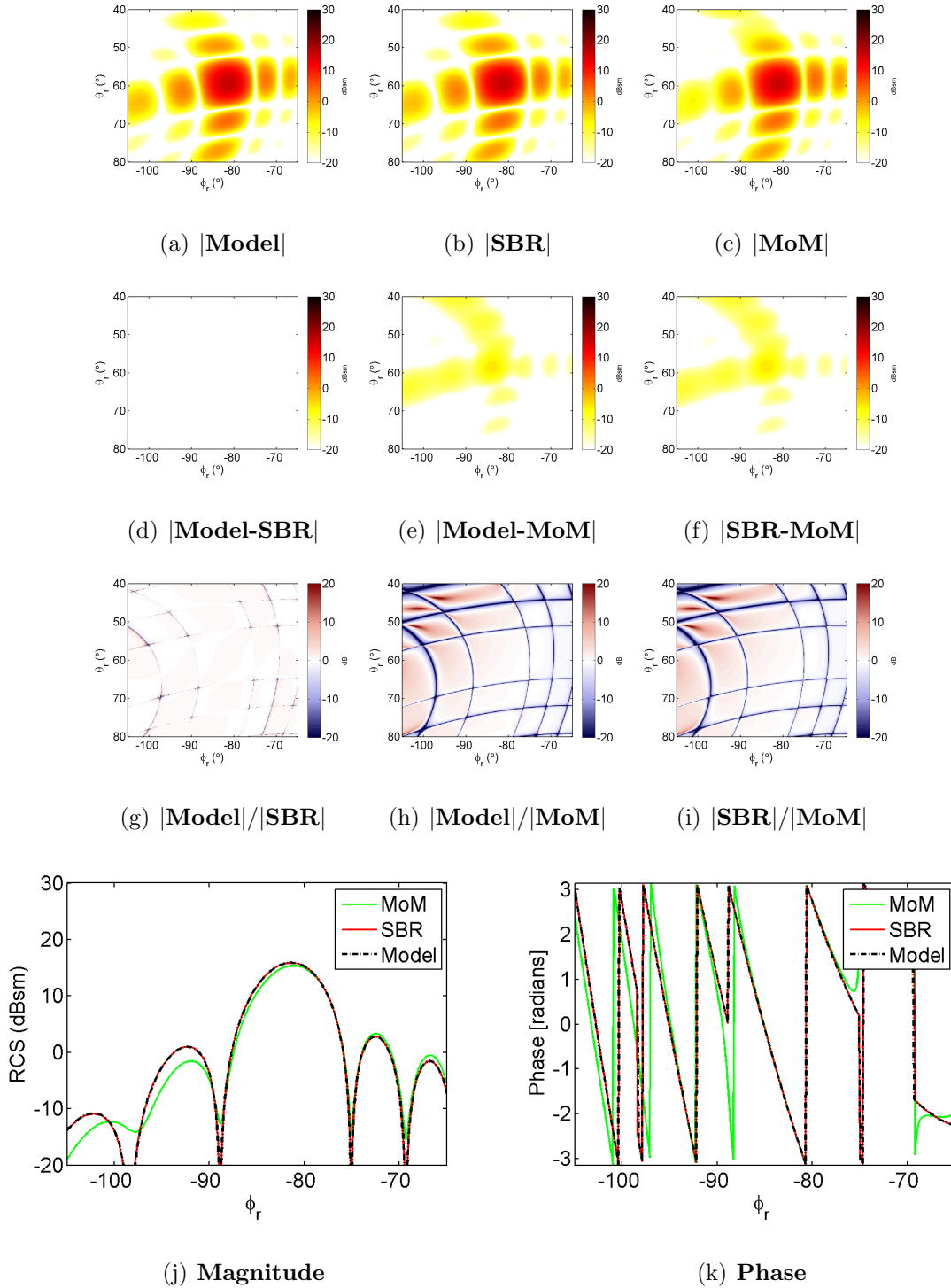


Figure A.7. Comparison of VV-pol scattering for the rotated and translated plate shown in Figure A.6 with incident aspect $(\theta_t, \phi_t) = (90^\circ, 30^\circ)$. Figures a-c show the magnitude response for the model developed in this thesis, SBR, and MoM data respectively. Figures d-f show the coherent difference, and g-i show the magnitude ratio between these waveforms. Figures j and k show magnitude and phase for an azimuth sweep for constant elevation through the peak response, in this case $\theta_r = 60^\circ$.

HV-polarization

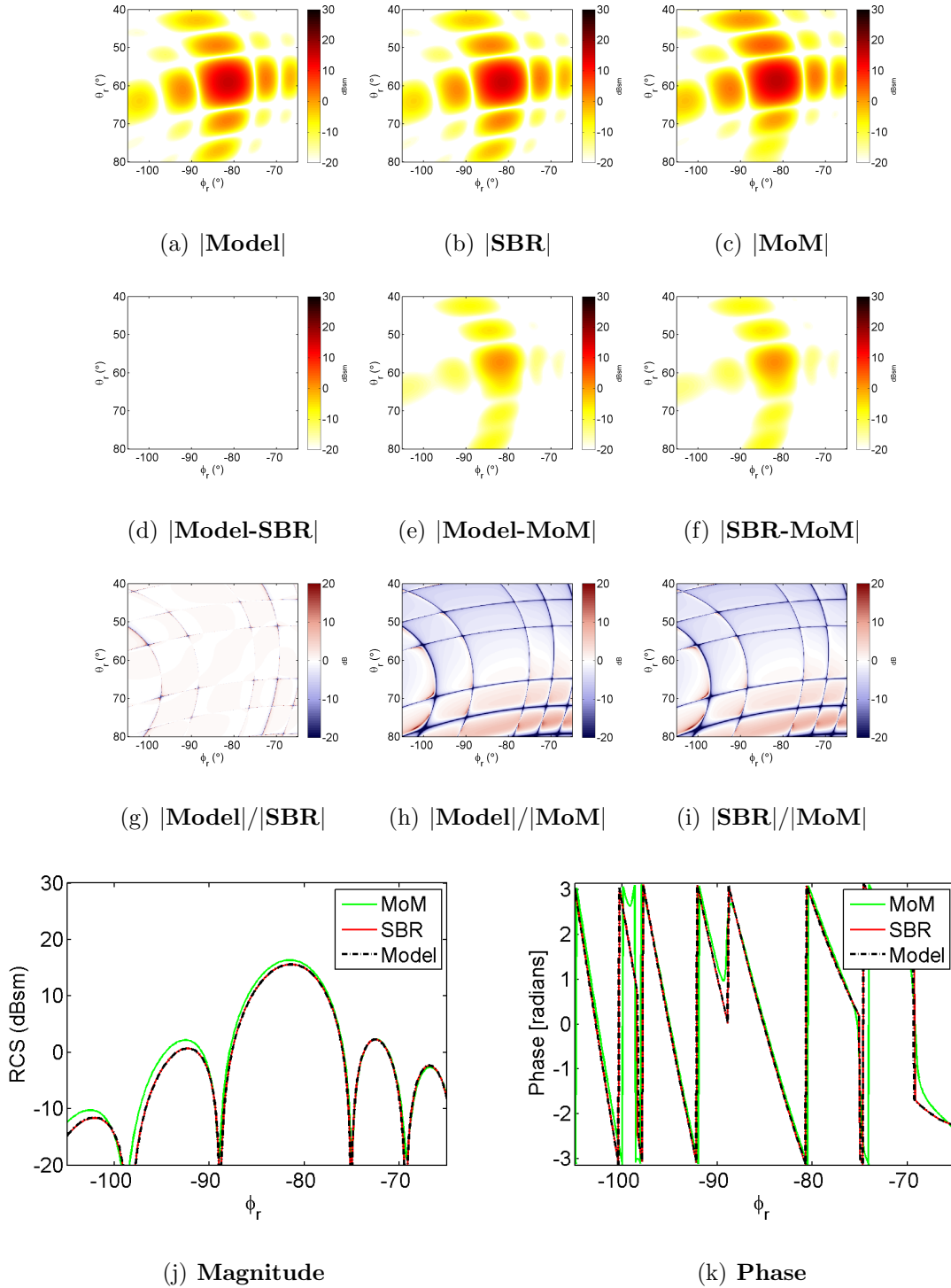


Figure A.8. Comparison of HV-pol scattering for the rotated and translated plate shown in Figure A.6 with incident aspect $(\theta_t, \phi_t) = (90^\circ, 30^\circ)$. Figures a-c show the magnitude response for the model developed in this thesis, SBR, and MoM data respectively. Figures d-f show the coherent difference, and g-i show the magnitude ratio between these waveforms. Figures j and k show magnitude and phase for an azimuth sweep for constant elevation through the peak response, in this case $\theta_r = 60^\circ$.

VH-polarization

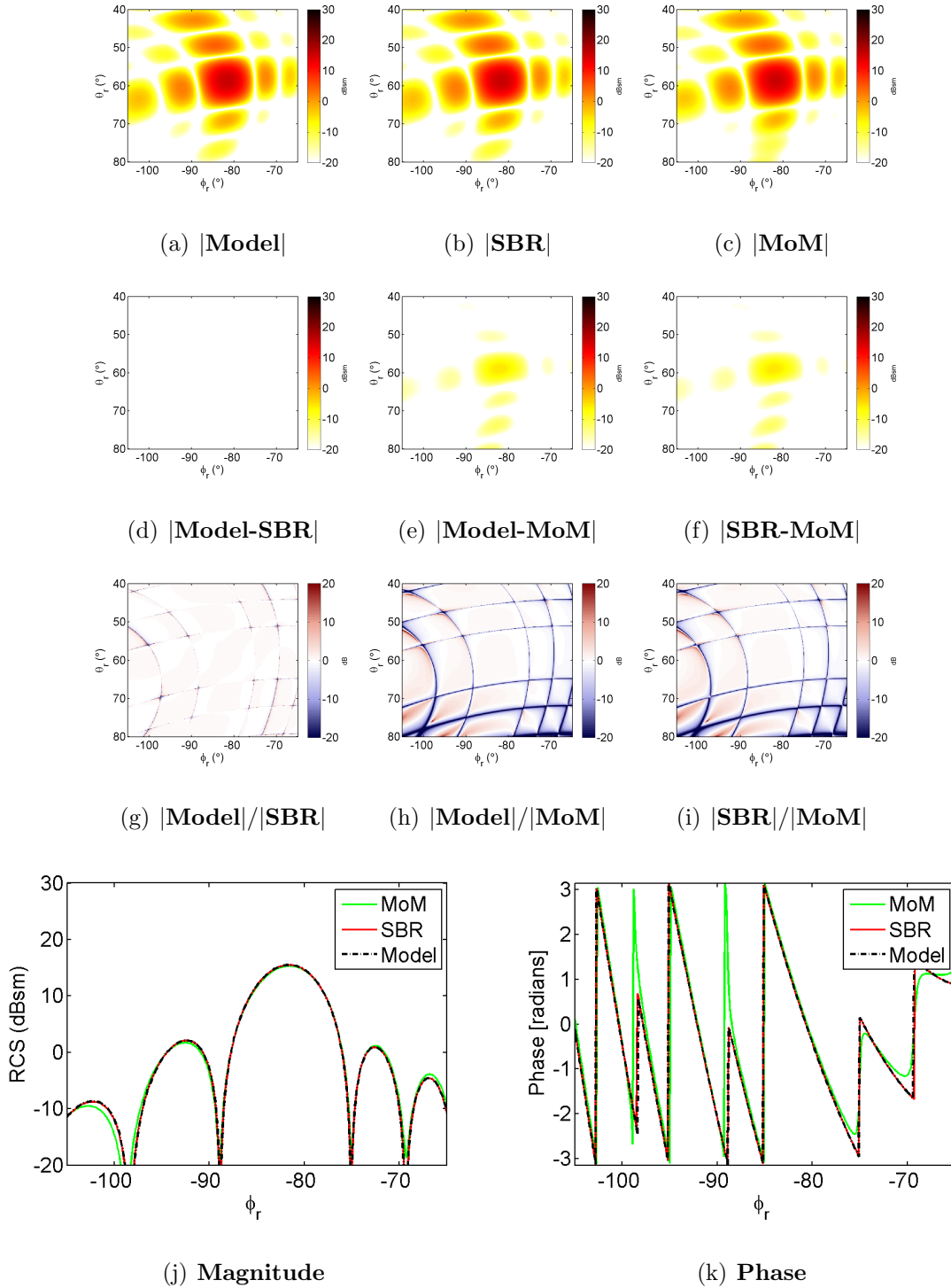


Figure A.9. Comparison of VH-pol scattering for the rotated and translated plate shown in Figure A.6 with incident aspect $(\theta_t, \phi_t) = (90^\circ, 30^\circ)$. Figures a-c show the magnitude response for the model developed in this thesis, SBR, and MoM data respectively. Figures d-f show the coherent difference, and g-i show the magnitude ratio between these waveforms. Figures j and k show magnitude and phase for an azimuth sweep for constant elevation through the peak response, in this case $\theta_r = 60^\circ$.

HH-polarization

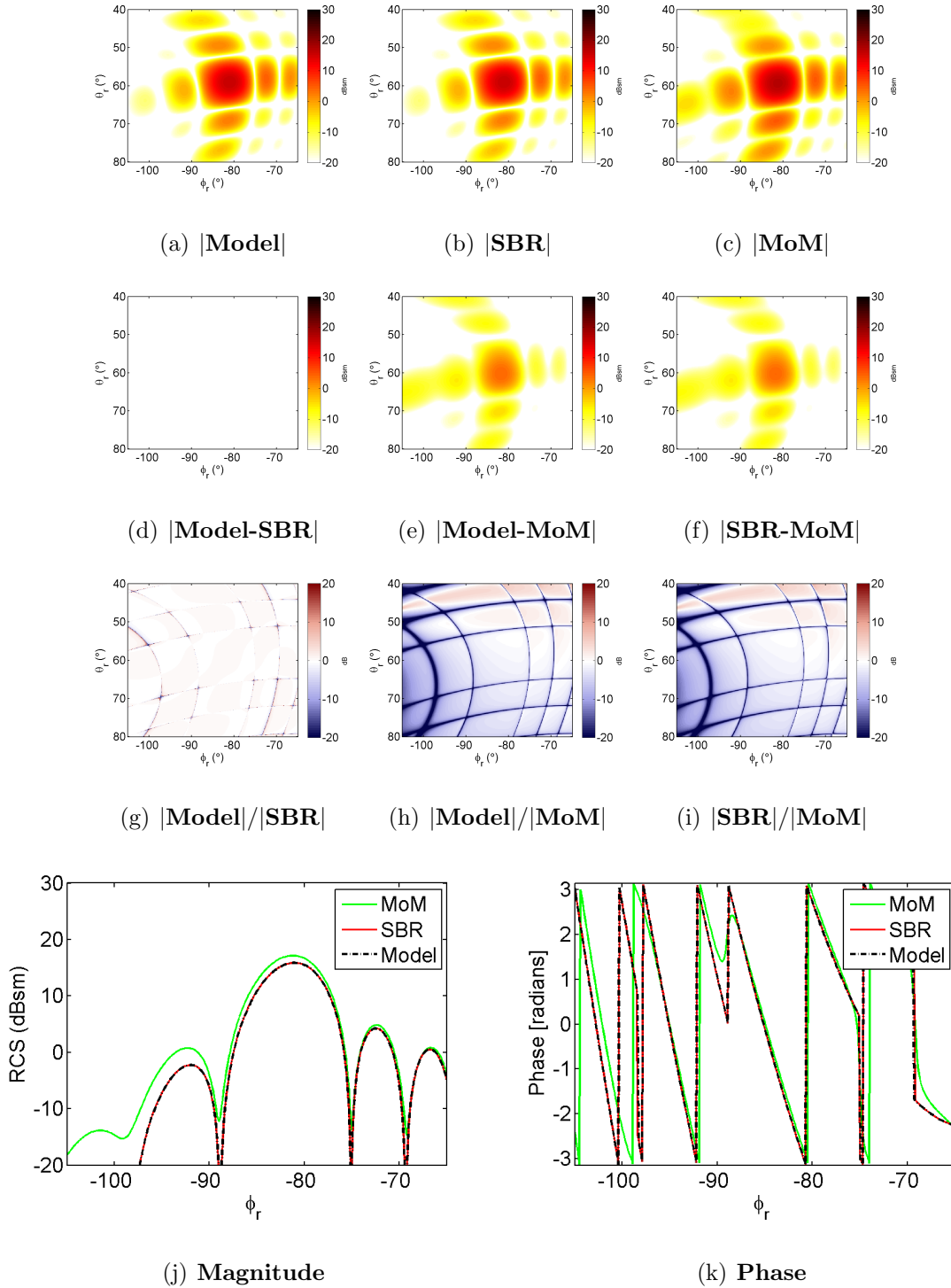


Figure A.10. Comparison of HH-pol scattering for the rotated and translated plate shown in Figure A.6 with incident aspect $(\theta_t, \phi_t) = (90^\circ, 30^\circ)$. Figures a-c show the magnitude response for the model developed in this thesis, SBR, and MoM data respectively. Figures d-f show the coherent difference, and g-i show the magnitude ratio between these waveforms. Figures j and k show magnitude and phase for an azimuth sweep for constant elevation through the peak response, in this case $\theta_r = 60^\circ$.

Appendix B. Co/Cross-pol Dihedral Scattering

This appendix contains the co/cross-polarization scattering equations for the bistatic 3D GO-PO dihedral scattering solution developed in [12] and summarized in Section 3.3.2. This information is presented in the appendix due to space constraints in Chapter III.

2.1 Co/Cross-pol Equations

Using Equation (3.26), the co/cross-pol PO solution for bistatic scattering from a dihedral at the orientation shown in Figure 3.3 is [12]:

$$\begin{aligned} \vec{E}'_{\text{VV,dih}} = & \frac{jkL}{2\pi} \text{sinc}\left(\frac{L}{2}\mathcal{Z}\right) \sin\theta'_r \left[a \text{sinc}\left(\frac{a}{2}\mathcal{X}\right) e^{\frac{ia}{2}\mathcal{X}} \sin\phi'_t \right. \\ & \left. - b \text{sinc}\left(\frac{b}{2}\mathcal{Y}\right) e^{\frac{ib}{2}\mathcal{Y}} \cos\phi'_t \right] - \frac{jk}{2\pi} \sin\theta'_r (\mathcal{I}_{xz} \sin\phi'_t + \mathcal{I}_{yz} \cos\phi'_t) \end{aligned} \quad (\text{B.1a})$$

$$\vec{E}'_{\text{HV,dih}} = 0 \quad (\text{B.1b})$$

$$\begin{aligned} \vec{E}'_{\text{VH,dih}} = & \frac{-jkL}{2\pi} \text{sinc}\left(\frac{L}{2}\mathcal{Z}\right) \left[a \text{sinc}\left(\frac{a}{2}\mathcal{X}\right) e^{\frac{ia}{2}\mathcal{X}} (\cos\theta'_r \cos\phi'_r \sin\theta'_t - \cos\theta'_t \cos\phi'_t \sin\theta'_r) \right. \\ & \left. - b \text{sinc}\left(\frac{b}{2}\mathcal{Y}\right) e^{\frac{ib}{2}\mathcal{Y}} (\cos\theta'_t \sin\phi'_t \sin\theta'_r - \cos\theta'_r \sin\phi'_r \sin\theta'_t) \right] \\ & - \frac{jk}{2\pi} (\sin\theta'_t \cos\theta'_r (\mathcal{I}_{xz} \cos\phi'_r - \mathcal{I}_{yz} \sin\phi'_r) \\ & + \cos\theta'_t \sin\theta'_r (\mathcal{I}_{xz} \cos\phi'_t - \mathcal{I}_{yz} \sin\phi'_t)) \end{aligned} \quad (\text{B.1c})$$

$$\begin{aligned} \vec{E}'_{\text{HH,dih}} = & \frac{jkL}{2\pi} \text{sinc}\left(\frac{L}{2}\mathcal{Z}\right) \sin\theta'_t \left[a \text{sinc}\left(\frac{a}{2}\mathcal{X}\right) e^{\frac{ia}{2}\mathcal{X}} \sin\phi'_r \right. \\ & \left. - b \text{sinc}\left(\frac{b}{2}\mathcal{Y}\right) e^{\frac{ib}{2}\mathcal{Y}} \cos\phi'_r \right] + \frac{jk}{2\pi} \sin\theta'_t (\mathcal{I}_{xz} \sin\phi'_r + \mathcal{I}_{yz} \cos\phi'_r) \end{aligned} \quad (\text{B.1d})$$

where $\mathcal{X} = k(\sin\theta'_r \cos\phi'_r + \sin\theta'_t \cos\phi'_t)$, $\mathcal{Y} = k(\sin\theta'_r \sin\phi'_r + \sin\theta'_t \sin\phi'_t)$, $\mathcal{Z} = k(\cos\theta'_r + \cos\theta'_t)$, and the integral terms \mathcal{I}_{xz} , \mathcal{I}_{yz} are defined in Equations (3.18)-(3.21).

Bibliography

- [1] Balanis, Constantine A. *Advanced Engineering Electromagnetics*. John Wiley & Sons, New York, 1989.
- [2] Baldauf, J., S.-W. Lee, L. Lin, S.-K. Jeng, S.M. Scarborough, and C.L. Yu. “High Frequency Scattering from Trihedral Corner Reflectors and other Benchmark Targets: SBR versus Experiment”. *Antennas and Propagation, IEEE Transactions on*, 39(9):1345–1351, Sep. 1991.
- [3] Bhattacharyya, Asoke K. and D. L. Sengupta. *Radar Cross Section Analysis and Control*. Artech House, Norwood, MA, 1991.
- [4] Blejer, D. J. *X- and Ku-band calibration reflectors for the MIT LL synthetic aperture radar*. Technical report, MIT Lincoln Lab Project Report ECCM-1, March 2 1998.
- [5] Coifman, R., V. Rokhlin, and S. Wandzura. “The fast multipole method for the wave equation: a pedestrian prescription”. *Antennas and Propagation Magazine, IEEE*, 35(3):7–12, June 1993.
- [6] Collins, P. “EENG630 lecture notes”. AFIT EENG630 - Asymptotic Techniques of Electromagnetic Theory.
- [7] Cripin Jr., J. W. and K. M. Siegel. *Methods of Radar Cross-Section Analysis*. Academic Press, New York, 1968.
- [8] Griesser, Timothy and Constantine A. Balanis. “Backscatter Analysis of Dihedral Corner Reflectors Using Physical Optics and Physical Theory of Diffraction”. *IEEE Trans. on Antennas and Propagation*, 35(10):1137–1147, Oct. 1987.
- [9] Griesser, Timothy and Constantine A. Balanis. “Dihedral Corner Reflector Backscatter Using Higher Order Reflections and Diffractions”. *IEEE Trans. on Antennas and Propagation*, 35(11):1235–1247, Nov. 1987.
- [10] Havrilla, M. “EENG622 lecture notes”. AFIT EENG622 - Advanced Electromagnetics.
- [11] Jackson, Julie Ann. *Three-Dimensional Feature Models for Synthetic Aperture Radar and Experiments in Feature Extraction*. Ph.D. thesis, The Ohio State University, 2009.
- [12] Jackson, Julie Ann. “Closed-form, Bistatic 3D Scattering Solution for a Dihedral Corner Reflector”. *Progress in Electromagnetics Research Symposium (PIERS), PIERS Online*, volume 6, 495–499. 2010.

- [13] Jackson, Julie Ann, Brian D. Rigling, and Randolph L. Moses. “Canonical Scattering Feature Models for 3D and Bistatic SAR”. *IEEE Trans. on Aerospace and Electronic Systems*, 46(2):525–541, Apr. 2010.
- [14] Knott, E. F. “RCS reduction of dihedral corners”. *IEEE Trans. on Antennas and Propagation*, AP-25(3):406–409, May 1977.
- [15] Knott, Eugene F. *Radar Cross Section Measurements*. Van Nostrand Reinhold, New York, 1993.
- [16] Knott, Eugene F., John F. Shaeffer, and Michael T. Tuley. *Radar Cross Section, Second Edition*. Artech House, Boston, 1993.
- [17] Maloney, Jim. “Introduction to Electromagnetic Fundamentals”. Course Notes, Radar Cross Section Reduction Short Course, Georgia Tech Research Institute.
- [18] Michaeli, A. “A closed form physical theory of diffraction solution for electromagnetic scattering by strips and 90 deg dihedrals”. *Radio Science*, 19(2):609–616, Apr. 1984.
- [19] Peebles, Peyton Z. *Radar Principles*. John Wiley & Sons, New York, 1998.
- [20] Ruck, George T., Donald E. Barrick, William D. Stuart, and Clarence K. Krichbaum. *Radar Cross Section Handbook*. Plenum Press, New York, 1970.
- [21] Song, J.M. and W.C. Chew. “Fast multipole method solution of three dimensional integral equation”. *Antennas and Propagation Society International Symposium, 1995. AP-S. Digest*, volume 3, 1528 –1531 vol.3. June 1995.
- [22] Song, J.M., C.C. Lu, W.C. Chew, and S.W. Lee. “Introduction to fast Illinois solver code (FISC)”. *Antennas and Propagation Society International Symposium, 1997. IEEE., 1997 Digest*, volume 1, 48 –51 vol.1. July 1997.
- [23] Tempelis, A., M. Jussaume, and J. A. Jackson. “Comparison of Measured and Predicted Bistatic Scattering from a Right-Angle Dihedral”. *IEEE Radar Conference*. To be presented May 2011.
- [24] Wang, S.-Y. and S.-K. Jeng. “A compact RCS formula for a dihedral corner reflector at arbitrary aspect angles”. *IEEE Trans. on Antennas and Propagation*, 46(7):1112–1113, July 1998.

Vita

Capt Andreas Tempelis was born in Duluth, MN. After graduating from Superior Senior High School in Superior, WI, he enrolled at the University of Minnesota, Twin Cities. There he majored in Electrical Engineering and minored in Business Management. After graduating in Dec 2005, he attended Officer Training School (OTS) at Maxwell AFB, Montgomery, Alabama and was commissioned into the United States Air Force in April 2006. Following OTS, he was assigned to Peterson AFB, Colorado. There he worked in the 850th Electronic Systems Group Space Sustainment Division (850th ELSG/NS) as a project manager for ground-based space tracking systems. Following his assignment at Peterson AFB, he entered graduate school at the Air Force Institute of Technology (AFIT) in August 2009 and is currently completing his Master's Degree. His anticipated follow-on assignment is to the Sensors Directorate of the Air Force Research Labs (AFRL/RV) at Wright-Patterson AFB, Ohio.

REPORT DOCUMENTATION PAGE

Form Approved
OMB No. 0704-0188

The public reporting burden for this collection of information is estimated to average 1 hour per response, including the time for reviewing instructions, searching existing data sources, gathering and maintaining the data needed, and completing and reviewing the collection of information. Send comments regarding this burden estimate or any other aspect of this collection of information, including suggestions for reducing this burden to Department of Defense, Washington Headquarters Services, Directorate for Information Operations and Reports (0704-0188), 1215 Jefferson Davis Highway, Suite 1204, Arlington, VA 22202-4302. Respondents should be aware that notwithstanding any other provision of law, no person shall be subject to any penalty for failing to comply with a collection of information if it does not display a currently valid OMB control number. **PLEASE DO NOT RETURN YOUR FORM TO THE ABOVE ADDRESS.**

1. REPORT DATE (DD-MM-YYYY) 24-03-2011		2. REPORT TYPE Master's Thesis		3. DATES COVERED (From — To) Aug 2009 — Mar 2011	
4. TITLE AND SUBTITLE BISTATIC 3D ELECTROMAGNETIC SCATTERING FROM A RIGHT-ANGLE DIHEDRAL AT ARBITRARY ORIENTATION AND POSITION				5a. CONTRACT NUMBER	
				5b. GRANT NUMBER	
				5c. PROGRAM ELEMENT NUMBER	
6. AUTHOR(S) Andreas Z. Tempelis, Capt, USAF				5d. PROJECT NUMBER	
				5e. TASK NUMBER	
				5f. WORK UNIT NUMBER	
7. PERFORMING ORGANIZATION NAME(S) AND ADDRESS(ES) Air Force Institute of Technology Graduate School of Engineering and Management (AFIT/EN) 2950 Hobson Way WPAFB OH 45433-7765				8. PERFORMING ORGANIZATION REPORT NUMBER AFIT/GE/ENG/11-39	
INTENTIONALLY LEFT BLANK				10. SPONSOR/MONITOR'S ACRONYM(S)	
				11. SPONSOR/MONITOR'S REPORT NUMBER(S)	
12. DISTRIBUTION / AVAILABILITY STATEMENT APPROVED FOR PUBLIC RELEASE; DISTRIBUTION UNLIMITED. This material is declared a work of the U.S. Government and is not subject to copyright protection in the United States.					
13. SUPPLEMENTARY NOTES					
14. ABSTRACT A method is created to extend a bistatic 3D electromagnetic scattering solution for a dihedral at a given orientation and position to the case of arbitrary orientation and position. Results produced using this method are compared to shooting and bouncing rays (SBR) and method of moments (MoM) predictions, as well as measured data for applicable cases. The model in this thesis shows excellent agreement in magnitude and phase with SBR predictions. It also shows good agreement in magnitude with MoM predictions. Small phase differences between model and MoM data occur due to differences in the underlying scattering solution and the more exact MoM prediction. The model accurately predicts bistatic scattering from a dihedral at arbitrary orientation and position and is computationally more efficient than SBR and MoM methods.					
15. SUBJECT TERMS Bistatic, Electromagnetic Scattering, Dihedral, RCS, Feature Identification, Synthetic Aperture Radar Calibration					
16. SECURITY CLASSIFICATION OF:			17. LIMITATION OF ABSTRACT	18. NUMBER OF PAGES	19a. NAME OF RESPONSIBLE PERSON
a. REPORT	b. ABSTRACT	c. THIS PAGE			Dr. Julie A. Jackson (ENG)
U	U	U	UU	120	19b. TELEPHONE NUMBER (include area code) (937) 255-3636, x4678; julie.jackson@afit.edu